ABSTRACT

FEASIBILITY OF SUPERCONDUCTIVITY IN SEMICONDUCTOR SUPERLATTICES

by

Kenneth P. Walsh

The objective of this thesis is to explore superconductivity in semiconductor superlattices of alternating hole and electron layers. The feasibility of superconductivity in semiconductor superlattices is based on a model formulated by Harshman and Mills. In this model, a semiconductor superlattice forms the layered electron and hole reservoirs of high transition temperature (high-T_C) superconductors.

A $GaAs-Al_XGa_{1-X}As$ semiconductor structure is proposed which is predicted to superconduct at $T_C = 2.0$ K and may be analogous to the layered electronic structure of high-T_C superconductors. Formation of an alternating sequence of electron- and hole-populated quantum wells (an electron-hole superlattice) in a modulation-doped $GaAs-Al_XGa_{1-X}As$ superlattice is considered. In this superlattice, the distribution of carriers forms a three-dimensional Wigner lattice where the mean spacing between carriers in the x-y plane is the same as the periodic distance between wells in the superlattice. This geometrical relationship mimics a prominent property of optimally doped high $-T_C$ superconductors.

A Schrödinger-Poisson solver, developed by Snider, is applied to the problem of determining the appropriate semiconductor layers for creating equilibrium electron-hole superlattices in the $GaAs-Al_XGa_{1-X}As$ system. Formation of

equilibrium electron-hole superlattices in modulation-doped $GaAs-Al_XGa_{1-X}As$ is studied by numerical simulations. Electron and heavy-hole states are induced by built-in electric fields in the absence of optical pumping, gate electrodes, or electrical contacts. The $GaAs-Al_XGa_{1-X}As$ structure and the feasibility of meeting all the criteria of the Harshman model for superconductivity is studied by self-consistent numerical simulation.

In order to test the existence of superconductivity, the physics of sensor arrays and their ability to create synthetic images of semiconductor structures, is explored. Approximations are considered and practical applications in detecting superconductivity in superlattices are evaluated.

FEASIBILITY OF SUPERCONDUCTIVITY IN SEMICONDUCTOR SUPERLATTICES

by

Kenneth P. Walsh

A Dissertation
Submitted to the Faculty of the
New Jersey Institute of Technology and
Rutgers, the State University of New Jersey-Newark
in Partial Fulfillment of the Requirements for the Degree of
Doctor of Philosophy in Applied Physics

Federated Physics Department

August 2006

APPROVAL PAGE

FEASIBILITY OF SUPERCONDUCTIVITY IN SEMICONDUCTOR SUPERLATTICES

Kenneth P. Walsh

Dr. Anthony Fiory, Dissertation Advisor — Date
Research Professor of Physics, NJIT

Dr. Nuggehalli M. Ravindra, Dissertation Advisor — Date
Professor of Physics, NJIT

Dr. John C. Hensel, Thesis Committee — Date
Distinguished Research Professor of Physics, NJIT

Dr. Tao Zhou, Thesis Committee — Date
Assistant Professor of Physics, NJIT

Dr. Zhen Wu, Thesis Committee — Date
Associate Professor of Physics, Rutgers University

Mr. Martin Lepselter, Thesis Committee — Date
President, BTL Fellows, Inc.

BIOGRAPHICAL SKETCH

Author: Kenneth P. Walsh

Degree: Doctor of Philosophy

Date: August, 2006

Undergraduate and Graduate Education:

- Master of Arts in Physics,
  Queens College, Flushing, NY 1985

- Bachelor of Arts in Mathematics,
  Queens College, Flushing, NY 1972

Major: Physics

Presentations and Publications:

Walsh, K.P & Rajendran, A.M. (1997). Modeling of in-situ ballistic measurements using the Rajendran-Grove and Johnson-Holmquist ceramic models. Proceedings of the Shock Compression and Condensed Matter, AIP Press, 913-916.

Walsh, K.P. (2000). Modeling the physical response of ceramics using a shock physics based code. Physics MS Thesis (unpublished), University of Maryland, Baltimore, MD.

Walsh, K.P., Schulkin, B., Gary, D., Federici, J. F., Barat, R. & Zimdars, D. (2004). Terahertz near field interferometric and synthetic aperture imaging. Proceedings SPIE, Volume 5411, 1-9.

Walsh, K.P., Fiory, A. T., Ravindra, N. M., Harshman, D. R. & Dow, J. D. (2006). Feasibility of superconductivity in semiconductor superlattices. March APS Meeting Abstract/Presentation, Baltimore, MD.

Walsh, K.P., Fiory, A. T., Ravindra, N. M., Harshman, D. R. & Dow, J. D. (2006). Electron-Hole superlattices in GaAs/$Al_xGa_{1-x}As$ multiple quantum wells. Philosophical Magazine, Volume 86, Number 23, 3581 - 3593.

To the memory of my beloved cairn terrier

Toto

1985-2001

"He gave so much and asked so little"

ACKNOWLEDGEMENTS

I would like to express my deepest appreciation to Dr. Anthony Fiory and Dr. Nuggehalli Ravindra, who not only served as my research supervisors, providing valuable and countless resources, insight, and intuition but also constantly gave me support, encouragement, and reassurance. Special thanks are given to Professors John Hensel, Tao Zhou, Zhen Wu, and Martin Lepselter for actively participating in my committee.

Appreciation is extended to Dr. D. R Harshman of Physikon Research, Arizona State University, and the University of Notre Dame and Dr. J. D. Dow of the Arizona State University for their valuable support and collaboration. I appreciate the support of Dr. Rao Surapeneni, Mr. Steven Nicolich and Mr. James Wejsa of the US Army at Picatinny, NJ, who provided funding for my research efforts.

I am highly fortunate to have obtained an open source software program written by Dr. Greg Snider of Notre Dame University. Without this program, my thesis research would have been difficult or even impossible to accomplish.

Last, but not least, I am grateful to the helpful assistance of Catherine Allen, US Army Librarian at Picatinny, NJ, who helped me obtain much of the background literature used in this study.

TABLE OF CONTENTS

Chapter	Page
1 INTRODUCTION	1
1.1 Objective	1
1.2 High Temperature Superconductivity	3
1.3 Computer Modeling of Superlattice Nanostructures	8
2 THEORY	12
2.1 BCS Theory of Superconductivity	12
2.2 The Harshman Formulation and Conditions for Superconductivity	12
2.3 Electron-Hole Formation in Superlattice GaAs-AlGaAs Wells	27
3 RESULTS OF COMPUTER SIMULATIONS OF SUPERLATTICES	31
3.1 Sensitivity of the Electron-Hole Superlattice to Parametric Changes at Low Temperatures	31
3.2 The Effect of Donor Concentrations and Layer Thickness on the Beta vs. T Plot	47
3.3 Superlattices with Uniform Spacing	53
3.4 Superlattices with Non-Uniform Spacing and Delta Doping	59
4 RECENT DEVELOPMENTS IN HIGH TEMPERATURE SUPERCONDUCTIVITY	60
4.1 Experimental and Theoretical Developments	60
5 THE DETECTION OF SUPERCONDUCTIVITY USING SYNTHETIC IMAGING	65
5.1 Synthetic Imaging	65
5.1.1 General Principles	65
5.1.2 Coherence Function for Sensor Pairs on a Parabolic Array	72

TABLE OF CONTENTS
(Continued)

Chapter **Page**

5.1.3 Coherence Function for Sensor Pairs on a Spherical Array..... 74

5.1.4 Coherence Function for Sensor Pairs on a Planar Array..... 76

5.2 Far Field Form of Phase Difference between Two Sensor Points in a Planar Array..... 77

5.3 Physical Structure of Near Fields Incident upon a Spherical Array..... 81

5.4 Synthetic Imaging Using an IFT of a U-V File..... 84

5.5 Synthetic Imaging and the Detection of Superconductivity..... 90

6 CONCLUSIONS..... 97

APPENDIX A DERIVATION OF LOGARITHMIC DERIVATIVE OF THE CRITICAL TEMPERATURE..... 98

APPENDIX B VALIDITY OF THE 3D HOLE/ELECTRON DENSITY FUNCTIONS AT THE T=0 K LIMIT..... 99

APPENDIX C THE 2-D INVERSE FOURIER TRANSFORM (IFT) OF THE PRODUCT OF TWO DISPLACEMENT VECTORS AND THE CORRELATION FUNCTION..... 100

APPENDIX D DERIVATION OF THE CONDITION FOR NON-DISSIPATION OF AN EM WAVE THROUGH A CONDUCTIVE MEDIUM..... 103

LIST OF FIGURES

Figure		Page
1.1	An example of a semiconductor superlattice	2
1.2	The 2-D surface density vs. inverse square separation	6
1.3	Effect of magnetic field on resistance of a GaAs electron superlattice	7
1.4	Flowchart of the Snider computer program	9
1.5	Hartree and Thomas-Fermi plots of electron energy and density of carrier states.	11
2.1	Critical temperature vs. sheet carrier density	15
2.2	3D plot of argument of coulomb correlation vs. surface carrier density and the Debye frequency	18
2.3	The energies for computer simulated noncrystalline structure (solid triangles) and regular superlattice structures (open squares)	26
2.4	(a) The lowest energy structure has alternating infinite straight chains of ions at x = 0.4, (b) A zigzag structure at x = 0.4	26
3.1	Semiconductor superlattice and carrier formation	33
3.2	Temperature dependence of sheet electron and hole densities calculated for the modulation doped superlattice for alloy concentration of x = 0.4	34
3.3	Variation of well sheet electron and hole densities with concentration of dopants in modulation doped layers of a superlattice for alloy concentration of x = 0.4	35
3.4	(a) Edges of conduction band, (b) Edges of valence band. For modulation doped n-p-n superlattice of alloy composition x = 0.4 as functions of depth y (Case 3)	40
3.5	Variation with depth y of the built-in electric field of a modulation doped n-p-n superlattice of alloy composition x = 0.4 (Case 3)	41
3.6	(a) Edges of conduction band, (b) Edges of valence band. For modulation doped n-p-n superlattice of alloy composition x = 0.4 as functions of depth y (Case 4)	42

LIST OF FIGURES
(Continued)

Figure **Page**

3.7 Variation with depth y of the built-in electric field of a modulation doped n-p-n superlattice of alloy concentration x = 0.4 (Case 4) 43

3.8 Plots of acceptor areal density vs. d-delta..... 45

3.9 Plots of charge transfer efficiency vs. d-delta..... 46

3.10 Quantum confinement in GaAs wells..... 47

3.11 Effect of layer thickness on beta..... 50

3.12 Effect of donor concentration on beta, L = 50 Angstroms..... 51

3.13 Beta vs. T (Case 1)..... 54

3.14 Beta vs. T (Case 2)..... 55

3.15 Beta vs. T (Case 4)..... 57

3.16 Beta vs. T (Case 5)..... 59

5.1 (a) Near field wave fronts, (b) Far field wave fronts, (c) Geometry of array and source..... 67

5.2 (a) Far field wave fronts parallel to sensor plane, (b) Far field wave fronts at an angle to sensor plane..... 68

5.3 (a) planar array, (b) curved array..... 71

5.4 Geometry of sensor nodes and near field source..... 71

5.5 Point source at d producing wave fronts at points 1,2 on the surface of a parabolic array..... 73

5.6 Point source at d producing wave fronts at points 1,2 on the surface of a spherical array..... 75

5.7 Point source at d producing wave fronts at points 1,2 on the surface of a planar array..... 76

LIST OF FIGURES
(Continued)

Figure **Page**

5.8 Source dS' irradiating a pair of sensors..... 78

5.9 Error delta from imaging 1.0, 2.0, 3.0 cm objects, frequency of radiation = 1.0 terahertz..... 80

5.10 (a) Spherical sensor array and imaged object, (b) Spherical coordinate system..... 83

5.11 Sensor nodes 1, 2 receiving radiation from a source point..... 85

5.12 (a) Geometric arrangement of u-v 25 sensor nodes, (b) Nodes generated in space by 25 sensors..... 86

5.13 (a) Circular geometric arrangement of 25 sensor nodes, (b) Nodes generated in space by 25 circular sensors..... 87

5.14 (a) Synthetic imaging of a source point with a spherical array, (b) Synthetic imaging of a source point with a circular array..... 88

5.15 (a) Synthetic imaging of a source point with a spherical array, (b) Synthetic imaging of a source point with a circular array..... 89

5.16 Circular array imaging sample in a cryostat..... 92

5.17 Scheme for determining superconductivity in a superlattice using a circular array..... 93

5.18 EM wave entering a semiconductor in superconducting state..... 95

5.19 Reflectivity of LSCO as a function of the frequency for fixed impurity scattering rate with different temperatures..... 96

C.1 Geometry of source point and sensor nodes..... 101

LIST OF TABLES

Table		Page
3.1	Vary T (Case 1).....	32
3.2	Vary Doping Concentrations, Beta (Case 2).....	37
3.3	Effect of D-Delta on Sheet Resistance, Maximum Electric Field and Charge Transfer Efficiency	38
3.4	Effect of D-Delta on Energy Band Offsets...	38
3.5	Vary D-Delta, D-Spacer (Case 3)...	39
3.6	Vary D-Delta, D-Well (Case 4)...	44
3.7	Effect of Donor/Acceptor Concentration N and Layer Thickness L on Beta.....	48
3.8	Relationships between the Electric Field and the Sheet Resistance as the Layer Thickness and Doping Concentrations are Varied...	51
3.9	Effect of Donor and Acceptor Concentration N and Layer Width on Beta (Case 3).....	56
5.1	Wavelength, Frequency and SR.....	91

LIST OF SYMBOLS AND ACRONYMS

T, T_β	temperature, temperature when $\beta=1$
m_H^*, m_E^*	hole effective mass, electron effective mass
n, p	electrons, holes density (atoms/cubic centimeter)
Tf-n, Tf-p	Fermi temperature calculated from N_S, P_S
J	electron current density
d	periodic distance between 2 hole or electron wells
β	beta, $N_S d^2$, $P_S d^2$
SR	spatial resolution
R_S	sheet resistance
N	donor/acceptor concentration (atoms/cubic centimeter)
E_G	energy level difference between two adjacent wells
E_C	conduction band energy
E_V	valence band energy
E_C^B	conduction band energy in AlGaAs well
E_C^W	conduction band energy in GaAs well
nano object	object whose dimensions are measured in Angstroms
macro object	object whose dimensions are measured in millimeters or centimeters
N_S	surface electron density
P_S	surface hole density
$D(E_i)$	density of states for energy E_i
$\mathring{A}$	Angstrom
SC	superconducting
λ_E	electron-phonon coupling coefficient
λ_{HE}	hole-exciton coupling coefficient
μ	Coulombic correlation coefficient
ΔL	lateral resolution
x	alloy concentration in $Al_xGa_{1-x}As$
ε_x	dielectric constant of $Al_xGa_{1-x}As$
L	layer thickness in Angstroms
d_X, d-spacer	spacing between N_D^+ and N_A^- layers in $Al_xGa_{1-x}As$
d_W, d-well	width of the undoped GaAs wells
d_δ, d-delta	width of the doped $Al_xGa_{1-x}As$ layers.
d_S	width of the substrate
d_C	width of the cap

N_{Ai}	acceptor concentration for layer I (atoms/cubic centimeter)
N_{Di}	donor concentration for layer I (atoms/cubic centimeter)
N_D^+, N_A^-	ionized donor, acceptor densities (atoms/cubic centimeter)
dy	mesh size
SE	Schrödinger Equation
Ψ	wavefunction
ρ	charge density (per cubic centimeter)
En	total energy of a particle
E_{GS}	GaAs energy band gap in the superlattice
E_{TOL}	maximum induced electric field a superlattice can tolerate
E_{MAX}	maximum induced electric filed within a superlattice
nm	nanometer
$\Delta E_{C\_OFF}/\Delta d_\delta$	change of conduction band offset with respect to d_δ
$\Delta E_{V\_OFF}/\Delta d_\delta$	change of valence band offset with respect to d_δ
HTS	high temperature superconductivity
1-D	one dimension
2-D	two dimensions
3-D	three dimensions
V(k)	potential difference between adjacent wells as a function of wavenumber k
beta-n	beta associated with an electron distribution
beta-p	beta associated with an hole distribution
e-eigen	electron eigenvalue
h-eigen	hole eigenvalue
N_C	prefactor in the electron density of states relation $(2(2\pi m_E^* k_B T/h^2)^{2/3})$
N_D	prefactor in the hole density of states relation $(2(2\pi m_H^* k_B T/h^2)^{2/3})$
k_B	Boltzmann's constant
E_A	acceptor atom ionization energy
E_D	donor atom ionization energy
EM	electromagnetic
E	electric field
B	magnetic field
Ex	same as 10^X
σ_E	surface electric field density
m	meter
cm	centimeter
mm	milimeter
SC	superconductivity
IFT	Inverse Fourier Transform

CHAPTER 1

INTRODUCTION

1.1 Objective

The purpose of this study is to determine the structure and physical properties of semiconductor superlattices that exhibit superconductivity at high temperatures. In order to investigate this, GaAs-$Al_xGa_{1-x}As$ superlattice structures are utilized. A two-dimensional layered geometry of high critical temperature (high-T_C) superconducting materials is optimized both for T_C and the bulk Meissner fraction [1]. The proposed superlattice structure comprises multiple repeating undoped GaAs and doped or undoped $Al_xGa_{1-x}As$ layers which are analogous to the layered electronic structure of high-T_C superconductors. In the structures of interest, when the system is in a state of electrostatic equilibrium, the mean spacing between nearest electron or hole wells is the same as the mean distance between the electrons or holes in any given well. A computer program is applied to the problem of determining the appropriate semiconductor layers for creating equilibrium electron-hole GaAs-$Al_xGa_{1-x}As$ superlattices.

Computer simulations are based on a superlattice structure as seen in Figure 1.1. The superlattice is composed of layers of undoped GaAs layers, doped and undoped AlGaAs layers. The periodic distance d is the distance between GaAs wells surrounded by like doped AlGaAs. Numerically, one can express the periodic distance as $d = 2(2d_\delta + d_W + d_X)$, where d_δ, d_W, and d_X are the widths of the doped, well, and spacer layers, respectively. The program uses the method of finite differences to find the

one-dimensional band diagram of a semiconductor structure. It can automatically calculate the band diagrams for multiple bias voltages, sheet resistance, and surface carrier densities. A self-consistent 1D solution of the Schrödinger and Poisson Equations is obtained using the finite-difference method (FDM) [2]. FDM divides real space into meshes and mesh points. The vector solution of Schrödinger Equation is solved for each mesh. The result is a matrix formulation of the solution of the Schrödinger Equation. The method is very effective in determining eigenstates over a relatively large spatial dimension without loss of accuracy. The program is menu driven through a pseudo-Mac interface but the user must provide separate text editing and plotting programs. The program calculates the conduction and valence band distributions, density of states and the hole and electron concentrations. Dopant ionization is included for both shallow and deep level dopants. This allows materials such as semi-insulating GaAs to be treated. Current flow is not calculated; therefore, the structure can be simulated only in thermodynamic equilibrium.

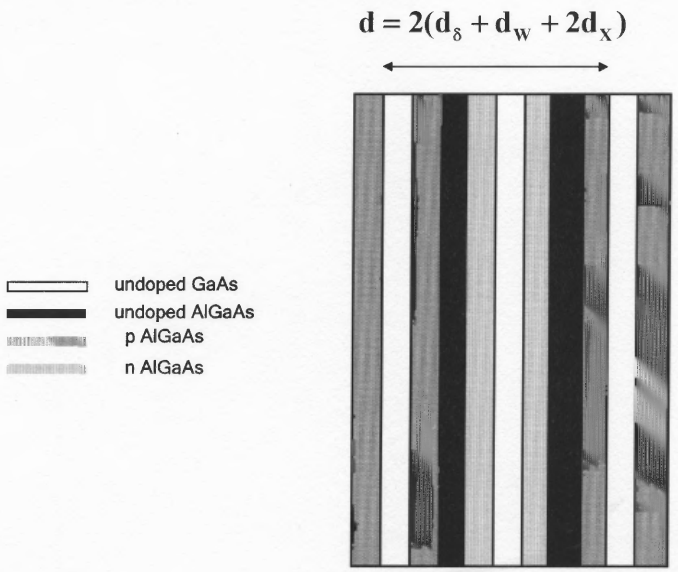

Figure 1.1 An example of a semiconductor superlattice.

1.2 High Temperature Superconductivity

The complexity of high temperature superconductivity brings together expertise from materials scientists, physicists and chemists, experimentalists and theorists to understand, demonstrate, and interpret these phenomena. Much of the research in high-T_C superconductivity has generated other areas of research where complex materials play an important role. The materials could consist of magnetism in the manganites, complex oxides, and two and one-dimensional magnets. Studies of superconductors seems to indicate that the higher the T_C the more complex the material. There has been a considerable effort to find universal trends and correlations amongst physical quantities (superfluid density, conductivity, and the critical temperature) as a clue to the origin of the superconductivity. One of the earliest patterns that emerged was the linear scaling of the superfluid density with the superconducting transition temperature, which marks the onset of phase coherence. However, it fails to describe optimally doped (where T_C is a maximum) or overdoped materials [3].

Theoretical approaches face challenges in identifying a clear avenue for interpreting empirical studies in which material parameters and properties are correlated with superconducting properties [4]. Comparisons of theoretical ideas, which rely only on artificially engineered layered superlattices, will be explored in this study.

The discovery of new superconducting high-T_C cuprates in 1986 by Bednorz and Mueller has played an important role in the advancement of the field of superconductivity research since its inception [5-8]. In MgB_2 superconductors, it was discovered that an in-plane boron phonon mode, that modulates lattice constants and angles within the honeycomb lattice, is responsible for coupling to the conduction electrons and is

the driving force for superconductivity [9]. The modulation of the bond lengths by phonon modes may create distortions in the Wigner lattice that is formed in superlattices after tunneling, thus creating a potential distribution, which may be the mechanism for super current at high temperatures. Studies of novel quantum phases in an unexplored regime of system dimensions and parameters, and nanoscale high-temperature superconducting structures will allow exploration of fundamental mechanisms with unprecedented insight [10]. High-temperature superconductivity in the nanometer scale from the perspective of experiments, theory, and simulation are currently being explored. It is the nanoscale of superconductivity that is the main focus of this study.

Despite the large number of studies and extensive research conducted since the discovery of high-T_C superconductivity in the 1980's, the numerous theories and formulations that have been proposed over the years have not been satisfactory in explaining high temperature superconductivity.

A more recent formulation by Harshman, which is an unpublished theoretical work in progress, considers the optimal structure for superconductivity as having alternating layers of hole-carrying and electron-carrying sheets. The Harshman and Mills [11] formulation for the presence of superconductivity is defined by the parameter $\beta = N_S d^2$ or $\beta = P_S d^2$, where P_S and N_S are the surface carrier densities and d is the spacing between hole or electron layers. When $\beta = 1$, the condition for maximizing T_C occurs. The condition $\beta = 1$ occurs when the mean distance between charge carriers within the sheets equals the distance d between the sheets. Harshman and Mills [1] studied the properties of all the experimental data on high-T_C superconductors which allowed for dynamic charge screening and confinement. The superconductors were

analyzed in terms of layered two-dimensional conducting sheets with Coulomb coupling between the sheets (Figure 1.2). They recognized that high $-T_C$ materials have (solid line in Figure 1.2) $\beta = N_S d^2 = P_S d^2 = 1.0$. It was later noted that alternating carrier layers within the material may be present separated by a periodic distance d that also satisfies $\beta = N_S d^2 = P_S d^2 = 1.0$.

To test this possibility, Harshman and Mills [11] prepared an n-doped GaAs superlattice sample but no signs of superconductivity were present. The resistance, however, was dependent on both temperature and external magnetic fields. The magnetic field affected the slope of the resistance vs. temperature curves as shown in Figure 1.3. At about 3 K, the resistance was field independent. Anomalous curves existed when the magnetic intensity was 4 and 6 Tesla. Even though there was no direct evidence of SC, a 'shadow' of SC was evident in the fact that magnetic fields affect the resistance.

Harshman [12] hypothesized that if a material is both p-doped and n-doped, the formation of alternating carrier layers may induce SC. The alternating carrier layers may trap holes and create a hole distribution that could cause super current.

Alternating layers of hole-carrying and electron-carrying sheets can be described as a Wigner lattice. The lattice is one in which charges on lattice sites interact via a Coulomb interaction in a uniform background of opposite charge, such that there is overall charge neutrality. A Wigner crystalline form for electrons may appear at low electronic densities [13] and it may be energetically feasible for the stationary ions to form a distorted periodic lattice. A distortion creates potential wells in which electrons are trapped in and form a Wigner electron crystal. Together, the periodic bunching of the positive ions and the trapped electrons form a periodic charge density variation. This and

holes trapped by them. Holes create vacancies and high-T_C superconductivity occurs thesis postulates that the periodic potential is the result of a coupling between excitons when the number of vacancies exceeds a certain threshold. If a superlattice nanostructure satisfies the criteria for the Harshman and Mills formulation for optimum superconductivity defined by the parameter $\beta=1$, then the structure is essentially a 3-D Wigner lattice in electrostatic equilibrium. The Wigner lattice forms at carrier densities that are optimized for superconductivity.

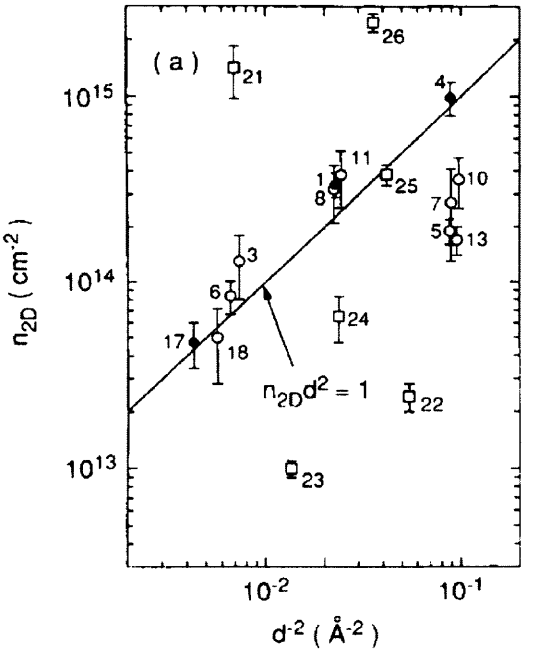

Figure 1.2 The 2-D surface density vs. inverse square separation. The circles represent layered materials that might exhibit HTS. Solid circles have unambiguous geometries and optimized parameters; open circles have ambiguous geometries or insufficient data. (from Figure 10 in Reference 11).

The kinetic energy of the electrons in a Wigner lattice in the low-density limit becomes negligible and the charges arrange themselves resulting in the minimization of the electrostatic energy. The presence of elastic and magnetic effects in real compounds can strongly modify the predicted ordering pattern and the ratio of intraplanar

Coulombic interactions to kinetic energy [14]. Covalent bonding in a 2-D well confinement gives electrons fewer ways of avoiding each other. Strongly interacting electrons tend to maximize their relative distance and minimize their electron energy configuration by forming crystals.

The feasibility of constructing a semiconductor superlattice that obeys the Harshman formulation for superconductivity is examined in this study. Ongoing research in electron-hole pair condensation and the formation of "ghost" hole layers and the consequent coupling in relation to the Harshman formulation, will be discussed [15]. Electron-hole pair condensation, in addition to the strong Coulombic coupling of carrier sheets, may be a contrary factor in achieving equal carrier layers in a superlattice. "Ghost" holes may be the holes trapped by excitons discussed in a later section.

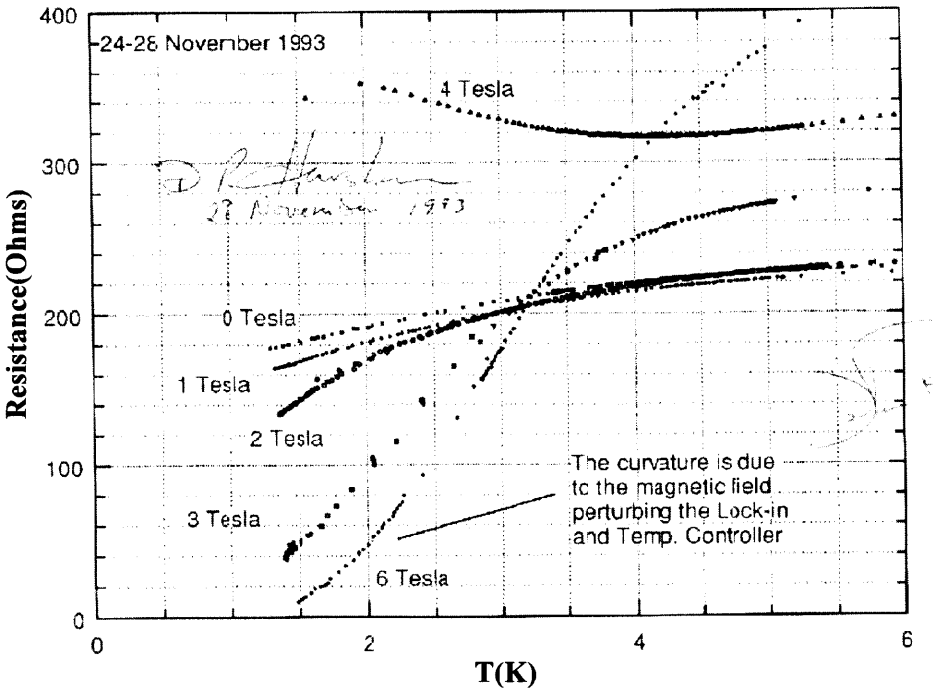

Figure 1.3 Effect of magnetic field on resistance of a GaAs electron superlattice.

1.3 Computer Modeling of Superlattice Nanostructures

In this study, a series of computer simulations were performed to determine the structure and properties of a superlattice when β for pairs of hole/electron wells is between 0.5 and 2. The program employed in the superlattice simulations is a 1-D FORTRAN program developed by Dr. Greg Snider of Notre Dame University [16]. Later, a C version was employed that increased the number of mesh points by two orders of magnitude, thus reducing the occurrence of nonconvergence. Computer simulations are based on an iterative process using Schrödinger-Poisson solvers in which an initial wave function is estimated and the wave function is updated for each cycle (Figure 1.4) until convergence is achieved. The final resulting wave function is utilized to calculate the charge distribution.

The program uses a method of finite differences [17] in one-dimension to create profiles of semiconductor structures for temperatures in the range of 4-300 K. Schrödinger-Poisson (S-P) solvers can be employed for cryogenic temperatures. The drawback is that using the S-P solvers for simulations below 50 K can cause problems with convergence. At what temperatures the S-P solvers option could be discarded is determined later in this section.

The program calculates the conduction and valence bands and the hole and electron concentrations. Dopant ionization is included for both shallow and deep level dopants. Current flow is not calculated and hence the structure can be simulated only in thermal equilibrium. Three possible boundary conditions can de defined for the surface and the substrate: Schottky barrier, Ohmic contact and slope = 0.

A Schottky barrier is defined at the surface or substrate where the default

barrier height is the barrier of the adjacent semiconductor with the option of specifying an applied bias. The Ohmic specifier sets the difference of the conduction and Fermi energy levels $(E_C - E_F)$ at the boundary to the value required for charge neutrality at the boundary. Slope = 0 sets the slope of the bands equal to zero at the boundary. If a Schottky barrier is used, the program can simulate the effect of an applied bias, which does not cause significant current flow. One can assign different Fermi levels to layers in the biased structure as a way of simulating structures under bias. This can be done only if the current flow is small enough to be ignored. If an Ohmic contact boundary condition is specified, the applied bias must match the Fermi level in the adjacent layer. The slope = 0 boundary condition is used when only a certain region of interest is to be simulated.

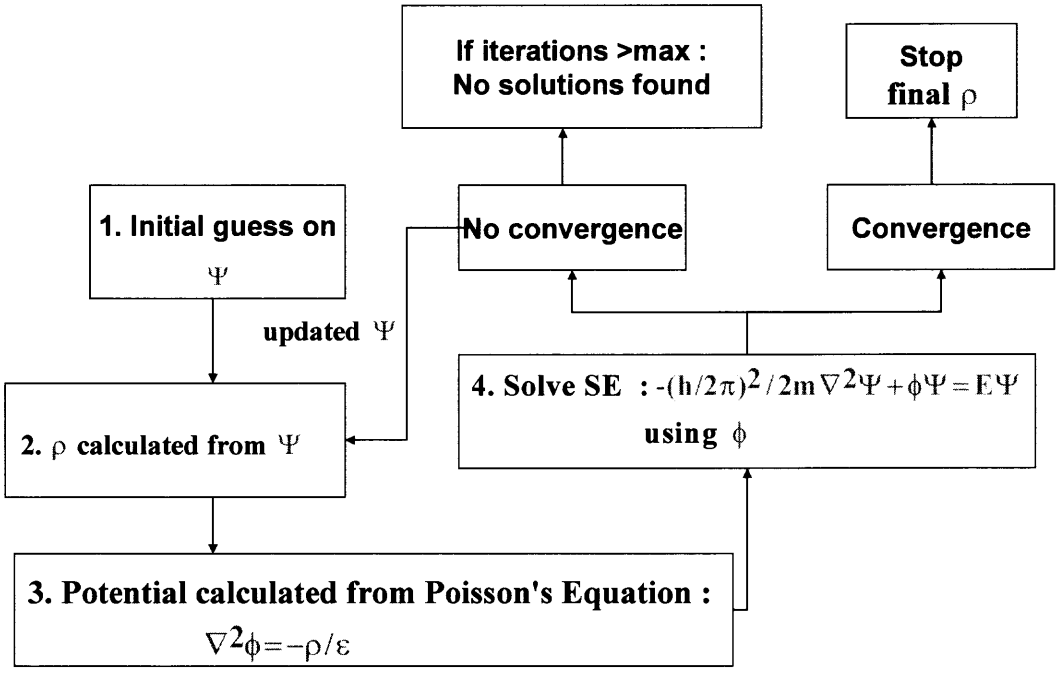

Figure 1.4 Flowchart of the Snider computer program.

For the superlattices used in the simulations, one can expect significant band bending if the doping is in a wider bandgap material. The band bending is tied to charge density in the wells, and one affects the other. The band bending will also affect charge transfer between wells. 1D Poisson calculates the band diagram based on doping and boundary conditions. Thus it inherently calculates the band bending.

Poisson's Equation relates the electrostatic potential to the charge distribution, but is useful by itself only with explicit knowledge of the charge distribution. When augmented by assumptions relating the charge density to the electrostatic potential, a screening equation can be derived. Universal electrostatic behavior in such situations is that the charges tend to move so as to reduce the magnitude of the electric field. Calculating the charge density from the bulk density of states and with the assumption of a local quasi-equilibrium described by Boltzmann statistics leads to Debye screening. Using the bulk density of states with Fermi-Dirac statistics, the result is Thomas-Fermi screening. Without utilizing the bulk density of states, but using the bound states from the Schrödinger Equation, and weighing them by a Fermi-Dirac distribution, results in a Hartree screening. Hartree calculation is the same as a "Schrödinger-Poisson solver". In a modulation-doped structure, this sort of calculation is useful when applied in the epitaxial growth direction for determining the surface carrier density. It is not usefully applied in the transport direction because the unbounded scattering solutions of the Schrödinger Equation have an "anti-screening" behavior, which prevents convergence to any meaningful results.

Modeling of heterostructures has indicated that one usually has to go to cryogenic temperatures in order to see a significant difference in the results. The plots at 10 K are shown in Figure 1.5. The figures show comparisons of Hartree (left) and Thomas-Fermi

(right) screening in an undoped AlGaAs-GaAs heterostructure at a temperature of 10 K. The green lines show the energy and approximate spatial distribution of the quantized states. The boundary between the AlGaAs and GaAs is the vertical black line. To the left is GaAs and to the right is AlGaAs. The charge distribution due to the evanescent tails of the wave functions is apparent in the Hartree case. In the plots, note that the potential reaches a deeper minimum in the Hartree case, because the lowest electron state lies at an energy well above the bottom of the potential well. Since there is no significant difference between the Hartree and Thomas-Fermi screening for T > 10 K, one can "turn off" the S-P option down to just above T=10 K if convergence problems occur.

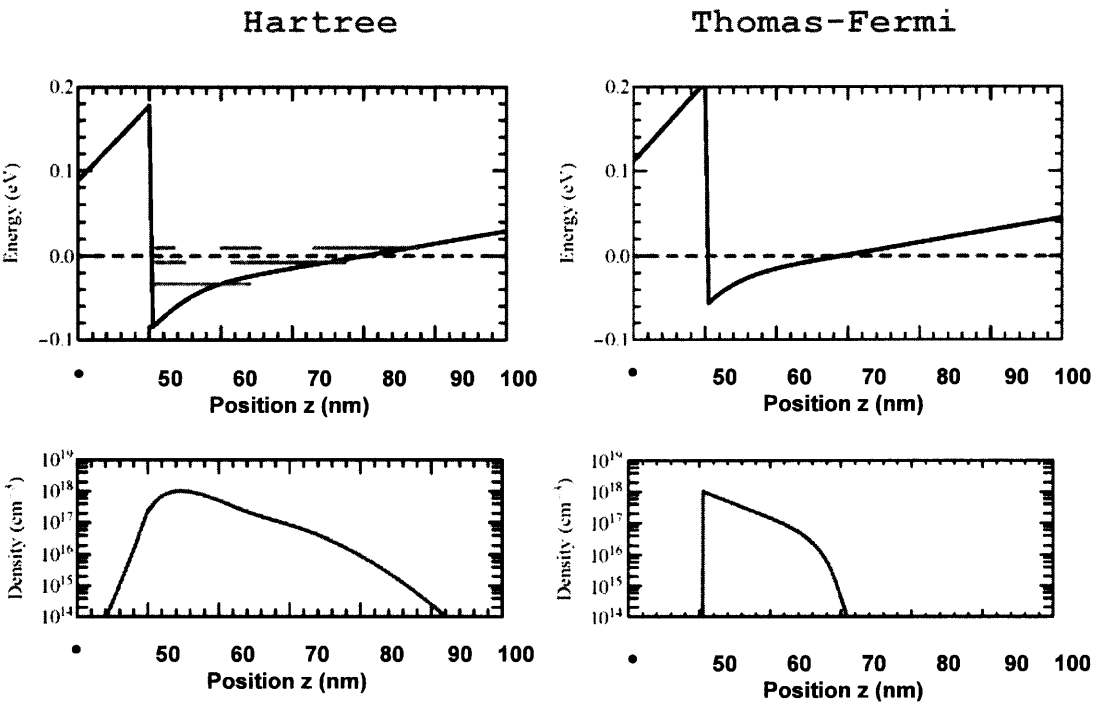

Figure 1.5 Hartree and Thomas-Fermi plots of electron energy and density of carrier states.

CHAPTER 2

THEORY

2.1 BCS Theory of Superconductivity

Bardeen-Cooper-Schrieffer (BCS) theory is a comprehensive theory that explains the behavior of superconducting materials. The theory successfully explains the ability of certain metals at low temperatures to conduct electricity without resistance. BCS theory views superconductivity as a macroscopic quantum mechanical effect. It proposes that electrons with opposite spin can become paired; creating two bound electrons called Cooper pairs. BCS theory states that the binding of Cooper pairs is a result of the electron-phonon interaction, which causes an attraction between electrons, thus overcoming the Coulomb repulsion. During the electron-phonon interaction, phonon energy can be gained or lost by the electron. Since the difference of the incident and scattered wave vectors of the electrons are not equal to a reciprocal lattice vector, the scattering amplitude is less than maximum thus increasing the degree of forward supercurrent. The electron-phonon interaction temporarily binds electrons in a lattice and supplies a means by which the energy required to separate the Cooper pairs into their individual electrons can be measured experimentally.

The Cooper pairs are formed when an electron moving through a conductor causes a slight increase in concentration of positive charges in the lattice around it; this increase in turn can attract another electron. In effect, the two electrons are then held together with a certain binding energy. If this binding energy is higher than the energy provided from oscillating atoms in the conductor, then the electron pair will stick together, thus not experiencing resistance. Since the electrons are bound into Cooper

pairs, a finite amount of energy is needed to break these apart into two independent electrons indicating an energy gap which separates the Cooper electron pairs after superconductivity vanishes. This energy gap is highest at low temperatures but vanishes at the transition temperature when superconductivity ceases to exist.

Conventional superconductors are materials that display superconductivity as described by the BCS theory for its extensions. Mercury was the first conventional superconductor and was discovered at the beginning of the last century. Most conventional superconductors are single elements or binary alloys. Their critical temperatures are low but some binary alloys have a critical temperature up to 23 K [18].

2.2 The Harshman Formulation and Conditions for Superconductivity

The high temperature superconductors were first discovered in 1986 by Bednorz and Mueller [19] and continue to pose very fundamental questions for Condensed Matter physicists to address. Seemingly, they are not likely candidates for superconductors, since basically they are insulators. However, by adding charge carriers by chemically doping them, they become superconductors with transition temperatures of up to 135 K, which is well below room temperature but is very high for a quantum mechanical state to dominate the properties.

The Hubbard model can be employed as an approximation to describe the transition between conducting and insulating systems. The Hubbard Model is a commonly used approximation for the behavior of electrons on a lattice that assumes an onsite-only repulsive interaction and allows hopping between adjacent sites. Investigations into the Hubbard model arise from the copper-dioxide planes including the oxygen atoms, and find important departures from the behavior of the Hubbard

model. In the low doping limit, a quantum paramagnet is stabilized, and not a ferromagnet. The Hubbard model can explain asymmetry in the electron- and hole-doped phases, since the electron doped materials are necessarily described by the Hubbard model [20].

A fundamental mechanism for superconductivity arises from the interaction of a hole with the outer electrons in atoms with nearly filled shells. Superconductivity results from the pairing of hole carriers, and is driven by the fact that paired holes can propagate more easily (have a smaller effective mass) than single holes with a lower kinetic energy. Single electrons propagate freely and do not pair. Dynamic Hubbard models describe the different physical phenomenon of electron and hole carriers in metals. The reason for the increased mobility of holes upon pairing is that they 'undress' when they pair, and turn into electrons. This leads to a new understanding of superconductors which considers a superconductor as a giant atom and implies that the electron-phonon interaction is not a factor in HTS superconductivity and the BCS theory is not applicable.

The theory of superconductivity asserts that superconductivity can only occur when hole carriers exist in the normal state of a metal. The formation of holes is the key mechanism for superconductivity, since holes resulting from unfilled covalent bonds do not repel as electrons do. There is a difference between electrons and holes in energy bands in solids from a many-particle point of view, originating in the electron-electron interaction and it has fundamental consequences for superconductivity. The difference between electrons and holes parallels the difference due to electron-electron interactions. Superconductivity may originate in 'undressing' of carriers [21]. Electrons at the Fermi surface give rise to high conductivity and normal metallic behavior. Holes at the Fermi

surface yield poor conductivity and give rise to superconductivity [22].

In order to test for superconductivity when the Coulombic hole-exciton coupling correlation factor is dominant, it has been suggested to test a 2-dimensional electron gas produced in a GaAs superlattice. The hole-exciton coupling is a hypothetical mechanism which occurs when holes are trapped by excitons and may be the source of supercurrent at high temperatures. Excitons form as a result of alternating carriers layers in a superlattice.

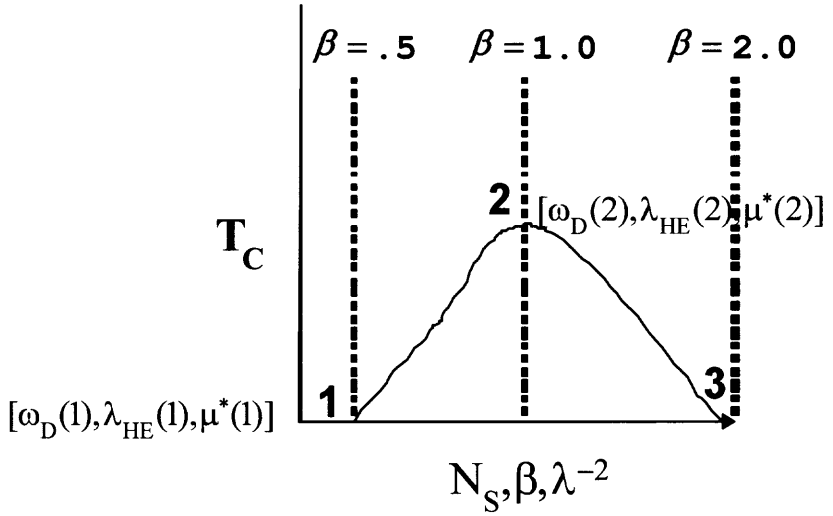

Figure 2.1 Critical temperature vs. sheet carrier density. The sketch is qualitative and represents the concept behind experimental findings and proposals of the Harshman and Mills analysis of titration experiments.

Harshman and Mills [23] suggested that layered high-T_C superconductors have alternating sheets of holes and electrons whose net charge must be equal to zero to preserve charge neutrality. It was deduced, from observations on experimental data, that a sketch could be used to show the relationship between T_C and β or between T_C and N_S. T_C is proportional to the Fermi Energy E_F, in a 2-D system since $T_C \propto d/\lambda_L^2$, where $\lambda_L \propto (d/E_F)^{1/2}$. One can thus create a corresponding plot of T_C and the inverse

square of λ_L. Knowing the surface hole density for $\beta = 1.0$, the London penetration depth can be calculated.

In addition to using the results of computer simulations to test the superconducting hypothesis in superlattices, this thesis will propose a novel theoretical understanding of the Harshman Model and how it connects to BCS theory. A trial function, containing a new coupling other than the electron-phonon coupling, will be utilized in the next sections to explain the Harshman sketch in Figure 2.1.

For a layer with a surface charge density N, the average near neighbor distance in the x and y directions between atoms is $1/\sqrt{N}$. If two layers with surface charge density N are separated by d, then the near neighbor spacing in the x, y, and z directions within the layers equals d and $\beta = Nd^2 = 1$. If alternating layers of carriers are coupled and separated by d, carriers will redistribute themselves so as to minimize the resultant electric field on each carrier. This geometry is the structure that is associated with the Wigner 3-D lattice at temperature T_C.

In most cases, it is unphysical to assume the existence of strong attractive interactions which indicates the presence of a weak Coulomb correlation. Coulombic correlation suggests that a 2-D Wigner lattice must exist in layers within the semiconductor material. A 2-dimensional electron gas between layers within a superlattice is the criterion for the formation of a Wigner lattice. The correlation to HTS and conventional BCS theory is discussed in the following sections.

The formulation $\beta = 1.0$ for maximal T_C is an observational equation that suggests that the dominant interaction is a Coulombic interaction, which is in contrast to the predominant electron-phonon correlation λ_E and Coulombic interaction μ for BCS

superconductivity. Layers of coupled alternating holes and electrons may contain the indirect excitons which could capture holes. In BCS theory, the positive charge distribution is caused by the distortion of the lattice structure by incident electrons. The positive charge distribution in the Harshman formulation may result from the accumulation of holes within excitons which in turn causes supercurrent.

Bardeen-Cooper-Schrieffer (BCS) theory postulates that the predominant mode of interaction in a Cooper pair is the electron-phonon correlation in which the critical temperature T_C is obtained from:

$$k_B T_C \approx \hbar\omega_D exp[-1/(\lambda_E - \mu)] \tag{2.1}$$

Phonons can distort the local crystal lattice and the local band structure. The conducting electrons are "sensed" by the lattice distortion [24].

However, for high-T_C, the electron-phonon coupling is too weak to explain the formation of Bosonic states from electron Fermions at high temperatures, but phonon renormalization cannot be entirely discarded in explaining HTS. Phonon renormalization is still important since phonons are within the critical energy range in the binding of Cooper pairs via charge fluctuations [25]. Electron-phonon coupling strongly influences the electron dynamics in high temperature superconductors and should be included in any microscopic theory of superconductivity [26].

Hypothetically, one could, however, explain the nature of the sketch qualitatively using conditions and equations derived from $low-T_C$ BCS theory by replacing the electron-phonon coupling λ_E with another term λ_{HE} resulting from another mechanism. The mechanism may involve the trapping of holes by indirect excitons.

As β increases (Figure 2.1), more holes may be trapped by indirect excitons. The source of the trapped holes may be the positive charge distribution caused by the electron-phonon interaction and the periodic positive charge distribution inherent in a Wigner lattice. The density of the trapped holes and λ_{HE} reaches a maximum at $\beta = 1$ since the net electrostatic forces on all charges, including the holes within the excitons, are at a minimum.

According to renormalization group (RG) theory, the Coulomb correlation is calculated by multiplying the interaction strength by the density of states and the renormalized value is [27]:

$$\mu^* = \mu/(1 + \mu \log[E_F/(\hbar\omega_D)]) = \mu/(1 + \mu \log[N_S\pi\hbar/(m^*\omega_D)]) \qquad (2.2)$$

where $E_F = N_S\pi\hbar^2/m^*$. Using $m^* = 0.15\text{x}9.1\text{x}10^{-31}$ kg, $h = 6.62\text{x}10^{-34}$ joules-sec, the argument in the log component of the equation above is $0.00242\, N_S/\omega_D$. A varying ω_D can affect the T_C so phonon modes can influence the critical temperature.

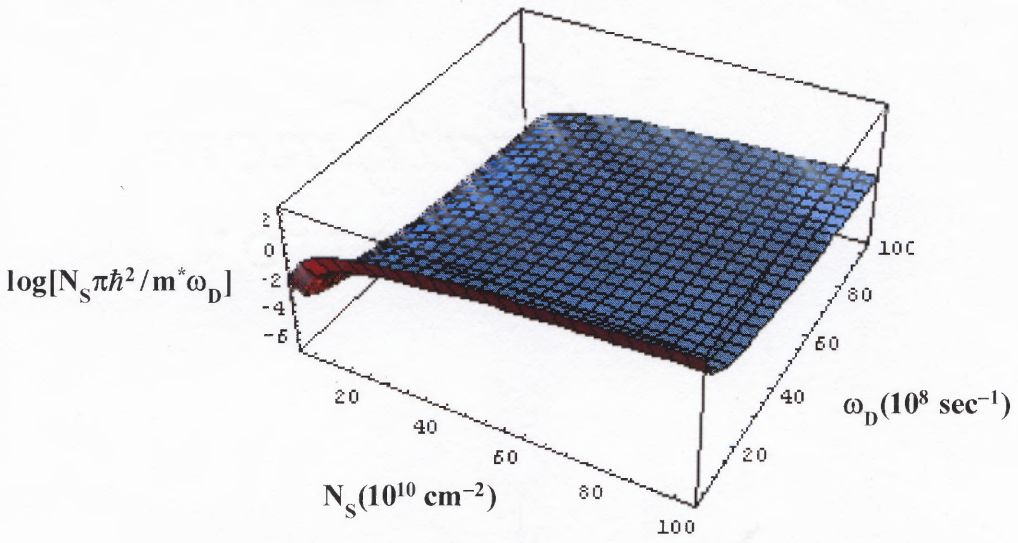

Figure 2.2 3D plot of argument of coulomb correlation vs. surface carrier density and the Debye frequency.

Decreasing ω_D can promote the value of the critical temperature since μ^* decreases as $\log[N_S\pi\hbar/(m^*\omega_D]$ increases. In Figure 2.2, $\log[N_S\pi\hbar/(m^*\omega_D]$ has an upward slope that assumes a greater positive value as N_S increases from $10x10^{10}-100x10^{10}$ carriers cm^{-2} and as ω_D decreases from $100x10^8-1x10^8$ sec^{-1}. However, from points 1-2 in Figure 2.1, the near neighbor distances decrease as β increases. Therefore, μ^* is an increasing function of β. This would require that ω_D increases faster than N_S. As ω_D increases, the first factor in T_C increases but an increasing ω_D in the exponential function of the second factor in T_C would tend to have a much greater effect in decreasing T_C. When β varies from 0.5 to 2.0 in the Harshman sketch, the rates of change of λ_{HE}, ω_D and μ^* determine how T_C advances.

If the Coulomb correlation μ^* is dominant ($\lambda_{HE} - \mu^* < 0$), then the instantaneous interaction is repulsive. According to standard RG analysis, when $\hbar\omega_D < k_BT_C$, the weak coupling estimate of the pairing scale T_C is $k_BT_C \propto \hbar\omega_D \exp[-1/(\lambda_{HE} - \mu^*)]$. As N_S increases from point 1 to point 2 on the Harshman sketch, λ_{HE} and $\exp[-1/(\lambda_{HE} - \mu^*)]$ may both increase since the indirect excitons, formed as a result of the charges layers, are capturing more holes and thereby promoting the hole-exciton coupling. A maximal point for T_C is reached at point 2 when a change in N_S results in a reduced T_C. In order for T_C to be at a maximum at point 2, there are several possible conditions. The following conditions to be satisfied are the most probable:

$$\omega_D(2) > \omega_D(1),\ \lambda_{HE}(1) < \lambda_{HE}(2),\ \mu^*(1) < \mu^*(2),\ d\lambda_{HE}/d\beta > d\mu^*/d\beta,\ d\omega_D/d\beta > dN_S/d\beta.$$

The dependence of T_C on ω_D can be shown to be: (see Appendix A)

$$d\log[k_B T_C]/d\log[\hbar\omega_D] = 1-(\mu^* \log[k_B T_C/\hbar\omega_D])^2 \quad (2.3)$$

If $\hbar\omega_D < k_B T_C \exp[-(1-\lambda_{HE})/(\lambda_{HE}\mu)]$, $d\log[k_B T_C]/d\log[k_B\omega_D] \cong 1.0$, then the critical temperature T_C is a linearly increasing function of ω_D in the region between points 1 and 2 on Harshman sketch. When $\hbar\omega_D > k_B T_C \exp[1/\mu^*]$, T_C becomes a decreasing function of ω_D in the region between points 2 and 3 on the Harshman sketch.

According to Harshman formulation, superconductivity exists when β lies between 0.5 and 2.0. At $\beta = 0.5$ (point 1 in Figure 2.1), T_C is at its minimum and near-neighbor distances of the carriers are at a maximum. At $\beta = 1.0$ (point 2 in Figure 2.1), the electrostatic interactions are at a minimum and the carriers are equally spaced. In addition, the electrostatic forces on all hole carriers captured by excitons are balanced. The number of Bosonic pairs and captured holes could now be maximal due to the alignment of excitonic pairs. When $\beta = 2.0$, T_C and near-neighbor distance of the carriers at a minimum, but now the and their interactions in the x-y plane are at maximum and again in a state of electrostatic nonequilibrium.

The Harshman model postulates that, in order to exhibit HTS, a superlattice design must satisfy certain condition according to the model. In designing a functional GaAs-AlGaAs superlattice, the preferable superlattice structure must have the following properties: (1) β is equal to 1 at T = 0 K. (2) The maximum tolerable electric field E_{MAX} in the superlattice is less than limit of $E_{TOL} = 5\text{x}10^5$ V/cm and a maximum sheet resistance of $R_S = 10^4$ Ohms. (3) N_S and P_S are about equal. (4)

Lowest sensitivity of P_S and N_S to variations in N_D and N_A (expressed as a % change in P_S and N_S for a % change in N_D and N_A). (5) An optimal alloy concentration x in $Al_XGa_{1-X}As$. In addition, one must consider the electronic structure of the superlattice: mobile holes and fixed acceptor ions, mobile holes and mobile acceptor ions, mobile acceptor ions and fixed donor ions. From a more practical aspect, the continuous scaling down of the feature sizes in superlattice structures leads to an increase in power dissipation per unit area of the semiconductor chip [28] in which the influence of size effects on thermal conductivity becomes extremely important for device design and reliability [29].

At high temperatures, symmetrical charge densities are produced and nearly complete ionization ($N_D^+ \cong N_D$, $N_A^- \cong N_A$) occurs. The thickness of the spacer layer between GaAs wells, d_X, is determined by the constraint $d_X = E_{GS}/E_{TOL}$, where E_{GS} is the energy gap in the GaAs layer. Poisson's Equation $\nabla \cdot E_{IND} = 4\pi q N_D^+/\varepsilon$ leads to E_{IND}, in terms of the ionized charge layers, and thus leads to $N_D^+ = \varepsilon \nabla \cdot E_{IND}/4\pi q = \nabla \cdot E_{TOL} d_X/4\pi q$.

According to the Harshman formulation, the feasibility for superconductive pairing of electron-hole pairs, assumes alternating 2D electron and hole gasses of densities N_S and P_S where $N_S \approx P_S$, $N_S = \beta / d^2$ with $\beta \approx 1$ (if $E_{IND} < E_{TOL}$). E_{TOL} is the maximum electric field tolerance in a superlattice. Satisfying the criteria $\beta = 1.0$ would mean finding the minimum d. Material properties, primarily the internal dielectric strength of the undoped $Al_xGa_{1-x}As$ spacer layer, impose a practical upper limit on the built-in electric field E_{TOL}. Thus the constraint $E_{IND} < E_{TOL}$, becomes

equivalent to a constraint on the spacer width, expressed as $d_X \geq E_{GS}/E_{TOL}$. A minimum d_X imposes a minimum allowable length for the superlattice period, expressed as $d > d_{MIN}$, where $d_{MIN} = 2(E_{GS}/E_{TOL} + E_W + E_\delta)$. Expressing the superlattice period in the form $d = 2\beta_X d_X$, where $\beta_X = 1+(d_W + d_\delta)/d_X$, yields $N_S = \beta/(4\beta_X^2 d_X^2)$. One can minimize the induced electric field on the surface of the carrier layers by adjusting d_X, d_W and d_δ. If $d_X >> d_W, d_\delta$, $\beta_X = 1$ and if all layer widths are equal ($d_X = d_W = d_\delta$), then $\beta_X = 3$. Choosing equal layer widths could thus minimize the induced electric field on the surface of the carrier layers if d_X is kept constant.

The superconducting transition temperature can be calculated from the Fermi energy of the 2D electron gas, $E_F = \pi\hbar^2 N_S/m_E^*$ and $T_C = \beta_3 E_F/k_B$, where $\beta_3 = 0.267-0.359$ and m_E^* is the electron effective mass. The variation of β_3 $(0.267-0.359)$ is necessary since the calculated T_C must be consistent with the formula for the critical temperature as is given at the end of this paragraph. It is assumed at this point that the expression, above, for the critical temperature can be applied for alternating carrier layers as well as superconductors with a periodic distance of d. The maximum critical temperature can now be estimated: $T_C = 1.1\text{x}10^4\beta/(m_C d^2)$ where d is in Angstroms and m_C is the effective mass coefficient. If d = 800 Angstroms and if $m_C = m_E^*/m_0 = 0.06$, which is the approximate effective mass coefficient for AlGaAs, then T_C = 1.8-2.4 K. This is a lower Figure than in the cuprates, for example, because a minimum value of d_X is determined by how great a field in the spacer can be tolerated. T_C is inversely proportional to the inverse square of d. The very magnitude of d

sets an upper limit on the superconducting transition temperatures. Superconducting transition temperatures are also estimated from the expression $kT_C = 0.25\,\hbar\Omega\,[\exp(2/\Lambda) - 1]^{-1/2}$, where $\hbar\Omega$ is the sum of the hole and electron eigenvalues. This T_C is a generalization to strong coupling ($\Lambda \sim 2 - 3$) and is consistent with experiments on high-T_C superconductors.

The Harshman sketch (Figure 2.1) is qualitative and is based on observational data and must be consistent with $T_C \propto 1/m_C$. The sketch itself cannot be taken as completely accurate since T_C must be close to zero at points 1 and 3, corresponding to $\beta = 0.5$ and 2.0 respectively. This implies that the effective masses at these points must be orders of magnitudes greater than at point 2 when $\beta = 1.0$. Until recently, for doped semiconductors, decreases in the layer thickness of the superlattice has resulted in a small reduction of the effective mass by a few percentage points [31]. Cleaved-edge overgrowth techniques, however, have led to structures with twice the effective electron mass in two-dimensions [32]. Effective masses in $YbAl_3$ can be shown to be dependent on magnetic fields and disorder, [33] and to what extent magnetic fields and disorder can promote the critical temperature by reducing the effective masses of holes and electrons remains uncertain.

The evolution of hole and electron densities may differ given identical parameters if certain conditions are met (Section 2.3). There may be numerous factors that contribute to the difference between the formation of holes and electrons. One factor is that tunneling of holes and electrons differ because they have different effective masses and mobilities. Another factor is the geometry and design of a superlattice.

Electrons flowing into the GaAs wells surrounded by n-doped AlGaAs form more slowly because the accumulating electron buildup within the well restricts further increases in the free electron density. Electrons flowing out of the GaAs wells surrounded by p-doped AlGaAs have hole densities that form more rapidly because the electronic outflow is directed away from the well in two directions and tunnel throughout the entire superlattice and whose accumulations are not highly localized. Hole densities evolve differently than electron densities, making it difficult to achieve equal and alternating carrier densities, one of the criteria of the Harshman formulation.

The ternary value of AlGaAs may adversely affect tunneling during ionization. The problem may be due to physical mechanisms and/or due to limitations in the Snider program. As the alloy concentration decreases, the electrostatic energy configuration of the Al and GaAs ions increases, making the system more disordered. This causes a "roughness" at the boundary of the AlGaAs/GaAs interface. When ionization energy is transferred at the Fermi level, the results may be a huge increase in the carrier concentration. The superlattice structure that is being simulated is very sensitive to the surface and substrate boundary conditions because it is nearly charge neutral with respect to the fixed charge. For low x, if electrons form in the first and last well, holes form in the central wells to balance this negative charge. The wells are too shallow to get carriers in alternating wells. By contrast, in the x = 0.4 case, the wells are deep enough to get carriers in alternating wells.

Given two kinds of ions, Al_xGaAs_{1-x} interacting via Coulomb interactions within the plane, the problem is to determine how the ions, and hence the carriers, are arranged on a 2D lattice at different concentrations. The long range Coulomb interaction couples

all pairs of ions and it is not possible to obtain analytic calculations. Thus, one must resort to computer simulations.

Despite the difficulties in determining the exact nature of a Wigner lattice, computer simulations using the Monte Carlo method, together with simulated annealing, can be used to ascertain the minimum energy configuration for a 2-D triangular lattice (Figure 2.3), alternating straight chains (Figure 2.4 a) or a zig-zag structure (Figure 2.4 b). At a given alloy concentration x, the structures are chosen initially at random at a high initial temperature. For a state of lowest energy, x takes on a value of 0.4 for infinite long chains and a value of 0.5 for a zigzag structure. The ternary used in the simulations for this study was 0.4. Choosing a ternary greater than 0.4 leads to increased overlapping and offsets of the valence and conduction energy bands.

There are two general classes of nonrandom structures and are symmetric about the concentration $x = 1/2$ as shown in Figure 2.4. For $x < 1/3$, like ions stay apart at a maximum distance and hence form a dilute triangular lattice at low x. This is effectively a Wigner lattice and the energetics of the 2D Wigner lattice with a continuum background for charge neutrality agree very well with simulation results at small x.

According to Harshman's hypothesis, T_C can be increased if there are equal and alternating layers of electrons and holes. At $\beta = 1$, the electrons and holes in a superlattice are equally spaced in all directions and hence are in a state of minimum electrostatic equilibrium. A minimum electrostatic energy configuration of Al and GaAs ions before ionization and for carriers after ionization, are correlated with equal and alternating carrier layers – one of the criteria of the Harshman model for SC.

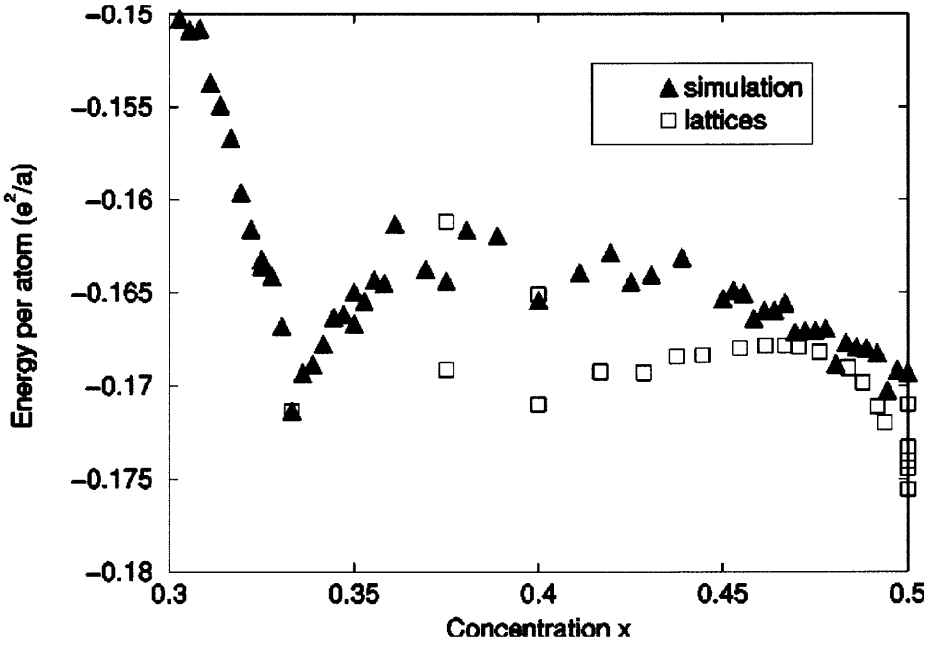

Figure 2.3 The energies for computer simulated noncrystalline structures (solid triangles) and regular superlattice structures (open squares) (from Figure 9 in Reference 30). The charges in the triangular lattice is e and the lattice spacing is a.

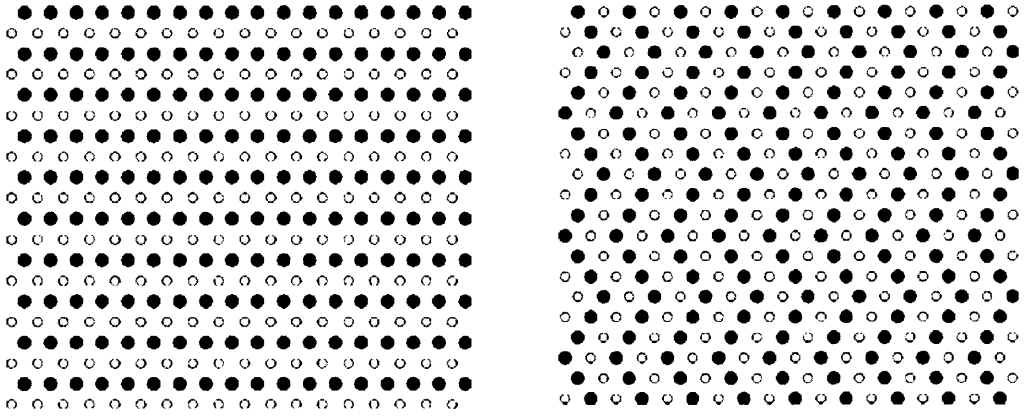

(a) (b)

Figure 2.4 (a) The lowest energy structure has alternating infinite straight chains of ions at x = 0.4 (from Figure 7 in Reference 30), (b) A zigzag structure at x = 0.5 (from Figure 8 in Reference 30).

2.3 Electron-Hole Formation in Superlattice GaAs-AlGaAs Wells

Consider a GaAs well surrounded by two doped AlGaAs barriers. The n and p densities in three dimensions can be expressed as follows:

$$n = 2\sqrt[3]{2\pi m_E^* k_B T / h^2}\, exp[-(E_G - E_F)/k_B T] \tag{2.4}$$

$$p = 2\sqrt[3]{2\pi m_H^* k_B T / h^2}\, exp[(-E_F)/k_B T] \tag{2.5}$$

Since $m_H^*/m_E^* = 2.2$ for a GaAs-AlGaAs superlattice, then $p > n$ and charge carrier densities evolve unequally.

The difference in energy between the two wells is [34]:

$$V(k) = E_G = E_C^B + \hbar^2 k^2/(2m_{AlGaAs}) - (E_C^W + \hbar^2 k^2/(2m_{GaAs}))$$

$$= \Delta E_C + (\hbar^2 k^2/2)(1/m_{AlGaAs} - 1/m_{GaAs}) \tag{2.6}$$

If the wells are of the same width, the wavenumbers for each well would be equal.

For high T [35]:

$$E_F = E_G - k_B T ln[N_C/N_D] = \Delta E_C + \hbar^2 k^2/2(1/m_{AlGaAs} - 1/m_{GaAs}) - k_B T ln[N_C/N_D] \tag{2.7}$$

For low T:

$$E_F = E_G - 1/2(E_D + k_B T ln[N_C/N_D])$$

$$= \Delta E_C + (\hbar^2 k^2/2)(1/m_{AlGaAs} - 1/m_{GaAs}) - 1/2(E_D + k_B T ln[N_C/N_D]) \tag{2.8}$$

where m_{AlGaAs}, m_{GaAs} are the electron effective masses in AlGaAs and GaAs wells, respectively.

For low and high temperatures, substituting E_F above into Equations 2.4 and 2.5, yields an expression for density of holes and electrons. Factors other than effective masses influence carrier evolution. For holes, the wavenumber is a factor in the hole density, whereas for electrons it is not. Hole evolution is also affected by differences

in the inverses of the effectives masses of carriers in the GaAs and AlGaAs wells.

For low T:

$$p = 2\sqrt[3]{2\pi m_H^* k_B T/h^2}\exp[(-E_F)/k_B T]$$

$$= 2\sqrt[3]{2\pi m_H^* k_B T/h^2}\exp[-(\Delta E_C + (\hbar^2 k^2/2)(1/m_{AlGaAS} - 1/m_{GaAs})$$

$$-1/2(E_D + k_B T\ln[N_C/N_D]))/k_B T] \tag{2.9}$$

$$n = 2\sqrt[3]{2\pi m_E^* k_B T/h^2}\exp[-(E_G - E_F)/k_B T]$$

$$= 2\sqrt[3]{2\pi m_E^* k_B T/h^2}\exp[-1/2(E_D + k_B T\ln[N_C/N_D])/k_B T] \tag{2.10}$$

For high T:

$$p = 2\sqrt[3]{2\pi m_H^* k_B T/h^2}\exp[(-E_F)/k_B T]$$

$$= 2\sqrt[3]{2\pi m_H^* k_B T/h^2}\exp[-(\Delta E_C +$$

$$\hbar^2 k^2/2(1/m_{AlGaAs} - 1/m_{GaAs}) - k_B T\ln[N_C/N_D])/k_B T] \tag{2.11}$$

$$n = 2\sqrt[3]{2\pi m_E^* k_B T/h^2}\exp[(-(E_G - E_F)/k_B T]$$

$$= 2\sqrt[3]{2\pi m_E^* k_B T/h^2}\exp[\ln[N_C/N_D]] \tag{2.12}$$

Equations 2.9 and 2.10 are valid in the limit as T approaches 0 (see Appendix B).

The exponential nature of the hole and electron density evolution would result in a non-linear response of the densities to changes in the doping concentration and layer widths. Varying doping concentrations and layer thicknesses can change the effective masses of electrons and holes. Table 3.9 shows that at certain layer widths and doping concentrations β can change exponentially, indicating the existence of a threshold in carrier density evolution.

Since $k = n\pi / L$, where L is the layer thickness, as L increases, k decreases. As the layer thickness increases or decreases from Equation 2.6, the potential difference between adjacent wells V(k) may decrease or increase, depending upon the effective masses change. Thus, more or fewer electrons can tunnel out of the GaAs well. As more or less electrons tunnel from the GaAs well into the p-doped AlGaAs as a result of the varying V(k), positive ionic cores are created or disappear. The result causes the drag or pull on the electrons in the well and thus affecting the effective mass. A small change in the term $1/m_{AlGaAs} - 1/m_{GaAs}$ can greatly affect the density of hole states and thus β changes. Changing hole density and keeping temperature constant can lead to a change in the slope of β vs. temperature. Since β is $P_S d^2$, the ratio of sheet hole densities at points 1 and 2 on β vs. T curves, at some specified temperature, is given by β_2/β_1.

The increase in β with increases in donor concentrations can be explained as follows. When two semiconductor layers are in contact, the occupation probability P for an electron of energy E_i in semiconductor i is $P(E_i) = f(E_i) = 1/[(\exp(E_i - \mu)/kT] + 1)$ where $f(E_i)$ is the Fermi-Dirac distribution function. The density of electron states in semiconductor i is n_i. The product of the two is the density of available states.

Let the difference in energy levels of two semiconductors be V, so $E_2 = E_1 + V$, where E_1 and E_2 are the energies of the electrons in semiconductors 1 and 2 respectively. In semiconductor 2, the rate of tunneling $R(E_2)$ into semiconductor 1 is directly proportional to the number of unoccupied states in semiconductor 1. By Fermi's Golden Rule, it is $R(E_2) \propto |M|^2 [1 - f(E_1)] n_1(E_1)$, where $\rho(E_1)$ is the density of available hole states in semiconductor 1 at energy E_1 and M is the tunneling

amplitude. The value of $\rho(E_1)$ is the product of the density of electron states and the probability that an electron state is unoccupied and is given by $\rho(E_1)=[1-f(E_1)]n_1(E_1)$. Thus the rate of tunneling from semiconductor 2 into semiconductor 1 as a function of the electron's energy E_1 is $R(E_2) \propto |M|^2 [1-f(E_1)]n_1(E_1)$.

The total number of electrons at energy E_2 in semiconductor 2 that might tunnel is $n_2(E_2)f(E_2)$, where n_2 is the density of electron states in semiconductor 2. The tunneling of electrons from semiconductor 2 to semiconductor 1 is proportional to the product of the density of available holes in semiconductor 1 ($\rho(E_1) = [1-f(E_1)]n_1(E_1)$) and the density of electrons in semiconductor 2. Integrating over all possible energies E, the current from 2 to 1 is:

$$I_{2,1} = -eK \int_{-\infty}^{+\infty} n_2(E_1+V) f(E_1+V) n_1(E_1)(1-f(E_1))dE_1 \qquad (2.13)$$

where K is a constant that depends on junction geometry.

CHAPTER 3

RESULTS OF COMPUTER SIMULATIONS OF SUPERLATTICES

3.1 Sensitivity of the Electron-Hole Superlattice to Parametric Changes at Low Temperatures

This section will examine the sensitivity of the Snider program to test superconductivity as per the Harshman formulation in a $GaAs/Al_xGa_{1-x}As$ semiconductor structure at low temperatures. Simulations will show that the Snider program accurately simulates changes in physical variables, including the induced electric field and sheet resistance, as the layer widths and doping concentrations in the superlattice are varied. Simulations will be based on a doped $GaAs/Al_xGa_{1-x}As$ superlattice structure (Figure 3.1) with GaAs wells surrounded by alternating doped layers. The computer program will simulate the formation of alternating sequence of electron- and hole-populated quantum wells in the $GaAs/Al_xGa_{1-x}As$ semiconductor structure. A series of superlattice structures meeting this criterion for superconductivity are studied by self-consistent numerical simulations.

Four different cases in this section were studied in which physical parameters were varied to show the effect they have on induced electric field, sheet resistance, and carrier densities. Varying the alloy concentration x in the region x = 0.14-0.29, resulted in simulations that rarely converged and it was decided that achieving alternating equal carrier surface densities for these ternary values were not feasible. Attempts to create a table using modulation doping were not successful since equal alternating carrier layers were impossible to achieve. The hole effective mass m_H^* used in Snider's data is 0.15

m_0 (the electron rest mass), which is the most accurate value measured by cyclotron resonance for AlGaAs grown epitaxially in the (311) plane [36]. In the following tables and plots, CGS units are used, energies are in electron volts and layer widths are in Angstroms.

Table 3.1 Vary T (Case 1)

Fixed N_A, N_D, x, d_W,d_δ,d_X, β

d (Å)	800	800	800	800	800	800	800
d_W (Å)	100	100	100	100	100	100	100
d_X (Å)	240	240	240	240	240	240	240
d_δ (Å)	30	30	30	30	30	30	30
x	0.4	0.4	0.4	0.4	0.4	0.4	0.4
N_A	1.21E+19	1.21E+19	1.21E+19	1.21E+19	1.21E+19	1.21E+19	1.21E+19
N_D	1.21E+19	1.21E+19	1.21E+19	1.21E+19	1.21E+19	1.21E+19	1.21E+19
temp (K)	0.0	0.5	1.0	2.0	5.0	7.5	10.0
dy	0.15	0.15	0.15	0.15	0.15	0.15	0.15
iterations	25	15	17	16	18	15	14
R_S (Ohms)	5.27E+03	5.27E+03	5.26E+03	5.21E+03	4.91E+03	4.60E+03	3.86E+03
N_S	2.645E+10	2.6420E+10	2.6480E+10	2.6740E+10	2.8310E+10	3.0130E+10	3.5860E+10
P_S	2.621E+10	2.6410E+10	2.6490E+10	2.6900E+10	2.8380E+10	3.0100E+10	3.5600E+10
$\beta-n$	1.69	1.69	1.69	1.71	1.81	1.93	2.30
$\beta-p$	1.68	1.69	1.70	1.72	1.82	1.93	2.28
Tf-n (K)	10.97	10.96	10.98	11.09	11.74	12.49	14.87
Tf-p (K)	4.85	4.89	4.91	4.98	5.26	5.58	6.59
e-eigen (eV)	9.4331E-04	9.4224E-04	9.4438E-04	9.5365E-04	1.0096E-03	1.0746E-03	1.2789E-03
h-eigen (eV)	4.1752E-04	4.2071E-04	4.2198E-04	4.2851E-04	4.5209E-04	4.7949E-04	5.6710E-04
E_{MAX} Volts/cm	5.51E+05	5.51E+05	5.51E+05	5.51E+05	5.51E+05	5.51E+05	5.51E+05
E_C (eV)	1.43	1.43	1.43	1.43	1.43	1.43	1.43
E_V (eV)	0.0	0.0	0.0	0.0	0.0	0.0	0.0
p	2.621E+16	2.641E+16	2.649E+16	2.690E+16	2.838E+16	3.010E+16	3.560E+16
n	2.645E+16	2.642E+16	2.648E+16	2.674E+16	2.831E+16	3.013E+16	3.586E+16

The superlattice structure that is being simulated is very sensitive to the surface and substrate boundary conditions because it is nearly charge neutral with respect to the fixed charge. Another issue is that the ionization of dopants at very low temperatures (especially 0 K) is complicated. The x = 0.4 structure is more likely to have electrons and holes in the wells because the wells are deeper compared to the depth of the surrounding AlGaAs layers. This effect can be pronounced at 0 K because the Fermi function is very abrupt. If electrons form in the last well, holes form in the central wells to balance this negative charge. For x < 0.3, the wells are too shallow to get both positive and negative carrier distributions in alternating wells. By contrast in the x = 0.4 case, the wells are deep enough to get positive and negative carriers in alternating wells.

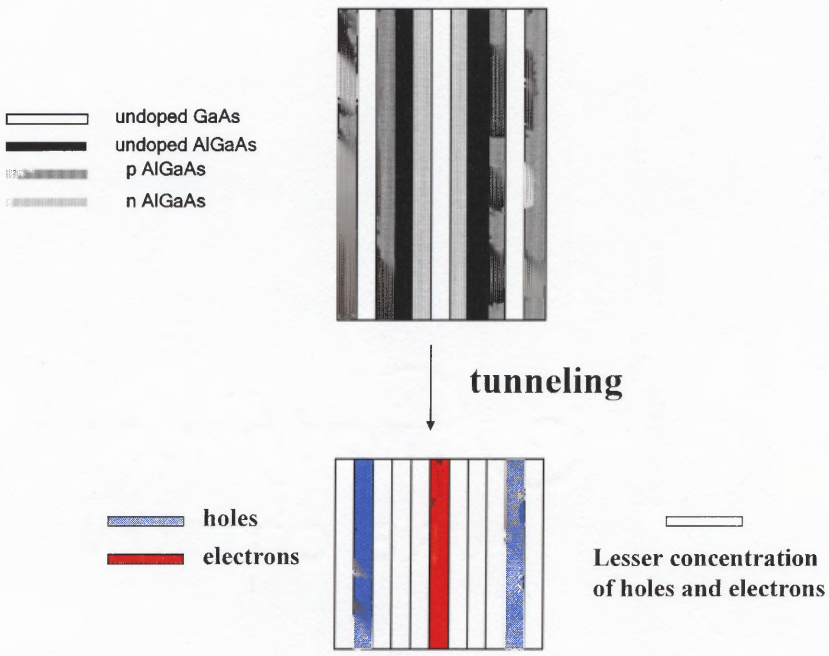

Figure 3.1 Semiconductor superlattice and carrier formation.

The Snider program has limitations, and has difficulty calculating dopant ionization at low temperatures. If one assumes a single ionization energy in the bandgap for dopants,

the carriers should freeze out at low temperatures. This alone causes numerical problems as the abrupt Fermi function leads to large changes in charge concentration as the Fermi level exceeds the ionization energy. A single dopant energy ignores the dopant energy bands caused by degenerate doping. Particularly at low temperatures, the program has a hard time converging if it does not have at least one fixed boundary condition. Schrödinger's and Poisson's Equations are solved self-consistently in a region, if one specifies the boundaries of the region, measured from the surface.

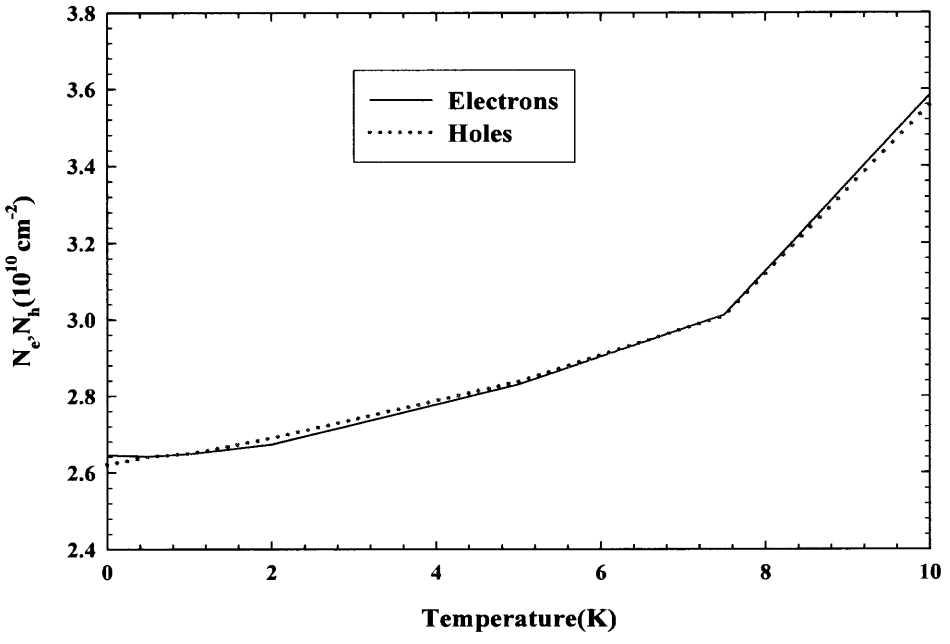

Figure 3.2 Temperature dependence of sheet electron and hole densities calculated for the modulation doped superlattice for alloy concentration of x = 0.4.

In Case 1 (Table 3.1), temperature changes had significant effect on the induced electric field. The sheet resistance decreased as the temperature rose but only incrementally. Ionization increased with increasing temperature. Both the surface charge densities and Fermi energies increased as expected with increased ionization. The sheet

resistance decreased because the sheet resistance is inversely proportional to surface density. As T increased from 0 to 10 K (Table 3.2), the sheet resistance decreased by 26.7%. The induced electric field remained constant and the ratio $p/N_A d_\delta$ increased by about 35.87%. The efficiency of charge transfer to the quantum wells, are calculated as $\eta_E = nd_W/N_D d_\delta$ for the electrons or $\eta_H = pd_W/N_A d_\delta$ for the holes, where d_W, d_δ are in Angstroms, and N_A and N_D are in units of 10^{19} atoms/cm^3. Changes in η with respect to changes in temperature can be expressed as $\Delta\eta_E = \alpha_E \Delta T$ and $\Delta\eta_H = \alpha_H \Delta T$ and their plots are shown in Figure 3.2 with $\alpha_H = \alpha_E = 0.0537\ K^{-1}$.

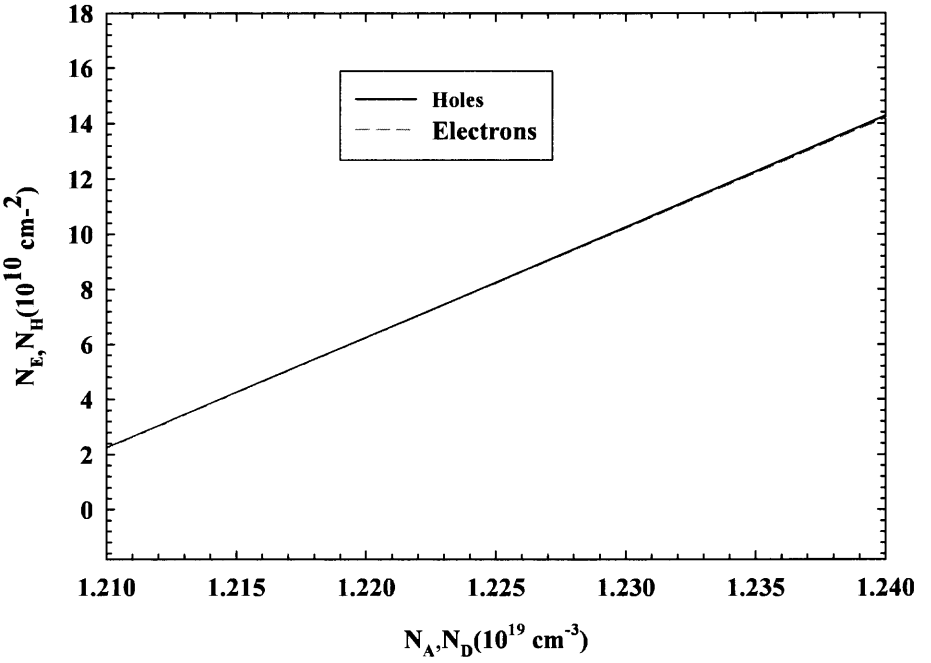

Figure 3.3 Variation of sheet electron and hole densities with concentration of dopants in modulation doped layers of a superlattice for alloy concentration of x = 0.4.

In Case 2 (Table 3.2), the layer widths were held constant as was x and T, while N_A, N_D and β were varied. Progressively increasing the doping concentration by

3.48% resulted in a large decrease in the sheet resistance and a large increase in β, charge surface densities and the Fermi energy - consistent with theory. As N_A and N_D increased from 1.205×10^{19} to 1.244×10^{19} atoms/cm^3 (Table 3.2), the sheet resistance decreased by 98.4%. The induced electric field increased by 1% and the ratio $p/N_A d_\delta$ increased by over 5,900%. The efficiency of charge transfer to the quantum wells are calculated as $\eta_E = nd_W/N_D d_\delta$ for the electrons or $\eta_H = pd_W/N_A d_\delta$ for the holes. Changes in η with respect to changes in doping can be expressed as $\Delta\eta_E = \beta_E \Delta N_D$ and $\Delta\eta_H = \beta_H \Delta N_A$ and their plots are shown in Figure 3.3 with $\beta_H = \beta_E = 960$ cm^3.

In Case 3 (Table 3.5), the width of the doped and spacer layers varied but β, the width of the well, and x were kept fixed with constant T = 0 K. Since β was held constant, the charge surface densities and the Fermi energy remained virtually unchanged as did the conduction and valence profiles (Figure 3.4). As d_δ increased from 1.0 to 5.5 nm, the sheet resistance decreased by 46.7%, the induced electric field increased by 23.4% (Figure 3.5), and the ratio $p/N_A d_\delta$ decreased by 20.2% (Table 3.3).

Conduction and valence band edges offsets (Figure 3.4) at $d_\delta = 5.0$ and 3.0 nm in the GaAs wells cross the Fermi level at -58.5 and 6.1 meV, respectively, with no change in the offsets as d_δ was varied (see Table 3.5). For Case 3, the change in the induced electric field increased by 23.4 % as d_δ was varied. In contrast, for Case 4, the change in the induced electric field decreased by 2.4 % as d_δ was varied (Table 3.3). The larger electric field increase in Case 3 was the result of the spacer being reduced in width as the width of the doped layers increased. Decreasing the width of the spacer layers increases the threshold of the induced field causing fewer carriers to be transferred into the GaAs

wells. The result is an induced electric field having a higher concentration outside the GaAs wells. The conduction and valence band edges in the GaAs wells remain constant for incremental increases in d_δ. Figure 3.5 shows the built-in electric field E(y) as a function of depth coordinate y for the same simulation results that

Table 3.2 Vary Doping Concentration, Beta (Case 2)

Fixed x, d_W,d_δ,d_X , T

d (Å)	800	800	800	800	800	800
d_W (Å)	100	100	100	100	100	100
d_X (Å)	240	240	240	240	240	240
d_δ (Å)	30	30	30	30	30	30
x	0.4	0.4	0.4	0.4	0.4	0.4
N_A	1.205E+19	1.2070E+19	1.2090E+19	1.2170E+19	1.2250E+19	1.2440E+19
N_D	1.205E+19	1.2070E+19	1.2090E+19	1.2170E+19	1.2250E+19	1.2440E+19
temp (K)	0.0	0.0	0.0	0.0	0.0	0.0
dy	1	1	1	1	1	1
iterations	20	20	20	17	17	17
R_S (Ohms)	5.81E+04	1.34E+04	7.55E+03	2.76E+03	1.69E+03	8.77E+02
N_S	2.383E+09	1.0390E+10	1.8430E+10	5.0500E+10	8.2530E+10	1.5870E+11
P_S	2.498E+09	1.0430E+10	1.8270E+10	5.0080E+10	8.2040E+10	1.5780E+11
$\beta-n$	0.15	0.66	1.18	3.23	5.28	10.16
$\beta-p$	0.16	0.67	1.17	3.21	5.25	10.10
Tf-n (K)	0.99	4.31	7.64	20.94	34.22	65.81
Tf-p (K)	0.46	1.93	3.38	9.28	15.20	29.23
e-eigen (eV)	8.4987E-05	3.7055E-04	6.5729E-04	1.8010E-03	2.9433E-03	5.6599E-03
h-eigen (eV)	3.9793E-05	1.6615E-04	2.9104E-04	7.9777E-04	1.3069E-03	2.5137E-03
E_{MAX} Volts/cm	5.50E+05	5.50E+05	5.51E+05	5.51E+05	5.53E+05	5.56E+05
E_C (eV)	1.43	1.43	1.43	1.43	1.43	1.43
E_V (eV)	0.0	0.0	0.0	0.0	0.0	0.0
p	2.498E+15	1.043E+16	1.827E+16	5.008E+16	8.204E+16	1.578E+17
n	2.383E+15	1.039E+16	1.843E+16	5.050E+16	8.253E+16	1.587E+17

produced Figure 3.4. The magnitude of the field is maximum and nearly constant in the spacer layers. The electric field in the GaAs wells increases by 22.8 mV/cm per nm incremental increase in d_δ.

Table 3.3 Effect of D-Delta on Sheet Resistance, Maximum Electric Field and Charge Transfer Efficiency

	R_S	E_{MAX}	$p/N_A d_\delta$
Case 3	46.7% ↓	23.4% ↑	20.2% ↓
Case 4	51.7% ↓	2.4% ↓	200% ↑

In Case 4 (Table 3.6), the width of the doped and well layers were varied while the spacer was held constant at 240 Angstroms. The charge surface densities, β and the Fermi energy remained virtually unchanged. As the width of the well increased, d_δ had to be decreased in order to maintain a constant d. Since d_X remained constant, the threshold field within the spacers also remained constant. As d_δ increased from 10 to 55 Angstroms, the sheet resistance decreased by 51.7%, the induced electric

Table 3.4 Effect of D-Delta on Energy Band Offsets

	$\Delta E_{C\_OFF}/\Delta d_\delta$	$\Delta E_{V\_OFF}/\Delta d_\delta$
Case 3	0 %	0 %
Case 4	7.0 % ↑	0 %

field decreased by 2.4%, and the ratio $p / N_A d_\delta$ increased by over 200% (see Table 3.3).

Table 3.5 Vary D-Delta, D-Spacer (Case 3)

Fixed β, x, d_W, T

d (Å)	800	800	800	800	800	800
d_δ (Å)	55	50	40	30	10	5
d_W (Å)	100	100	100	100	100	100
d_X (Å)	190	200	220	240	280	290
N_A	7.28E+18	7.85E+18	9.43E+18	1.21E+19	3.25E+19	6.65E+19
N_D	7.28E+18	7.85E+18	9.43E+18	1.21E+19	3.25E+19	6.65E+19
x	7.28E+18	7.85E+18	9.43E+18	1.21E+19	3.25E+19	6.65E+19
temp (K)	0.0	0.0	0.0	0.0	0.0	0.0
dy	1	1	1	1	1	1
iterations	27	23	25	64	200	21
R_S (Ohms)	1.1310E+03	2.1580E+03	2.1590E+03	3.8650E+03	2.1220E+03	6.4660E+03
N_S	2.6780E+10	2.6630E+10	2.7030E+10	2.641E+10	2.720E+10	2.722E+10
P_S	2.6670E+10	2.6520E+10	2.6920E+10	2.631E+10	2.713E+10	2.709E+10
$\beta-n$	1.71	1.70	1.73	1.69	1.74	1.74
$\beta-p$	1.71	1.70	1.72	1.68	1.74	1.73
Tf-n (K)	11.11	11.04	11.21	10.95	11.28	11.29
Tf-p (K)	4.94	4.91	4.99	4.87	5.03	5.02
e-eigen (eV)	9.5508E-04	9.4973E-04	9.6400E-04	9.4189E-04	9.7006E-04	9.7077E-04
h-eigen (eV)	4.2485E-04	4.2246E-04	4.2883E-04	4.1912E-04	4.3218E-04	4.3154E-04
E_{MAX} Volts/cm	6.07E+05	5.95E+05	5.72E+05	5.50E+05	4.92E+05	5.04E+05
E_C (eV)	1.43	1.43	1.43	1.43	1.43	1.43
E_V (eV)	0.0	0.0	0.0	0.0	0.0	0.0
p	2.667E+16	2.652E+16	2.692E+16	2.631E+16	2.713E+16	2.709E+16
n	2.678E+16	2.663E+16	2.703E+16	2.641E+16	2.720E+16	2.722E+16

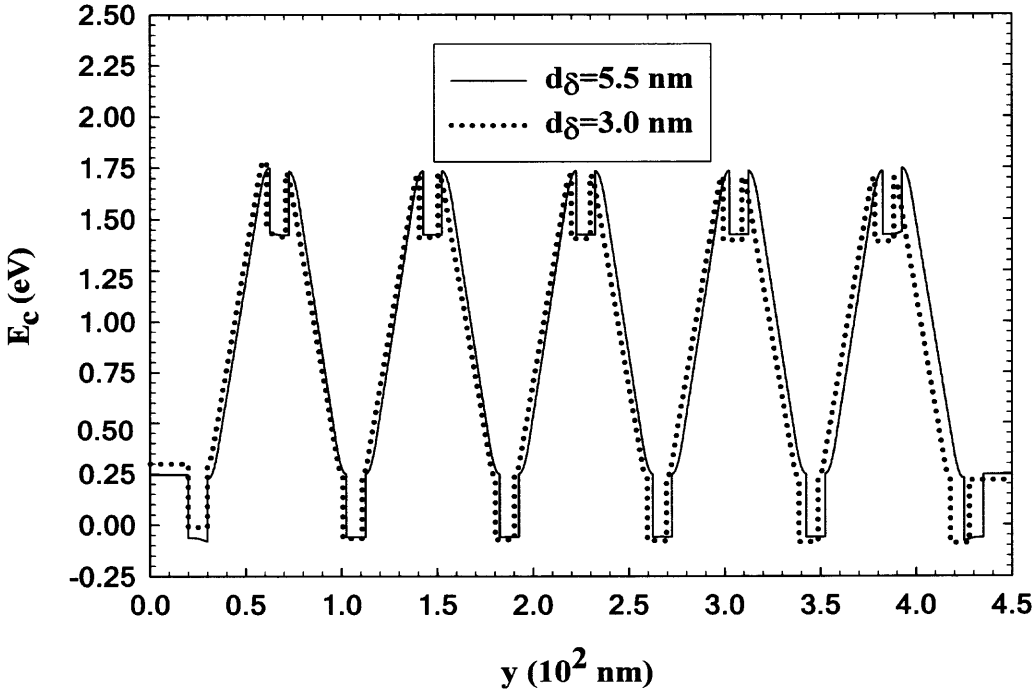

(a)

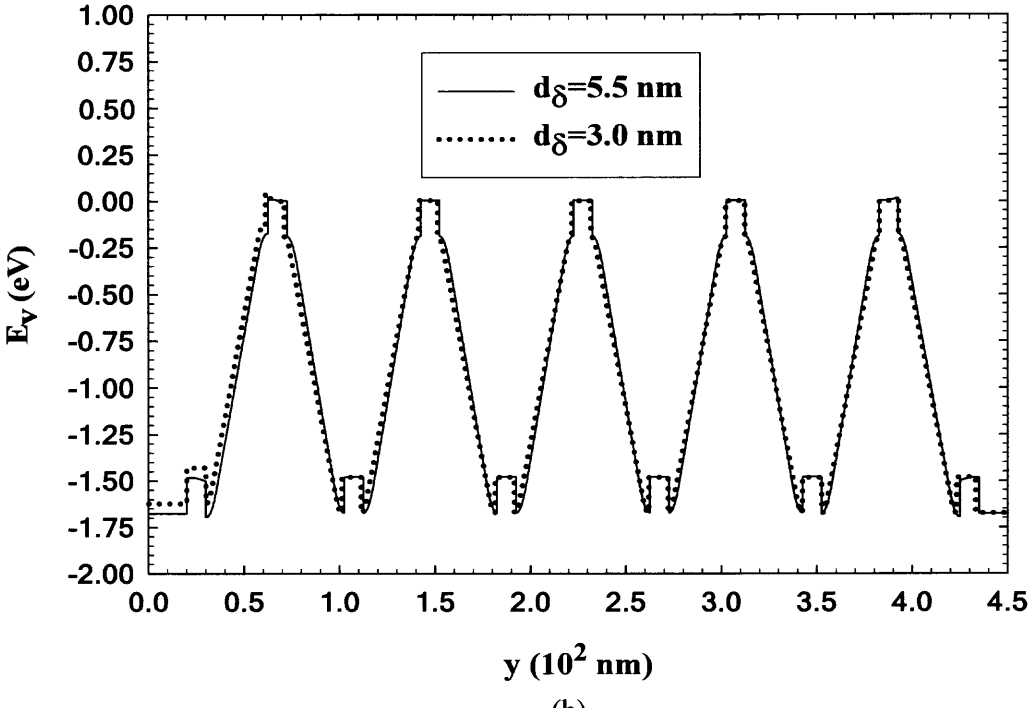

(b)

Figure 3.4 (a) Edges of conduction band, (b) Edges of valence band. For modulation doped n-p-n superlattice of alloy composition x = 0.4 as functions of depth y (Case 3).

Conduction and valence band edges offsets (Figure 3.6) at d_δ = 5.0 and 3.0 nm in the GaAs wells cross the Fermi level at -234, -59, and 6.6, 6.6 meV, respectively, with only the conduction band offset increased as d_δ was varied. The conduction band edge in the GaAs wells increases by 87.5 meV per nm incremental increase in d_δ. The valence band edge in the GaAs wells remained constant as d_δ varied. Figure 3.7 shows the built-in electric field E(y) as a function of depth coordinate y for the same simulation that resulted in Figure 3.5. The magnitude of the field is maximum and nearly constant in the spacer layers owing to the unchanged threshold field. The electric field in the well in the GaAs wells increases by 6.6 mV/cm per nm incremental increase in d_δ.

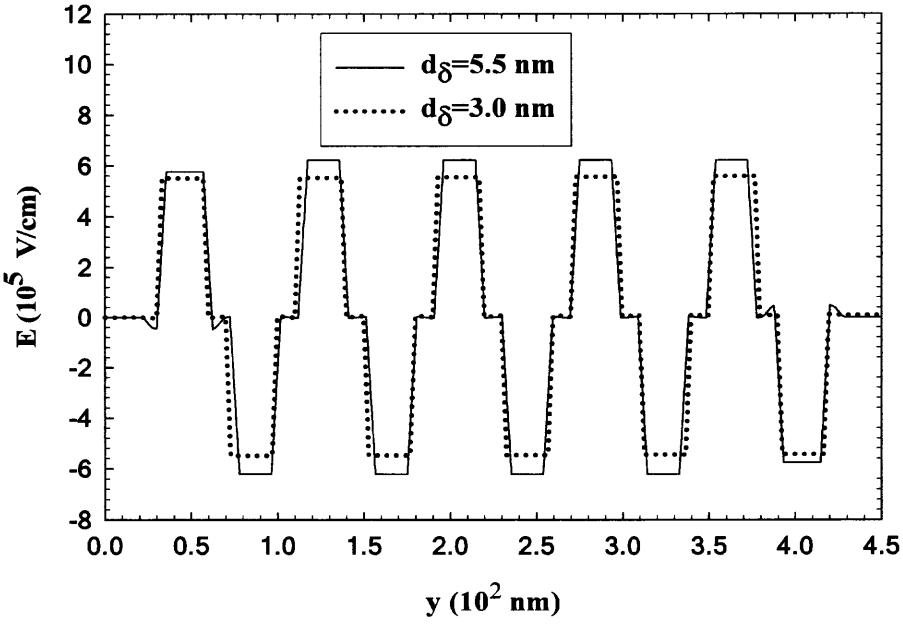

Figure 3.5 Variation with depth y of the built-in electric field of a modulation doped n-p-n superlattice of alloy composition x = 0.4 (Case 3).

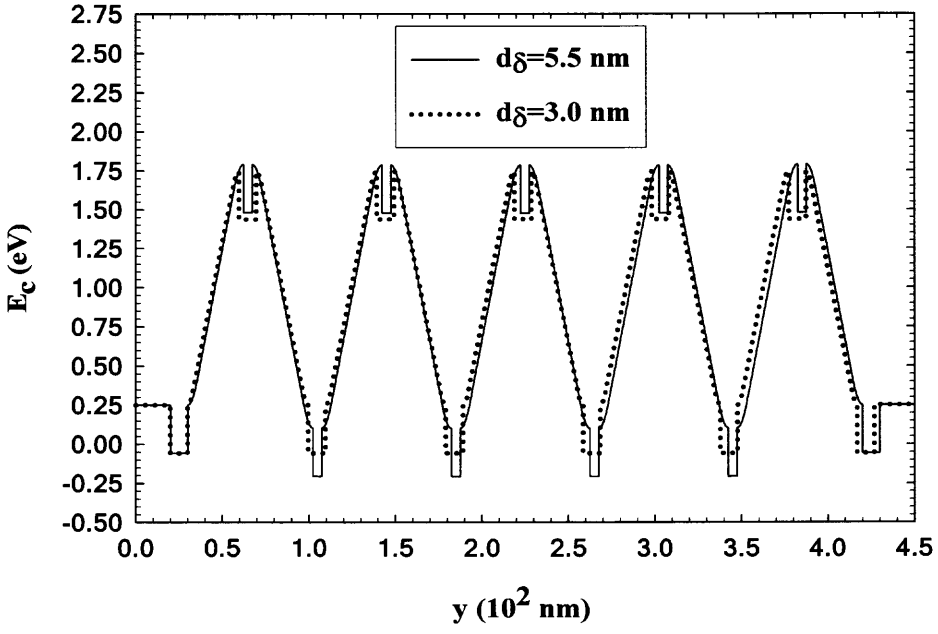

(a)

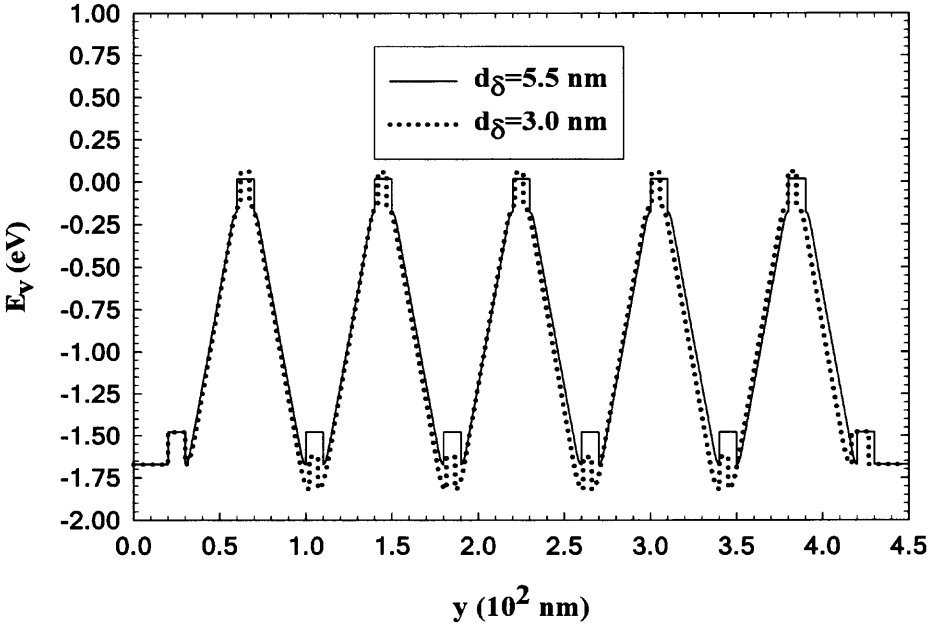

(b)

Figure 3.6 (a) Edges of conduction band, (b) Edges of valence band. For modulation doped n-p-n superlattice of alloy composition x = 0.4 as functions of depth y (Case 4).

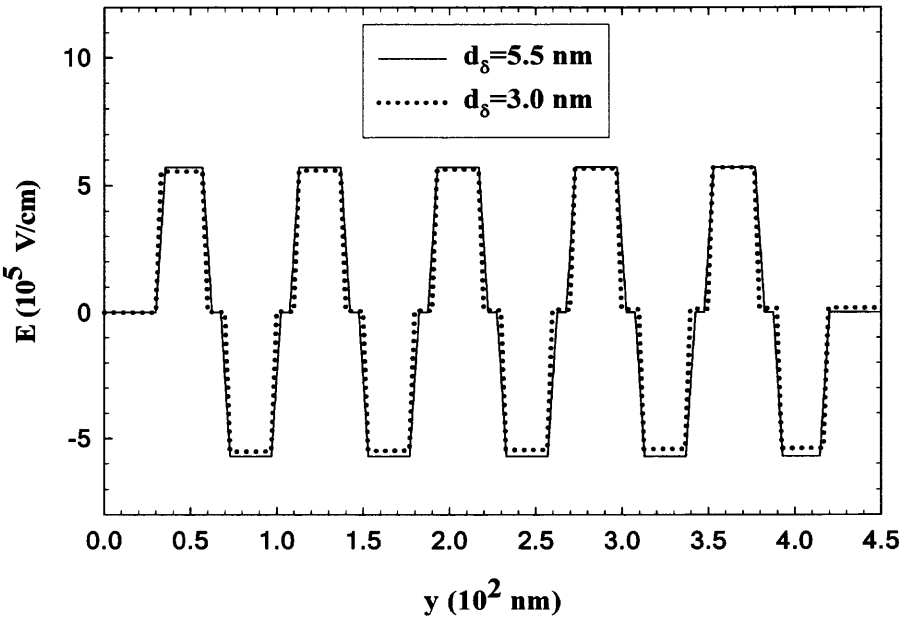

Figure 3.7 Variation with depth y of the built-in electric field of a modulation doped n-p-n superlattice of alloy composition x = 0.4 (Case 4).

The logical self consistency of Cases 3 and 4 are evident in the plots in Figures 3.8 and 3.9. In Figure 3.8, for both cases, $N_A d_\delta$ is plotted against d_S (the respective β's are held constant). For Case 3, as d_δ increases, d_X decreases in order to keep d constant. As d_X decreases, P_S and N_S remains unchanged as β is held constant ($\beta = 1.71$). Since the spacer width is decreasing, the threshold electric field increases so fewer electrons or holes are spilling into the GaAs wells. In order to keep β constant, $N_A d_\delta$ must increase. Thus, $p/d_\delta N_A$ deceases as d_δ increases.

For Case 4, as d_δ increases, d_X remains constant so the number of holes spilling over into the GaAs wells also remains constant but the width of the GaAs wells decreases. As d_δ increases in Case 4, the sheet density P_S remains the same since β is held constant ($\beta = 2.4$). Since d_W is decreasing, p must increase in order to keep P_S

constant and $N_A d_\delta$ decreases. Thus, efficiency of charge transfer $p/N_A d_\delta$ increases. This is consistent with the plot in Figure 3.9 where $p/N_A d_\delta$ increases as d_δ increases.

Table 3.6 Vary D-Delta, D-Well (Case 4)

Fixed β, d_X, x, T

d (Å)	800	800	800	800	800
d_W (Å)	50	60	80	100	140
d_X (Å)	240	240	240	240	240
d_δ (Å)	55	50	40	30	10
x	0.4	0.4	0.4	0.4	0.4
N_A	6.825E+18	7.290E+18	8.986E+18	1.213E+19	3.849E+19
N_D	6.825E+18	7.290E+18	8.986E+18	1.213E+19	3.849E+19
temp (K)	0.0	0.0	0.0	0.0	0.0
dy	1	1	1	1	1
iterations	107	21	37	19	24
R_S (Ohms)	2.369E+03	4.422E+03	4.875E+03	3.860E+03	4.884E+03
N_S	3.618E+10	3.568E+10	3.607E+10	3.607E+10	3.612E+10
P_S	3.797E+10	3.547E+10	3.572E+10	3.576E+10	3.596E+10
$\beta-n$	2.32	2.28	2.31	2.31	2.31
$\beta-p$	2.43	2.27	2.29	2.29	2.30
Tf-n (K)	15.00	14.80	14.96	14.96	14.98
Tf-p (K)	7.03	6.57	6.62	6.62	6.66
e-eigen (eV)	1.290E-03	1.272E-03	1.286E-03	1.286E-03	1.288E-03
h-eigen (eV)	6.049E-04	5.650E-04	5.690E-04	5.697E-04	5.728E-04
E_{MAX} Volts/cm	5.680E+05	5.520E+05	5.400E+05	5.510E+05	5.820E+05
E_C (eV)	1.43	1.43	1.43	1.43	1.43
E_V (eV)	0.0	0.0	0.0	0.0	0.0
p	7.594E+16	5.912E+16	4.465E+16	3.576E+16	2.569E+16
n	7.236E+16	5.947E+16	4.509E+16	3.607E+16	2.580E+16

This section has underlined the possibility of forming superconducting electron-hole superlattices in modulation-doped GaAs/$Al_xGa_{1-x}As$ heterostructures by a self-consistent numerical solution of the Schrödinger and Poisson Equations. These superlattices emulate the electronic structure of high$-T_C$ superconductors for $\beta = Nd^2 = 1$, where N is the sheet carrier density in the layers and d is the superlattice period. Results are based on a maximum built-in electrostatic field of 500 $kVcm^{-1}$, which dictates a minimum superlattice period of d = 80 nm. The corresponding sheet carrier density of electrons and holes is $N = 1.56 \times 10^{10}$ cm^{-2} which is five times larger than the minimum sheet density required for metallic superconductivity Based on a strong-coupling electronic model of superconductivity, a superconductor with a transition temperature of 2 K will result from such an electron-hole superlattice [37].

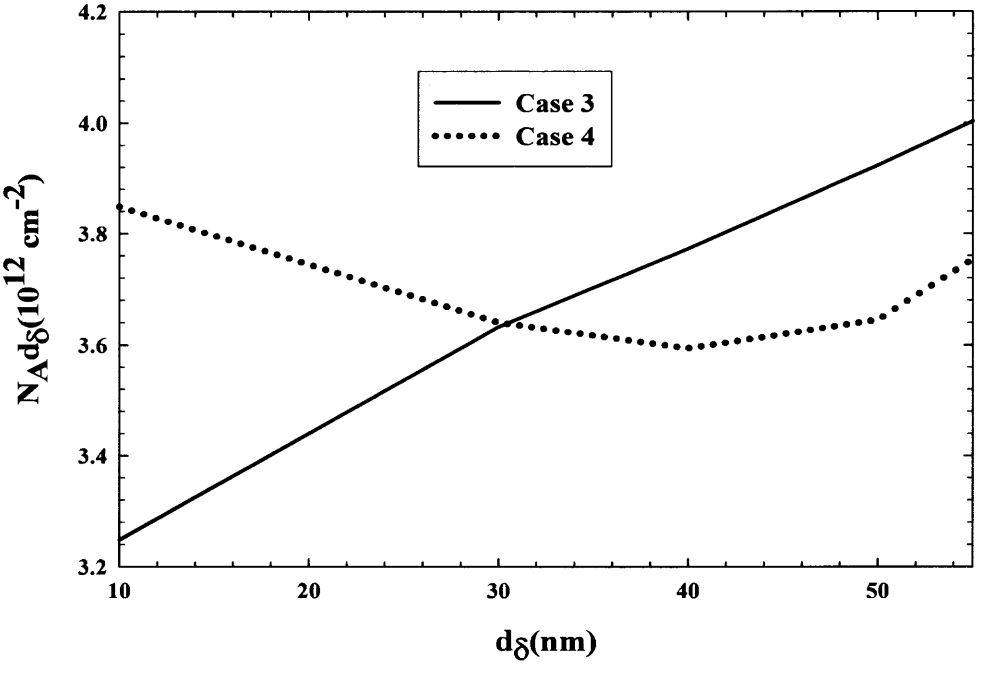

Figure 3.8 Plots of acceptor sheet density vs. d-delta.

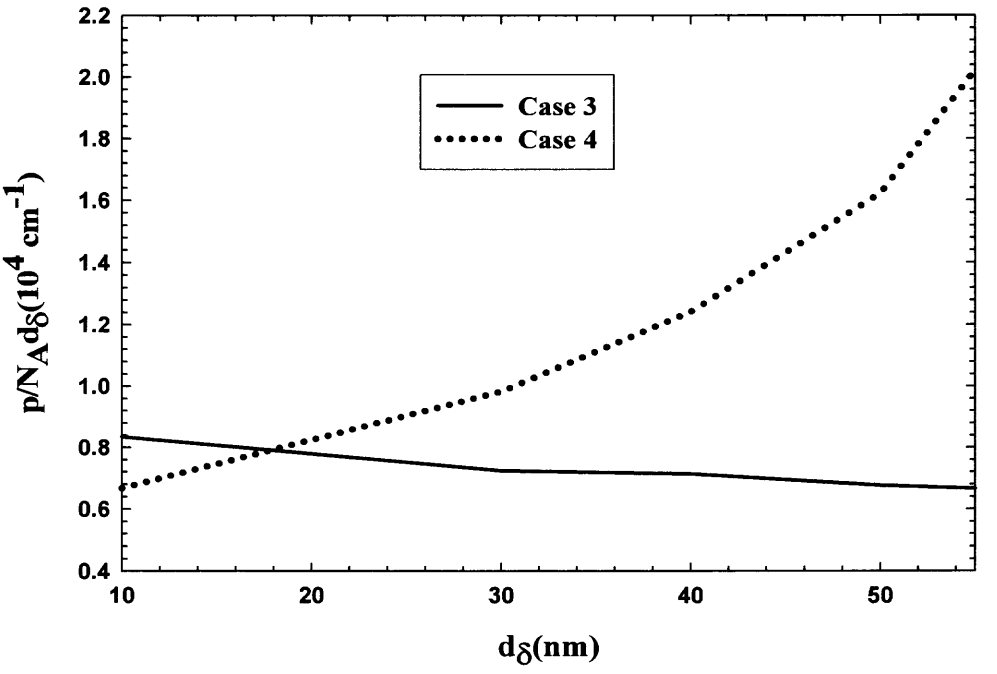

Figure 3.9 Plots of charge transfer efficiency vs. d-delta.

3.2 The Effect of Donor Concentrations and Layer Thickness on the Beta vs. T Plot

Hundreds of computer simulations, using the Snider program, were performed to determine the effects of layer thickness and donor concentration on β. The basic structure of the uniform superlattice is shown in Figure 3.1. The thickness of the layers is denoted by L. In order for the carriers to be bound in the wells, quantum confinement must be assured by having the conduction levels in the layers adjacent to the wells at a higher level. This can be done by increasing the alloy concentration of AlGaAs as shown in Figure 3.10.

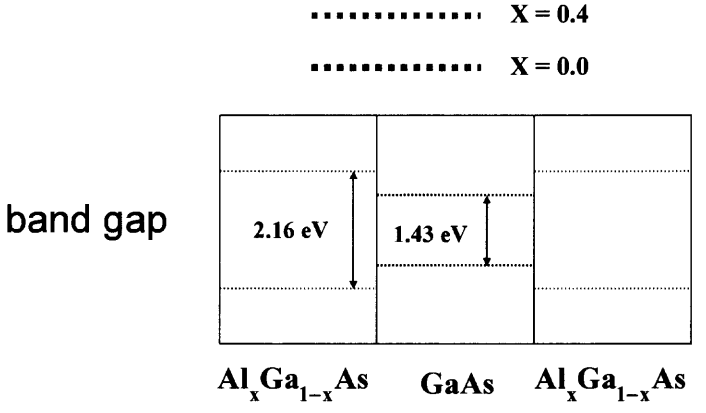

Figure 3.10 Quantum confinement in GaAs wells.

During tunneling, charges are transferred from n-doped layers to p-doped layers. At equilibrium, the carriers are distributed in the GaAs wells with lesser concentrations elsewhere as indicated in the figure above. The thickness of the capping layers is taken to be sufficiently large such that the amplitudes of the bound-state wavefunctions at the surface and substrate are negligibly small, which is possible because the proposed symmetric device structure has zero bias and zero net charge. Capping layers of $d_C = 10$ nm are found to be of sufficient thickness to allow one to impose zero wavefunction slope as the boundary condition. The results of the first set of simulations confirmed the

underlying theory in Section 2.3 and are summarized in Table 3.7 with the corresponding plots in Figures 3.11 and 3.12. In Table 3.7, N is of the order of 10^{19} atoms$-$cm^{-3} and T_C is in Kelvin.

Table 3.7 Effect of Donor/Acceptor Concentration N and Layer Thickness L on Beta

T(K)/β	L= 50 Å N=0.01	L= 50 Å N=0.02	L = 50 Å N=0.03	L = 100 Å N=0.01	L = 125 Å N=0.01
1	0.004	0.0027	0.0	0.0	0.0
10	0.05	0.06	0.006	0.07	0.08
50	0.14	0.2	0.2	0.14	0.44
300	0.22	0.39	0.38	0.85	1.45

The curves for L = 50 Å, L = 100 Å, and L = 125 Å show a progressive increase in both the slope and relative amplitude of the β vs. T plots which are influenced by four factors. Firstly, increasing L will automatically increase β since d is also increased, if the carrier sheet density remains fixed.. Secondly, increasing L will decrease the wave number k since it is inversely proportional to L. As k decreases, the difference of the energy levels of the AlGaAs and GaAs wells decreases so more electrons are tunneling out of the GaAs well. Thirdly, increased layer widths also increase the amount of interplanar charge transfer. Fourthly, the exponential nature of the electron/hole formation. One of the independent variables of the hole density function is the difference of the inverses of the effective masses of electrons within and outside the GaAs wells. As k decreases, more electrons tunnel. The resultant formation of positive and negative ions can push or pull electrons in their respective wells, thus affecting the electron's effective mass since electrons have to drag the ionic cores around with them or

be pulled along by them. From Equations 2.9 and 2.10, even if $1/m_{AlGaAs} - 1/m_{GaAs}$ increases by a small amount, the free hole and electron densities and the slope of the β vs. T plot can increase significantly.

The creation of carrier densities is also influenced by donor concentrations. The rate at which electrons go from one well to another is dependent on the availability of hole states in one well and the availability of electron states in the other. Increased donor concentrations and layer thickness affect the carrier sheet densities and hence the β vs. T slope in Figures 3.11 and 3.12.

The mechanism of populating the quantum wells with electron and hole carriers from adjacent doping layers is one of balancing Fermi energies and interplanar Coulomb interaction. The interplanar Coulomb interaction, $V = e^2/(\varepsilon d')$ (d' is the near-neighbor distance in the x, y, or z direction), must have a proper magnitude relative to the 2D Fermi energy. If V is too large, maintaining a separation of the interplanar layers would be difficult since they would behave as if they belonged to a single plane. If V is too small, the coupling of the alternating planes will be too weak to yield bound states. If one wants to achieve a greater critical temperature by decreasing the layer thickness L from 100 to 10 Angstroms in order to maintain the same electric field, one would have to increase the donor concentration by a factor of 10, assuming complete ionization of the donor atoms.

Since one is dealing with low-dimensional superlattice structures, the sheet density of a layer and the areal density would be numerically equal. The sheet densities do not change since $P_S \approx pL$. For L = 10 Angstroms, p is 10 times greater than it was when L = 100 Angstroms, but L decreases by a factor of 1/10 so P_S remains constant.

Now β decreases by a factor of $(80/800)^2 = 0.01$, which partially explains the large decrease in the slope of β vs. T when L = 50 Angstroms was used.

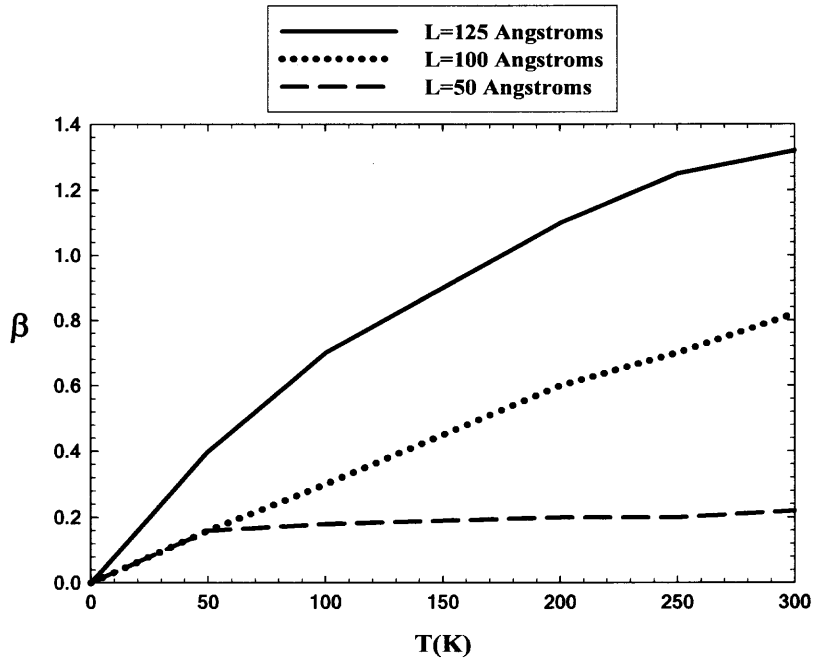

Figure 3.11 Effect of layer thickness on beta.

To guide in the design of a better superlattice, the Table below can be used as a "rule of thumb" and also in understanding the "see-saw" relationship between n and p. In a semiconductor, Poisson's Equations can be expressed as $\partial E/\partial x = (p - n + N_D^+ - N_A^-)/\varepsilon_0$. In the absence of an external electric field where the material is only p-doped $n = p + N_D^+ - N_A^-$. In low-dimensional semiconductors, tunneling induces spatially varying electric field and the gradient so the left side of the above equation is not zero.

Charge transfer from the n-doped and p-doped AlGaAs and undoped GaAs wells are very different, complex and occur in both the +z and – z directions and are exponentially dependent on the width of barriers. Electrons from the GaAs wells can

tunnel more easily into the adjacent p-doped AlGaAs wells than can electrons from ionized n-doped AlGaAs tunnel inward into the GaAs wells. Electrons from the n-doped AlGaAs flow inward into the GaAs wells but the accumulated electrons in the well can act as a "screen" to prevent further electron accumulation. Electrons from the n-doped AlGaAs tunneling away from the GaAs wells are attracted by p-doped AlGaAs layers which further retard the accumulation of electrons in the GaAs wells. Electrons

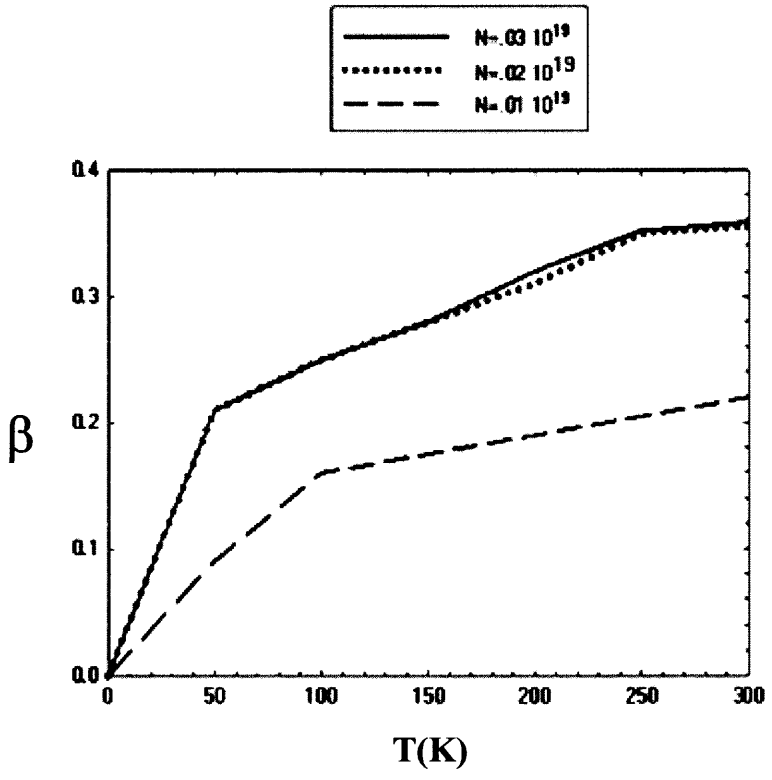

Figure 3.12 Effect of donor concentration on beta, L = 50 Angstroms.

Table 3.8 Relationships Between the Electric Field and the Sheet Resistance as the Layer Thickness and Doping Concentrations are Varied

L	N	E	R_S
↑	↑	↑	↓
↓	↓	↓	↑

tunneling away from the GaAs wells, surrounded by p-doped AlGaAs layers, are not immediately repelled by negative charge distributions.

Holes from the p-doped AlGaAs layers flow inward into the GaAs wells but accumulated holes in the well can act as a "screen" to prevent further hole accumulation. Holes tunneling away from the GaAs wells, surrounded by n-doped AlGaAs layers, are not immediately repelled by positive charge distributions. Holes from the p-doped AlGaAs tunneling away from the GaAs wells are attracted by n-doped AlGaAs layers which further retard the accumulation of holes in the GaAs wells.

3.3 Superlattices With Uniform Spacing

Case 1:

$d_X = d_W = d_\delta = 10$ Å, $d_S = d_C = 100$ Å, $d = 80$ Å

$N_{Ai} = 2\text{x}10^{19}$ for i = 2,4,34,36

$N_{Ai} = 1.8\text{x}10^{19}$ for i = 10,12,18,20,26,28

$N_{Di} = 0.5\text{x}10^{19}$ for i = 6,8,14,16,22,24,30,32

Computer simulations were performed using the design in Figure 3.1 and the β vs. T plot is shown in Figure 3.13. The results did not satisfy all the conditions of the Harshman formulation. Sheet resistance was about 1000 Ohms. Throughout the 95 % + of the superlattice, the maximum electric field of 10^5 V/cm was not exceeded. Simulations were performed with T = 5 K and T = 10 K, using S-P solvers. For T = 50 K, S-P solvers were not used because of convergence problems. There were unequal hole and electron surface densities but charge neutrality was achieved. $T_\beta = 35.0$ K was determined by interpolation since some simulations between 10 K and 50 K did not converge.

Bound states occur when the carriers are confined to their respective layers. Since the momentum of the carriers are well defined, the uncertainty in their position means that the carriers could be found anywhere in the superlattice. The wave functions for a specific output in the computer program are merely cartoon snapshots of the wavefunctions for the carriers within the superlattice at a particular time corresponding to the average geometric arrangement of carriers in the superlattice.

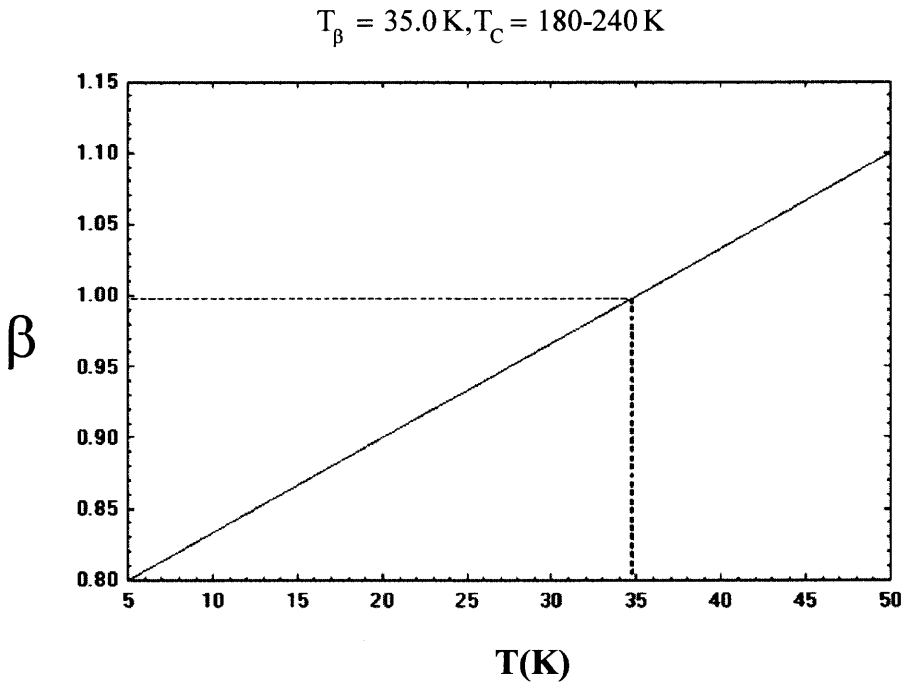

Figure 3.13 Beta vs. T plot (Case 1).

Case 2:

$d_X = d_W = d_\delta = 10$ Å, $d_S = d_C = 100$ Å, $d = 80$ Å

$N_{Ai} = 1x10^{19}$ for i = 2,4,34,36

$N_{Ai} = 1.8x10^{19}$ for i = 10,12,18,20,26,28

$N_{Di} = 0.2x10^{19}$ for i = 6,8,14,16,22,24,30,32

Case 2 was similar to Case 1 except the doping concentration was reduced within the superlattice. The graph in Figure 3.14 shows that the temperature is 3.7 K when β is equal to one, which is well below the critical temperature T_C = 180-240 K. Lowering the doping concentration within the lattice reduced T_β by over 31 degrees K. There were unequal hole and electron surface densities but charge neutrality was achieved. The induced field never exceeded the maximum tolerance level. In order to promote T_β, the slope of β vs. T would have to be decreased.

$T_\beta = 3.7\ K, T_C = 180 - 240\ K$

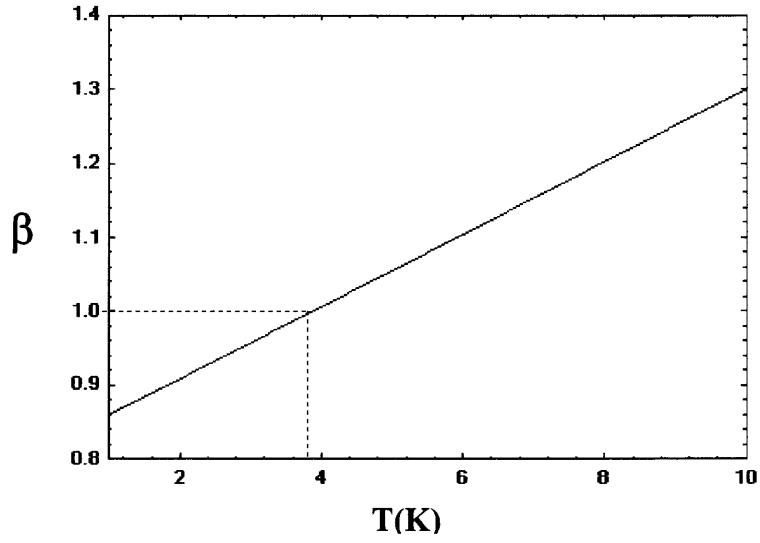

Figure 3.14 Beta vs. T plot (Case 2)

Case 3:

d = 200-100 $\overset{0}{A}$, uniform layer thickness

Vary doping concentration

The third case had six subcases with varying layer widths and varying doping concentration. The effects of the varying layer widths and varying doping concentrations on the β profile are shown in Table 3.9. N is of the order of 10^{19} $atoms - cm^{-3}$ and T_C is in Kelvin. None of the six subcases yielded equal hole and electron layers and the criteria $T_\beta = T_C$ were never satisfied. Calculating T_C with a strong coupling of $\Lambda \approx 2-3$, yielded a high range of T_C of 28.8-38.4 K for L = 25 Angstroms to a lower range of 7.2-9.6 K for L = 125 Angstroms. The exponential nature of charge density in the wells as a function of layer thickness and doping concentration is evident from the table below. Keeping the doping concentration constant and varying the layer thickness L from 25-100 Angstroms increased β by an two

orders of magnitude – indicating a possible threshold in the evolution of sheet carrier densities. An increase of β by almost two orders of magnitude was also evident when L was kept constant at 50 Angstroms and the doping concentration was varied from 0.44723-2.0 $x10^{19}$ $atoms-cm^{-3}$.

Table 3.9 Effect of Donor and Acceptor Concentration N and Layer Width on Beta (Case 3)

T(K)/β	N=0.44723 L= 25 Å	N=0.44723 L= 50 Å	N=0.44723 L = 100 Å	N=0.44723 L = 125 Å	N=0.89446 L = 50 Å	N=2.02 L = 50 Å
1	0	0	1.009	137	0	42
5	.07	0	1.165	143	0	42
10	.22	.008	1.452	143	.015	42
15	.38	.04	1.771	143	.08	42
20	.51	.17	2.103	143	.2	42
50	1.37	.73	4.13	143	.73	43
100	2.53	1.58	7.75	144	1.6	46
300	5.33	4.44	24.08	147	4.7	63

Case 4:

$d_X = d_W = d_\delta = 10$ Å, $d_S = d_C = 100$ Å, $d = 80$ Å

$N_{Ai} = 0.48 \times 10^{19}$ for i = 2,4, 10, 12,18,20,26,28,34,36

$N_{Di} = 0.48 \times 10^{19}$ for i = 6,8,14,16,22,24,30,32

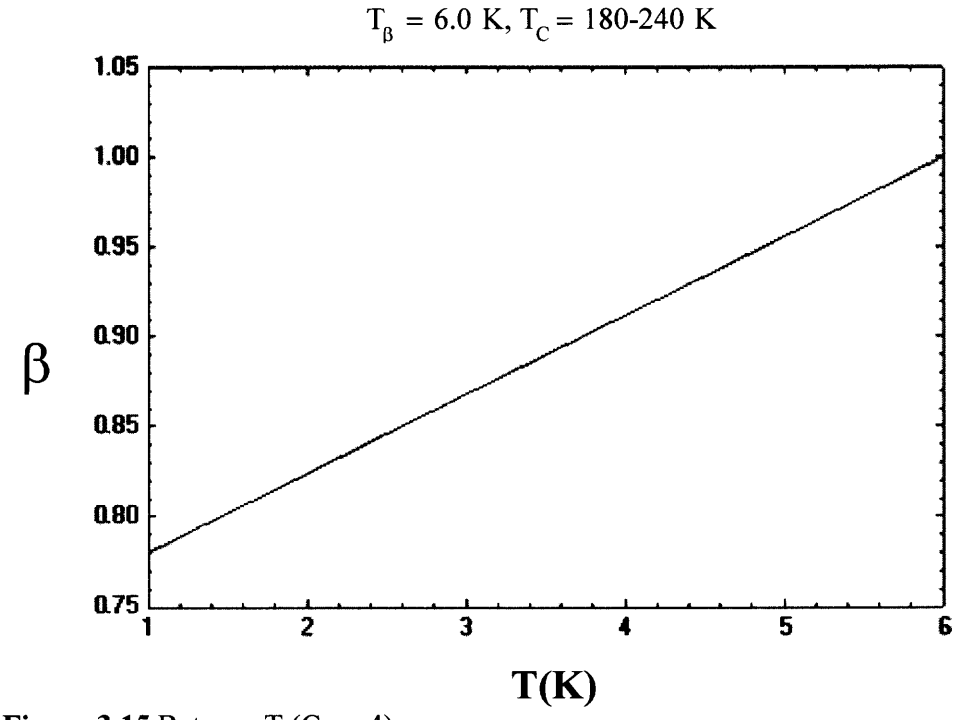

Figure 3.15 Beta vs. T (Case 4).

For Case 4, a temperature of 6 K (Figure 3.15) was achieved for equal alternating hole and electron layers of equal sheet densities with $\beta = 1$. The sheet resistance was below the maximum tolerance but the induced electric field exceeded the maximum tolerance by 33%. The maximal critical temperature for the design is 180-240 K, which is well above 6 K. The value of d for Case 4 was the same as for Case 2 (d = 400 Angstroms) but the temperature for β equal to 1.0 was about an order of a magnitude lower. The doping concentration was also much less in Case 4 than they were in Case 2. Satisfying one of the requirements of the Harshman formulation, i.e., equal and

alternating carrier layers, resulted in the lowering of T_β to a few degrees above absolute zero, an order of magnitude less than in the previous case.

The problem of maintaining equal carrier layers is due to the interplanar Coulomb interaction. If V is too large, maintaining a separation of the interplanar layers would be difficult since they would behave as if they belonged to a single plane. If V is too small, the coupling of the alternating planes will be too weak to yield bound states. Materials with large dielectric constants can tolerate larger internal fields before breaking down and would also increase the interplanar breakdown voltage. Choosing a semiconductor material that has a larger dielectric constant than AlGaAs and GaAs could at least theoretically increase the critical temperature.

3.4 Superlattices with Non-Uniform Spacing and Delta Doping

Case 5:

$d_X = d_S = d_C = 400$ Å, $d_W = 50$ Å, $d = 940$ Å

$N_{Ai} = 2.43 \times 10^{19}$ for i = 2,4, 10, 12,18,20,26,28,34,36

$N_{Di} = 2.43 \times 10^{19}$ for i = 6,8,14,16,22,24,30,3

Most of the criteria of the Harshman Model were satisfied but the critical temperature for this case, T_C, is below 1.88 K (Figure 3.16). The temperature corresponding to β equal to 1.0 was about 11 K. Alternating hole and electron layers of near equal surface densities existed. The induced electric field and sheet resistance never exceeded the maximum tolerance level. However, the T_C was not in the HTS range and the Harshman criteria for superconductivity were not completely satisfied since $T_C < T_\beta$.

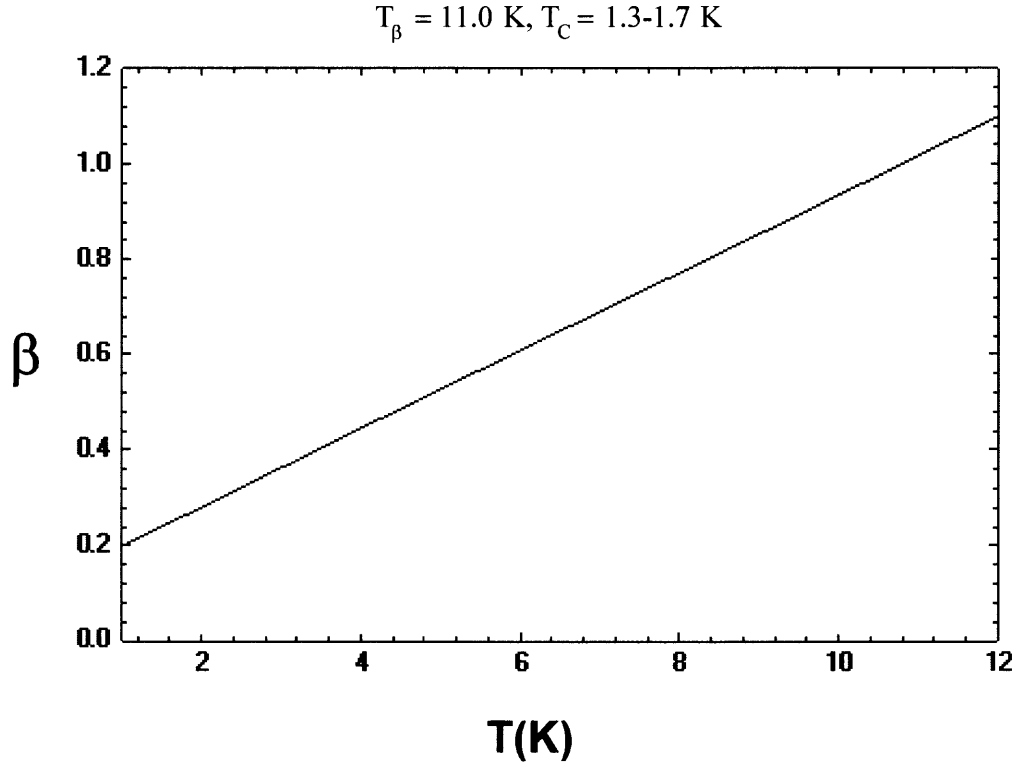

Figure 3.16 Beta vs. T plot (Case 5).

CHAPTER 4

RECENT DEVELOPMENTS IN HIGH TEMPERATURE SUPERCONDUCTIVITY

4.1 Experimental and Theoretical Developments

The existence of new superconductors has proven impossible to predict from first principles and their discovery has been largely empirical and intuitive. New systems can be found in either bulk methods or thin film materials and the search for new materials has always been, and remains, an important area of research in the field of superconductivity. Evidence exists that superconductivity is a bulk property [38].

At the Physics Department at Heriot-Watt in Edinburgh Scotland, researchers are presently working on a microscopic theory of high-temperature superconductivity that incorporates the findings of angle-resolved photo-emission spectroscopy in the cuprates. The key feature of the approach is the anisotropy in the screened Coulomb repulsion and the plasmon-mediated attraction together with an isotropic electron-phonon interaction.

High-temperature copper oxide superconductors exhibit many other properties apparently incompatible with conventional metal physics. The materials compel researchers to develop new experimental techniques and theoretical concepts, which can enhance the understanding of interacting electrons in metals [39].

Exciting results, such as critical-temperature dependence on concentration of dopants with a value of around 100 K for optimal doping and a weak isotope effect, have emerged. To extend the model, researches are investigating lattice excitations caused by charge transfer fluctuations in the copper oxide planes. These give rise to soliton-like waves which propagate along the atomic chains. They can carry charge and pair forming

bound states when the electrons or holes have opposite spins.

The fact that some materials show a magnetic effect at room temperature, typical of superconductivity, strongly suggests that a "shadow" of the superconducting state (formation of Bosons and Cooper pairs) exists even when the material appears normal and may give clues about the underlying causes of the HTS phenomenon. The materials become superconducting only at much lower temperatures. One model proposes that pairing occurs only in narrow stripes, currents flowing over the surface of Type-2 semiconductors, while resistance-free electric current is blocked by intervening stripes of magnetism. Another "shadow" would be the observation that n-doped superlattices show no signs of superconductivity but show a resistance that is a function of temperature and magnetic intensity.

A research team cooled a sample of Bi-2212 to below the transition temperature and found that the light reflected from it shifted towards higher frequencies and away from the infrared region of the spectrum. This indicates that the material absorbs more infrared light when it is in its superconducting state. Also indicated is that that the electrons in Bi-2212 pair up because they have the lowest kinetic energy in this arrangement. This could lead to a stable superconducting state even if the electrostatic repulsion between two electrons tends to push them apart. If the shift of 'spectral weight' occurs in all high-temperature superconductors, it would prove that the BCS mechanism is not the only way to achieve superconductivity [40].

Signs of T_C enhancement can occur when the weight ratios of alternating CuO_2 planes were increased to create new Sn-based superconducting compounds. The only limitation to planar weight-tilting appears to be that it must be limited to either

the copper-oxide planes or the insulating layers. Attempting both in the same molecule was found to depress T_C. The new material produced a Meissner transition near 104 K, and a drop to zero resistance at 101 K - more than a 30 degree improvement over the prototype [41].

The presence of a strong electron correlation in cuprates has been demonstrated by the existence of the insulating state of the undoped cuprates. The transfer of spectral weights from high to low energies, with doping. and the small electron-phonon coupling can be deduced from transport measurements. Numerous models have adopted the strong electron correlation manifested by spin fluctuations as the mechanism for high temperature superconductivity.

The challenge of solving the puzzle of HTS has led to great advances in experimental techniques. Using the high resolution of angle resolved photoemission, instruments can create detailed images of electron energy distributions. Scanning tunneling electron microscopes have been used to study charge ripples around impurities in which wavelength and frequency variations are determined with great accuracy and consistency with theoretical predictions [42].

A d-wave is a form of electron pairing in which the electrons travel together in orbits resembling a four-leaf clover. The d-wave wave function helps theoreticians describe and predict electron behavior of Cooper pairs. The d-wave models have gained substantial support recently over s-wave pairing as the mechanism by which high-temperature superconductivity might be explained. While phase-sensitive experiments clearly show that the superconducting order parameter has a d-symmetry, suggesting that the prominent role of strong electron correlation in cuprates, renormalization of the

electron-phonon interaction and the residual Coulomb repulsion were later proposed to be able to give rise to a d-wave as well.

The electron-phonon interaction alone cannot account consistently for the high-T_C and the many anomalous normal-state properties. However, as noted in this thesis, an electron-phonon interaction, with a combined Coulombic effect of strong electron correlation and interaction, may be the cause. It has been proposed that a large electron-phonon interaction may be predominantly responsible for the T_C and that such an effect, renormalized by the strong electron correlation, can account for the unusual normal and superconducting-state properties observed.

Since 1986, remarkable progress in the areas of basic research and technological applications has been made on the high-T_C cuprate superconductors. Using polycrystalline and single crystal bulk and thin film materials has made it possible to make reliable measurements of the physical properties of these materials and to optimize superconducting properties. The next decade of research on the high-T_C cuprate superconductors will yield significant advances toward the development of a theory of HTS. It is possible that significantly higher values of T_C will be found in new cuprate compounds or other classes of materials.

There seems to be no theoretical or experimental reason that T_C cannot be further raised to room temperature. A wide variety of cooperative phenomena have been shown to exist in compounds with strong electron correlation. The ordering temperatures of these cooperative phenomena can be more than several hundred degrees Kelvin. Given the similarities between these compounds and cuprates, it appears that a superconductor

with a T_C equal to or higher than room temperature, is not an impossibility. The limit may eventually be the melting point of the compound.

From the standpoint of technological applications, superconductors are used to make very powerful electromagnets, such as those used in MRI machines and the beam-steering magnets used in particle accelerators. Superconductors have also been used to make digital circuits and microwave filters for mobile phone base stations. Other possible applications arise where the relative efficiency, size and weight advantages of devices based on HTS outweigh the additional costs involved.

CHAPTER 5

THE DETECTION OF SUPERCONDUCTIVITY USING SYNTHETIC IMAGING

5.1 Synthetic Imaging

5.1.1 General Principles

Sensor array synthetic imaging has numerous applications in many diverse fields of science and engineering, particularly where the goal is to study propagating wave fields. Synthetic imaging can be used in astronomy, radio astronomy, medical diagnosis, radar, communication, sonar, nonrestrictive testing, seismology, seismic exploration, and the detection of hidden explosives [43]. The purpose of this section is to determine what kind of sensor array design can be used to detect superconductivity in a material without contact with the material and the sensor array. Various array geometries will be explored to determine which type of array would be feasible for detecting superconductivity.

Sensor arrays should be able to extract range and direction about wave propagating from a source. The instantaneous response of an interferometer to point sources can be analyzed by knowing the signal paths. The tools of sensor array synthetic imaging are primarily in beam formation where the goal is the reduction of side lobes in the reflectivity profiles. In the real world, different types of wave fields are used in different applications. Acoustic waves in sonar, mechanical waves in seismic exploration, electromagnetic waves in radar, and radio astronomy are just a few examples.

In many applications, it may be impossible to determine if a source point is located in the near or far field. To understand the errors induced by assuming far field propagation instead of near field, let ε_M be the angle between the rays emanating from

the source to the array origin and to the mth sensor as shown in Figure 5.1c. This angle represents the error we want to estimate. Simple applications of the law of sines yields $\sin\varepsilon_M = \sin\psi_M(x_M/r_M)$, with ψ_M denoting he angle between the vectors $\vec{x}_M$ and $\vec{x}_0$. When $r_M >> x_M$, the source is located well outside the array's aperture and $\varepsilon_M \to 0$ as $r_M \to \infty$. But if r_M is of the order of the radius of the sensor aperture, ε_M increases dramatically. In the far field (Figure 5.1a), knowing the difference of the angle the wave front makes with the center of the array and another sensor node, one can determine the phase difference with respect to the center of the array. Conversely, knowing the phase difference between the center of the array and a sensor node, one can determine the direction of the wave front. Using the delay in arrival time of the wave front between a pair of antennas, a measurement will yield an angle at which the object is located from the sensor.

However in the near field (Figure 5.1b), the wave front makes a different angle with the center of the array (α_0) and a sensor node (α_1,α_2), but the phase difference is 0, so a determination of the direction of the source point is impossible to determine. Figure 5.2a shows wave fronts are parallel to a plane containing the sensor elements of the array where the individual wave front arrive at all the sensors on a planar array at the same time. The time delay between detection of a wave front at two different sensors is a function of baseline between the sensors and the angle of incidence (Figure 5.2b) incident upon a planar arrangement of sensors. The wave front is detected simultaneously at all sensors indicating the presence of a point source at infinite distance from the detection array. If the source at infinity is not directly in front of the detector array, the incoming plane waves intersect the array at an incident angle α. The phase difference of two

nodes, separated by d, assumes the far-field form $kb\sin\alpha$, where k is the wave number of the incoming wave. The time delay between detection of the wave front at one sensor compared to the other is determined by α and the spacing b between the sensor pair.

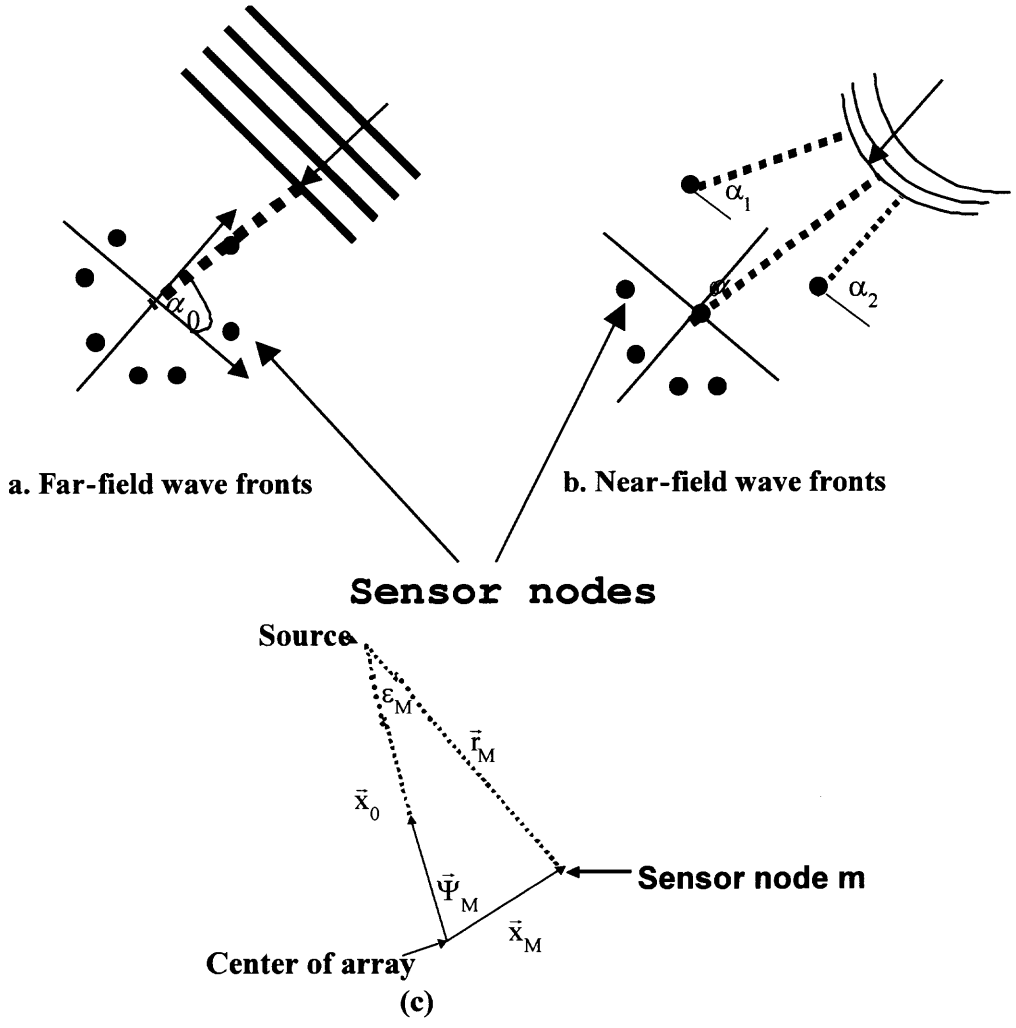

Figure 5.1 (a) Near field wave fronts, (b) Far field wave fronts, (c) Geometry of array and source.

For the imaging of a far field object, standard Fourier transforms of sensor pair correlation pairs gives the reconstructed real image of the object. If the object is not far away from the sensor nodes, the wave fronts from a point object are not planar but curved and the synthesized image is distorted. Synthetic imaging is still possible if a sensing

geometry can be devised so the phase differences between pairs of sensor nodes can be expressed in the far-field form. Adjusting the placement of the sensors to match the circular wave fronts, the sensors detect the same wave fronts simultaneously. Distortion of the planar array to match the curvature of the spherical wave fronts is not possible.

The problem now is to match the curvature of the wave front with the curvature of the sensor spacing. In order to generate images in the near field of the imaging array, curvature can be adjusted so that the object is in focus. Using a parabola to match the curvature may be difficult since the radius of curvature of a parabolic array varies.

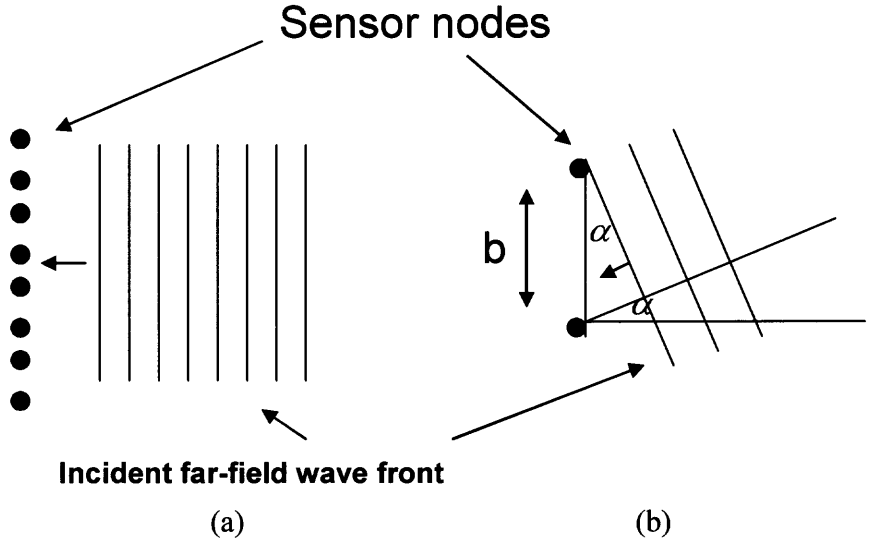

Figure 5.2 (a) Far field wave fronts parallel to sensor plane, (b) Far field wave fronts at an angle to sensor plane.

As shown in Figure 5.3b, by placing the sensors on a curved surface, the curvature of the wave fronts and sensor array spacing are matched. In this case, an individual wave front is detected simultaneously by all sensors. This is equivalent to Figure 5.1a for an object very far away. For a point object placed at some angle α (Figure 5.2b), there will be a phase delay in detection by successive sensors which can be

related to the angle α in analogy with Figure 1.4b. Let d_{MN} be the distance between nodes m and n, Δt_{MN} is the time delay between the two nodes, and R_0 the radius of curvature of the spherical array. The angle β is formed by subtending the lines from sensor nodes to the radiation source at O and is given by $\sin\beta = d_{MN}/(R_0 + ct_{MN})$. Calculating α using just the baseline and time delay is impossible considering the geometry in Figure 5.4.

Besides physically moving the sensors, keeping the sensors fixed in a plane and by adding a phase delay to the individual detector signals during the signal processing of the detected wave fronts, can accomplish the same. By using the electronic delay method, an interferometric imaging array could be electronically programmed to image objects at different distances. This electronic method would probably be easier and cheaper to implement and allow for real-time imaging of an object.

The basic technique of radio interferometry utilizes signals at two or more points in space on the surface of an array containing sensor nodes. Calculating the coherence function of all pairs of sensor nodes can be used to synthesize the image of an object. Applying the vanCittert-Zernike theorem, if a large number of points in the u-v plane are generated, the original brightness distribution can be synthesized. Using just a single pair of sensors for synthetic imaging would be insufficient according to the van Cittert-Zernike theorem (see Appendix C). Each sensor measures the amplitude and phase of incoming radiation and pairs of sensors measures one spatial Fourier component of the incoming wave front.

There are N(N-1)/2 possible pair combinations along the distance between two sensors for a system containing N sensors. An image is generated from the spatial Fourier

components of all the different pair combinations. The sharpness of imaging depends on the coverage of the number of different points generated in the u-v plane. The u and v points are determined not by absolute coordinates but relative positions of the sensor nodes. Generation of unique u, v points can be achieved by a completely random arrangement of sensor nodes. In actuality, each u, v pair has a mirror image in the u-v plane so the total number of point generated is N(N-1).

Wave fronts in the far field region are flat and the phase difference between two sensor points 1, 2 can be expressed as $kb\sin\alpha$. Taking the Inverse Fourier Transform (IFT) of all the coherence functions in the far field form, for all pairs of sensor nodes, one can reconstruct an image of an object. Sensor array that receive wave fronts in the near field can also reconstruct an image of an object if the phase difference between any pair of nodes can be expressed as a function of the wave number of the incident radiation, the baseline and an angle of incidence. Points in u-v space can be generated and knowing the phase differences between the sensor points, a synthetic image of an object can be created. The are three possible types of sensor array systems that may be used for reconstructive imaging: parabolic arrays, spherical arrays, and planar arrays.

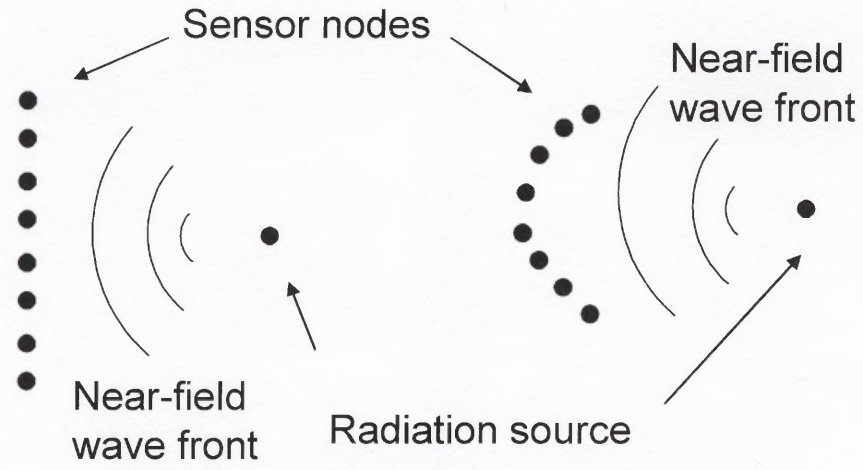

Figure 5.3 (a) planar array, (b) curved array. In (a), nodal phase differences are zero with time delays. In (b), nodal phase differences are zero but with no time delays.

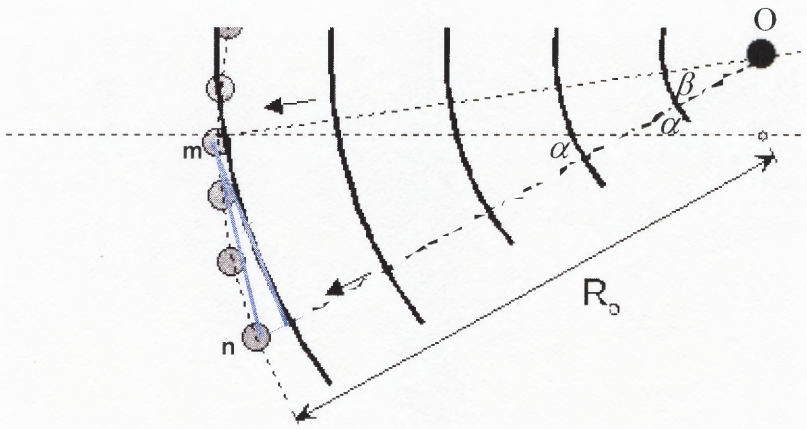

Figure 5.4 Geometry of sensor nodes and near field source.

5.1.2 Coherence Function for Sensor Pairs on a Parabolic Array

The wave fronts from a light source, at distance d from the z-axis in the x-y plane, arrive at points 1, 2 in the x-z plane (Figure 5.5) and are:

$$\psi_1 = E_0 exp(i(kr_1 - \omega t))/r_1 \tag{5.1}$$

$$\psi_2 = E_0 exp(i(kr_2 - \omega t))/r_2 \tag{5.2}$$

where the displacements from the origin are:

$$r_1 = \sqrt{d^2 + R_1^2} \tag{5.3}$$

$$r_2 = \sqrt{(R_2 \cos\beta)^2 + (R_2 \sin\beta - d)^2} \tag{5.4}$$

and the sensor nodes are confined to the x-z plane. The phase difference between points 1, 2 are:

$$\begin{aligned} \phi_{1,2} &= k[\sqrt{d^2 + R_1^2} - \sqrt{(R_2 \cos\beta)^2 + (R_2 \sin\beta - d)^2}\,] \\ &= k[R_1\sqrt{(d/R_2)^2 + 1} - R_2\sqrt{1 - 2\sin\beta(d/R_2) + (d/R_2)^2}\,] \end{aligned} \tag{5.5}$$

For small angle approximations, the phase difference and hence the coherence function never assume the far field form so using parabolic arrays for synthetic imaging is not a possibility.

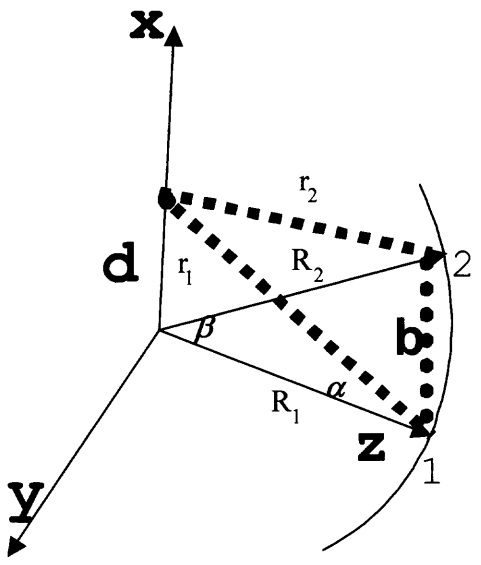

Figure 5.5 Point source at d producing wave fronts at points 1,2 on the surface of a parabolic array.

5.1.3 Coherence Function for Sensor Pairs on a Spherical Array

The wave fronts from a light source, at distance d from the z-axis in the x-y plane, arrive at points 1, 2 in the x-z plane (Figure 5.6), travel along paths r_1 and r_2 and are given by Equations 5.1 and 5.2, where

$$r_1 = \sqrt{R_0^2 + d^2} \tag{5.6}$$

$$r_2 = \sqrt{(R_0 \cos\beta)^2 + (R_0 \sin\beta - d)^2} \tag{5.7}$$

Since the sensor nodes are in the x-z plane, the baseline b is the vertical projection of point 2 to the z-axis. The correlation c(1,2) between the two wave fronts at points 1,2 is the real part of the product of one wave times the complex conjugate of the other:

$$c(1,2) = E_0^2 \cos(k[\sqrt{R_0^2 + d^2} - \sqrt{(R_0 \cos\beta)^2 + (R_0 \sin\beta - d)^2}])/\sqrt{R_0^2 + d^2}\sqrt{(R_0 \cos\beta)^2 + (R_0 \sin\beta - d)^2} \tag{5.8}$$

C(1,2) can be simplified using the above and $R_0^2 + d^2 = R_0^2/(\cos\alpha)^2$.

$$c(1,2) = E_0^2 \cos(k[(R_0/\cos\alpha)(1 - \sqrt{1 - 2db\cos\alpha^2/R_0^2}])/R_0^2\sqrt{(1 - (2db(\cos\alpha)^2/R_0^2)} \tag{5.9}$$

In the limit as $b, d/R_0 \to 0$, $\sqrt{1 - 2db(\cos\alpha)^2/R_0^2} \to 1 - db(\cos\alpha)^2/R_0^2$. The denominator in Equation 5.9 can be set to R_0^2 and in the numerator $1 - \sqrt{1 - 2db\cos\alpha^2/R_0^2} \to db\cos\alpha^2/R_0^2$.

Noting $b = R_0 \sin\alpha$ and using the geometry of Figure 5.6, the correlation for a node pair now becomes:

$$c(1,2) = E_0^2 \cos(kb\sin\alpha)/R_0^2 \tag{5.10}$$

and hence the phase difference now assumes the far field form.

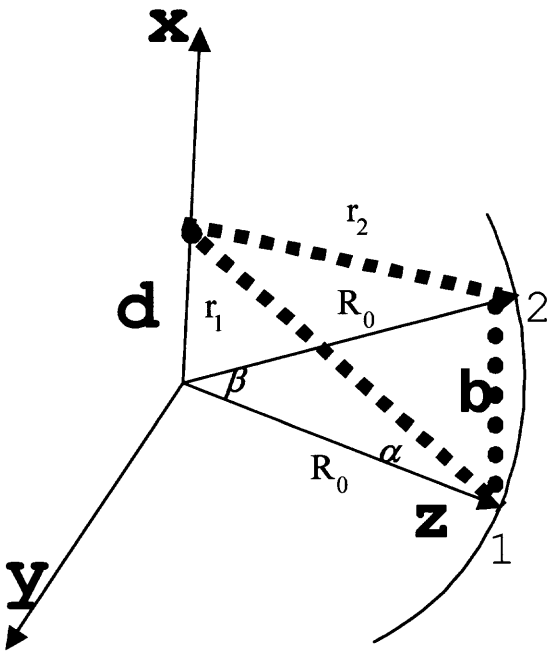

Figure 5.6 Point source at d producing wave fronts at points 1, 2 on the surface of a spherical array.

5.1.4 Coherence Function for Sensor Pairs on a Planar Array

The wave fronts from a light source, at distance d from the z-axis in the x-y plane, arrive at points 1, 2 in the x-z plane (Figure 5.7), and are given by Equations 5.1 and 5.2, where $r_1=\sqrt{d^2+Z_0^2}$ and $r_2=\sqrt{(x-d)^2+Z_0^2}$.

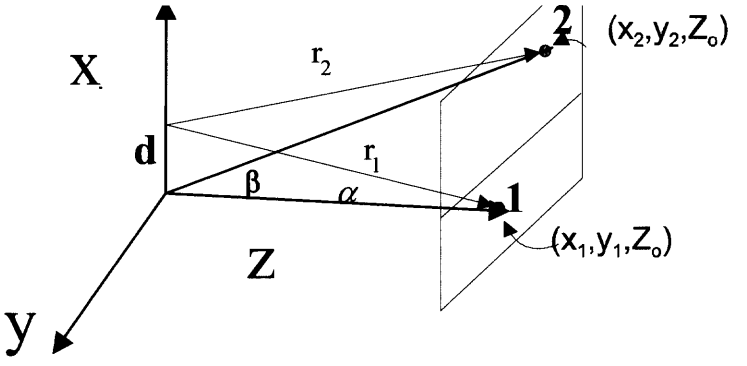

Figure 5.7 Point source at d producing wave fronts at points 1, 2 on the surface of a planar array.

Thus, the phase difference between points 1, 2 can be expressed as:

$$\varphi_{1,2}=k(r_1-r_2)=k(\sqrt{Z_0^2+d^2}-\sqrt{Z_0^2+(b-d)^2})$$

$$=k(\sqrt{d^2+Z_0^2}-\sqrt{b^2+Z_0^2-2db+d^2})$$

$$=k\sqrt{d^2+Z_0^2}(1-\sqrt{1+b^2/(d^2+Z_0^2)-2db/(d^2+Z_0^2)}) \quad (5.11)$$

Using the BET and $b,d/Z_0\rightarrow 0$, the phase difference reduces to

$$\varphi_{1,2}=k\sqrt{d^2+Z_0^2}(1-\sqrt{1+b^2/(d^2+Z_0^2)-2db/(d^2+Z_0^2)})$$
$$=k\sqrt{d^2+Z_0^2}db/(d^2+Z_0^2)=kb\sin\alpha \quad (5.12)$$

The correlation now becomes:

$$c(1,2)=E_0^2\cos(kb\sin\alpha)/(r_1r_2) \quad (5.13)$$

The coherence function for sensor nodes on a planar array can assume the far field form.

5.2 Far Field Form of Phase Difference between Two Sensor Points in a Planar Array

Understanding the u-v plane and the 2D Fourier Transform (FT) and how they relate to synthetic imaging, is essential in order to introduce the corrections in the near field. It is imperative to explain how the Van Cittert-Zernike theorem relates the interferometric correlation of sensor pairs in the imaging array plane to the amplitude of the radiation at the surface of the object [44]. An incremental source of radiation in localized over an area dS' on the x'-y' plane (Figure 5.8). Φ_0 is the surface intensity density at source dS'. The source area can be self-illuminating or irradiated from another source of radiation in back or in front of the x'-y' plane. The planar sensor array is entirely in the x-y plane at $z = Z_o$. The contribution to the total electric field from the infinitesimal surface dS' at a two sensor elements in the sensor array located at (x_1,y_1) and (x_2,y_2) can be expressed as:

$$dE_1 = (\Phi_0(x',y')/r_1)\, exp(i\omega t - ikr_1)dS' \tag{5.14}$$

$$dE_2 = (\Phi_0(x',y')/r_2)\, exp(i\omega t - ikr_2)dS' \tag{5.15}$$

where r_1 and r_2 are given by:

$$r_j = \sqrt{(x'-x_j)^2+(y'-y_j)^2+Z_0^2} \tag{5.16}$$

In Equations 5.14 and 5.15, the electric field is described as a spherical wave whose amplitude is decreasing with propagation distance. The mathematical form of a spherical wave is a solution to the wave equations derivable from Maxwell's Equations [45] which assume the form of a spherical wave [46]. The scalar electric fields are uncorrelated and are polarized in the same direction. For interferometric detection, the correlation of the electric fields at the various pairs of sensors is calculated. It can

be shown that the mutual coherence function of the electric fields at points (x_1,x_2) and (y_1,y_2) can be written as:

$$C_{1,2} = \int_S \frac{\sigma_E(x',y')exp(ik(r_1 - r_2))}{r_1 r_2} dS' \tag{5.17}$$

where $\sigma_E(x',y')$ is the time-averaged intensity of the surface at dS' and the integral is over the surface S of the radiating surface.

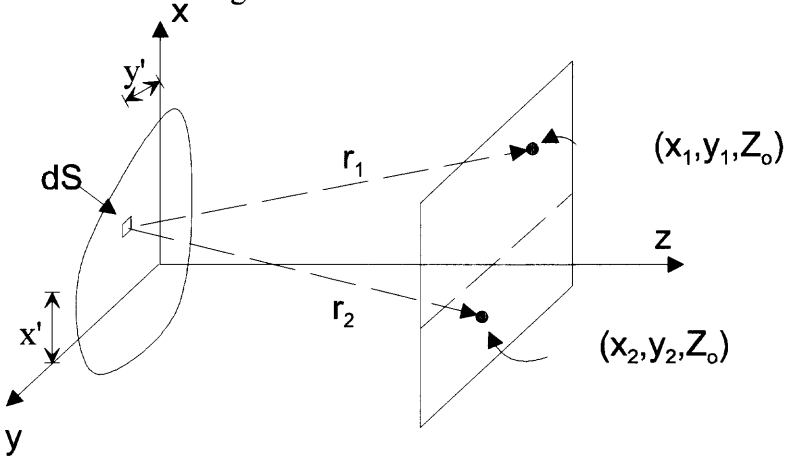

Figure 5.8 Source dS' irradiating a pair of sensors.

Using the expression in Equation 5.16, the distances to the two sensor elements can be shown to be:

$$r_j = Z_0\sqrt{1+(x'-x_j)^2/Z_0^2+(y'-y_j)^2/Z_0^2}$$

$$= Z_0\sqrt{1+((x')^2-2x'x_j+(x_j)^2)/Z_0^2+((y')^2-2y'y_j+(y_j)^2)/Z_0^2} \tag{5.18}$$

The prime squared terms in the above don't disappear automatically. However, if x'/Z_0, y'/Z_0, x/Z_0, $y/Z_0 << 1$, one can apply the Binomial Expansion Theorem (BET) and the expressions for r_1 and r_2 becomes:

$$r_1 - r_2 = \frac{x_1^2 - x_2^2 + y_1^2 - y_2^2}{2Z_0} + \frac{(x_2 - x_1)x' + (y_2 - y_1)y'}{Z_0} \tag{5.19}$$

Using the following new variables, $u = k(x_1 - x_2)/2\pi$, $v = k(y_1 - y_2)/2\pi$, $\xi = x'/Z_0$, $\eta = y'/Z_0$, assuming $r_1 \cong r_2$ and absorbing both into σ_E, the coherence function can be cast into the form:

$$C_{1,2}(u,v) = exp(i\delta) \int_{-\infty}^{\infty} \int_{-\infty}^{\infty} \sigma_E(\xi,\eta) exp(-i2\pi(u\xi + v\eta)) d\xi \, d\eta \qquad (5.20)$$

where $\delta = k(x_1^2 - x_2^2 + y_1^2 - y_2^2)/2Z_0 = kb^2/2Z_0$ is a phase shift resulting from an object in the near field of the planar imaging array. If this phase shift can be neglected ($\delta << 1$), Equation 5.20 will then relate the coherence function in the antenna plane to the brightness distribution of the source. By a Fourier transform, the brightness or intensity distribution of the source can be reconstructed by measuring the coherence function for a given arrangement of sensors in the sensor array.

Other forms of the phase ($\delta = n\pi$) are not acceptable since for a given pair of sensors, another pair of sensors in the same approximate spatial region, will have a phase that is different from $\delta = n\pi$ resulting in a phase factor exp[iδ] not equal to one.

The angular resolution of a planar array can be approximated as $\theta = \lambda/b$ and a distance Z_0 away, the lateral spatial resolution is $\Delta L = \theta Z_0 = \lambda Z_0/b$. One can view a high degree lateral resolution of an object occurring when relatively large parts of the object can be fitted into one pixel. High resolution occurs when the smallest linear separable and measurable feature on the imaged surface is achieved, thus distinguishing two separate points on an object.

. To maintain a specific lateral spatial resolution at all distances, the maximum baseline for a planar imaging array can be estimated as $b = \lambda Z_0/\Delta L$. Using $\delta \sim b^2/Z_0\lambda$ as an estimate of the far field limit for a planar array, the limit can be estimated as

$\delta \sim Z_0 \lambda / \Delta L^2$ (Figure 5.9). In order to keep the spatial resolution constant, as Z_0 increases, the baseline b must also increase proportionally. Figure 5.9 shows that when Z_0 increases, δ increases rapidly. Even when the spatial resolution is large, the requirement $\delta << 1$ is never satisfied, indicating that the synthetic imaging using a planar array is not possible.

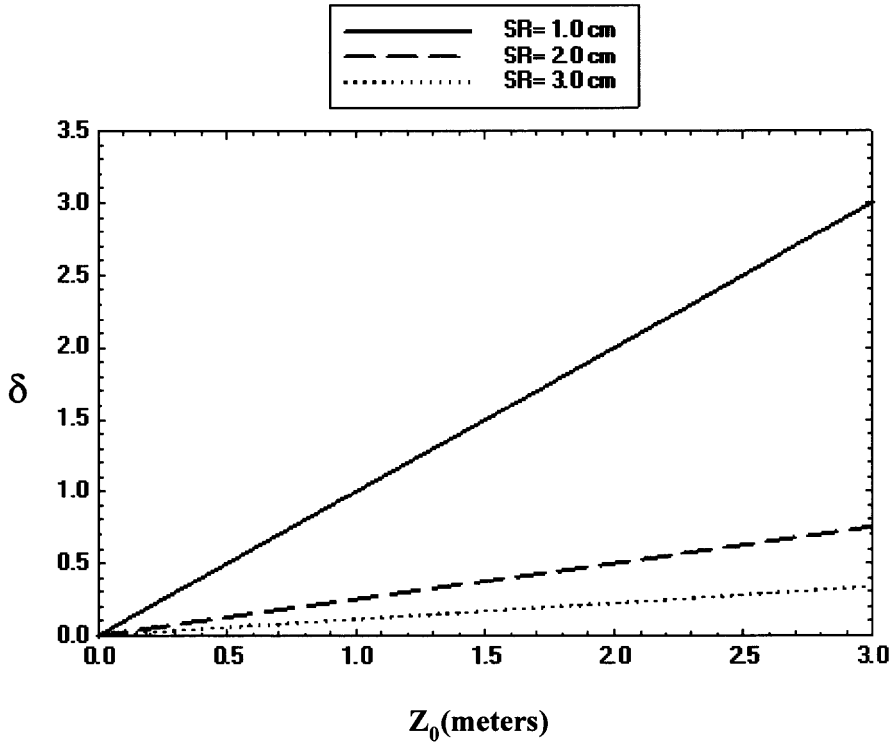

Figure 5.9 Error delta from imaging 1.0, 2.0, 3.0 cm objects, frequency of radiation = 1.0 terahertz.

5.3 Physical Structure of Near Fields Incident upon a Spherical Array

Using a spherical imaging array, the curvature of the imaging array is matched to the curvature of a point source where synthetic imaging may be possible. In Figure 5.10, it will be assumed that any pair of sensors of the spherical imaging array can measure an electric field from an element of surface dS' given by Equations 5.14 and 5.15. The sensors are located at spherical coordinates (R_0,ϕ_1,θ_1) and (R_0,ϕ_2,θ_2) and receive radiation from surface dS'. (R_0,θ,ϕ) denotes the distance from the point to the origin, the angle relative to the z axis and the angle relative to the x axis in the x-y plane, respectively. The source element dS' lies on the surface of the imaged object and sensors can lie on the surface of the sphere. The correlation between the two wave fronts at the two sensors can be calculated using:

$$r_1=\sqrt{(R_0 sin\theta_1 cos\phi_1-x')^2+(R_0 sin\theta_1 sin\phi_1-y')^2+(R_0 cos\theta_1-z')^2} \tag{5.21}$$

$$r_2=\sqrt{(R_0 sin\theta_2 cos\phi_2-x')^2+(R_0 sin\theta_2 sin\phi_2-y')^2+(R_0 cos\theta_2-z')^2} \tag{5.22}$$

Simplifications using trigonometric identities yields:

$$r_1=R_0\sqrt{1-2x' sin\theta_1 cos\phi_1/R_0-2y' sin\theta_1 sin\phi_1/R_0-2z' cos\theta_1/R_0+(x'^2+y'^2+z'^2)/R_0^2}$$

$$r_1=R_0\sqrt{1-2x' x_1/R_0^2-2y' y_1/R_0^2-2z' cos\theta_1/R_0+(x'^2+y'^2+z'^2)/R_0^2}$$

$$r_2=R_0\sqrt{1-2x' sin\theta_2 cos\phi_2/R_0-2y' sin\theta_2 sin\phi_2/R_0-2z' cos\theta_2/R_0+(x'^2+y'^2+z'^2)/R_0^2}$$

$$r_2=R_0\sqrt{1-2x' x_2/R_0^2-2z' y_2/R_0^2-2z' cos\theta_2/R_0+(x'^2+y'^2+z'^2)/R_0^2} \tag{5.23}$$

If x'/R_0, y'/R_0, z'/R_0, x/R_0, y/R_0, $z/R_0 << 1$, one can apply the Binomial Expansion Theorem (BET) and the expressions for r_1 and r_2 now becomes:

$$r_1 - r_2 = x'(\sin\theta_2\cos\phi_2 - \sin\theta_1\cos\phi_1) + y'(\sin\theta_2\sin\phi_2 - \sin\theta_1\sin\phi_1) + z'(\cos\theta_2 - \cos\theta_1) \quad (5.24)$$

Substituting the above into Equation 5.17 yields:

$$C_{1,2} = \exp(ikz'(\cos\theta_2 - \cos\theta_1)) \iint \frac{\sigma_E(x',y')\exp(ik(x'(\sin\theta_2\cos\phi_2 - \sin\theta_1\cos\phi_1) + y'(\sin\theta_2\sin\phi_2 - \sin\theta_1\sin\phi_1)))}{R_0^2} dx'dy' \quad (5.25)$$

Using:

$\xi = x'/R_0$, $\eta = y'/R_0$, $\delta = kz'(\cos\theta_2 - \cos\theta_1)$, $v = k(y_1 - y_2)/2\pi$, $u = k/2\pi(x_1 - x_2)$, and assuming $r_1 \cong r_2$ and absorbing both into σ_E, the coherence function can be cast into the form:

$$C_{1,2} = \exp i\delta \iint \sigma_E(\xi,\eta)\exp(-i2\pi(u\xi + v\eta))\, d\xi d\eta \quad (5.26)$$

If $\exp i\delta$ can be neglected ($\delta \approx 0$), Equation 5.26 will then relate the coherence function in the sensor array to the brightness distribution of the source. Assuming that the azimuth angles of the sensors are not equal, the condition that the $\delta << 1$ implies that $kz' << 1$, so that the depth of focus (z') of the imaging array may be comparable to the wavelength of the far infra-red light (3 microns). However, part of the condition for small angle approximations (x/R_0, y/R_0, $z/R_0 << 1$), insures that the difference of the cosines of the azimuthal angles are very small. Z' can now assume a value much greater than the wavelength of the light and still satisfy the condition $\delta \approx 0$. The spherical sensor nodes used in this thesis are displaced 1 cm to 1 m from the z-axis. For a radius of curvature of 50 meters, the maximum cosine azimuth angle difference for any pair of sensors is.0001 so the depth of focus can be of the order of 50 centimeters and still satisfy $\delta \approx 0$. Arranging the sensors in a circle with the same azimuth angle forces $\delta = kz'(\cos\theta_2 - \cos\theta_1) = 0$.

The form of the coherence function of a spherical array is the same for that of a planar array when $R_0 \to \infty$ since at very large radii of curvature, the surface of the spherical array now becomes flat. When $R_0 \to \infty$, $\exp i\delta = \exp ikz'(\cos\theta_2 - \cos\theta_1) \to 1$ since the azimuth angles are virtually zero. As $Z_0 \to \infty$, $\exp i\delta = \exp ikb^2 / Z_0 \to 1$.

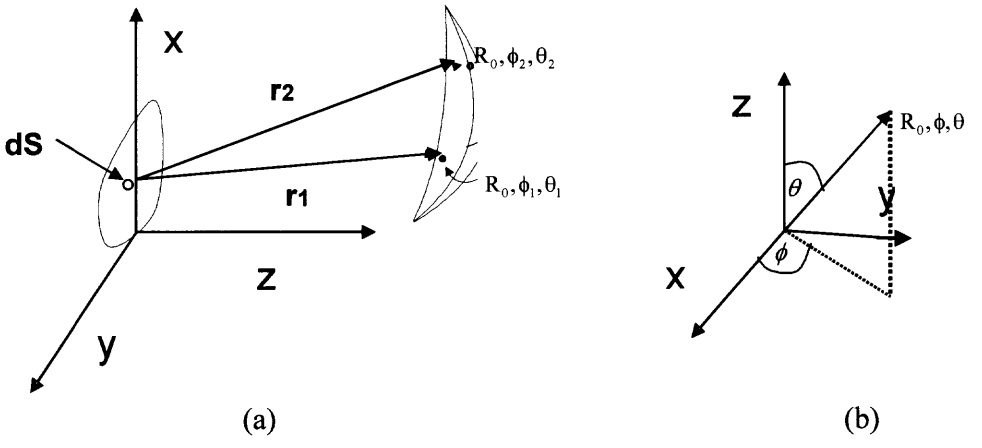

Figure 5.10 (a) Spherical sensor array and imaged object, (b) Spherical coordinate system.

5.4 Synthetic Imaging Using an IFT of a U-V file

Two MATLAB programs simulated an image of a point source (Figure 5.11) using a spherical and circular geometric arrangement of 25 sensor nodes and the approximate 600 points in the u-v plane (Figures 5.12 and 5.13). The programs used the 2-D Inverse Fourier Transform (IFT) of the product of $2r_i r_j$ and the correlation c(i.j) between 2 sensor points located at r_i, r_j to synthesize the intensity distribution on the surface of an illuminated object (see Appendix C). The sensor nodes on the circular array can be considered to lie on the surface of a spherical array with radius of curvature R_0. The sensor coordinates for the spherical array were generated in a spiral to maximize the number of unique u and v points. The sensor coordinates for the circular array were randomly generated evenly for the sake of simplicity. The point source can assume any position relative to the x'y'z' system. The distance of the nodes to the z-axis for the spherical array can vary from 1 centimeter to 1 meter. For the circular array, the sensor nodes are all 1 meter from the z-axis. The Discrete Inverse Fourier Transform of the coherence function reconstructs the image based upon the location of the source and the specified sensor node positions.

The computer simulation verified all of the conditions for near field imaging for both spherical and circular arrays (Figures 5.14 and 5.15). As z' was increased from 0 to 50 centimeters, and then to 100 centimeters, the amplitude of the intensity profiles decreased by 1/3 and then by 2/3 and the half width maximum increased, indicating that the imaging of the point source became blurred and decreased in brightness. For the circular array, there was no change in the intensity profiles as z' was increased - consistent with the fact that $\delta = kz'(\cos\theta_2 - \cos\theta_1) = 0$ for circular arrays. The

width of the half maximum was narrower than for the case with the spherical array. This was consistent with the image profile where the point source image with a circular array had greater resolution.

For the spherical array as $(x'-x)/R_0$, $(y'-y)/R_0$, and $(z'-z)/R_0$ became larger as R_o decreased from 50 to 10 meters and then to 8 meters, the amplitude of the intensity profiles decreased by 1/4 and then by 1/2 but the half width maximum became narrower, indicating that the imaging of the point dimmed and shrunk in size.

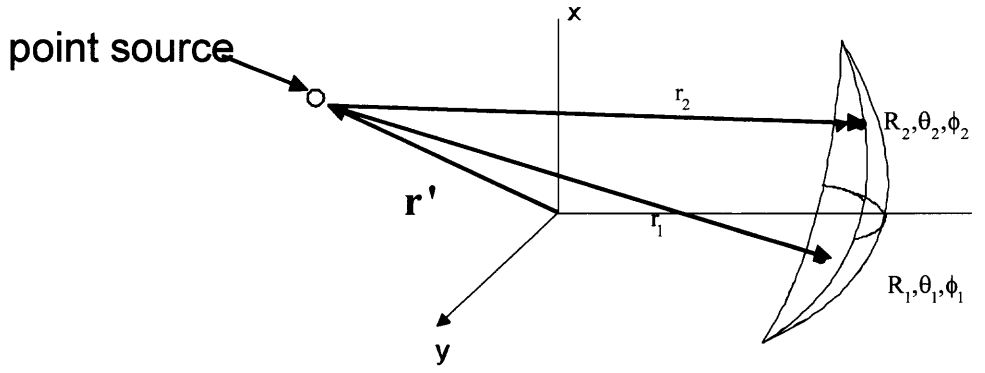

Figure 5.11 Sensor nodes 1, 2 receiving radiation from a source point.

The computer program was coded to produce a spiral arrangement of the sensor nodes. For the circular array, the progressive decrease in amplitude was very different than when a spherical array was used and the amplitude decreased much faster as R_0 decreased. For the circular array, the width of the half maximum also decreased but the intensity decreased more rapidly. A possible explanation is that when the point source is displaced from the z-axis, the more orderly arrangement of nodes on the ring of the circular results in a reduced generation of unique nodes.

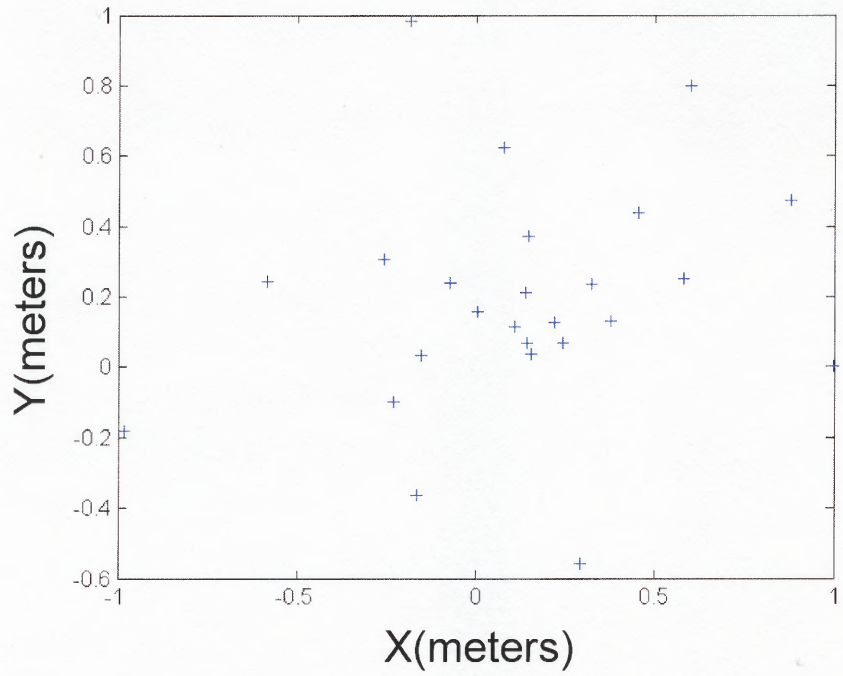

(a)

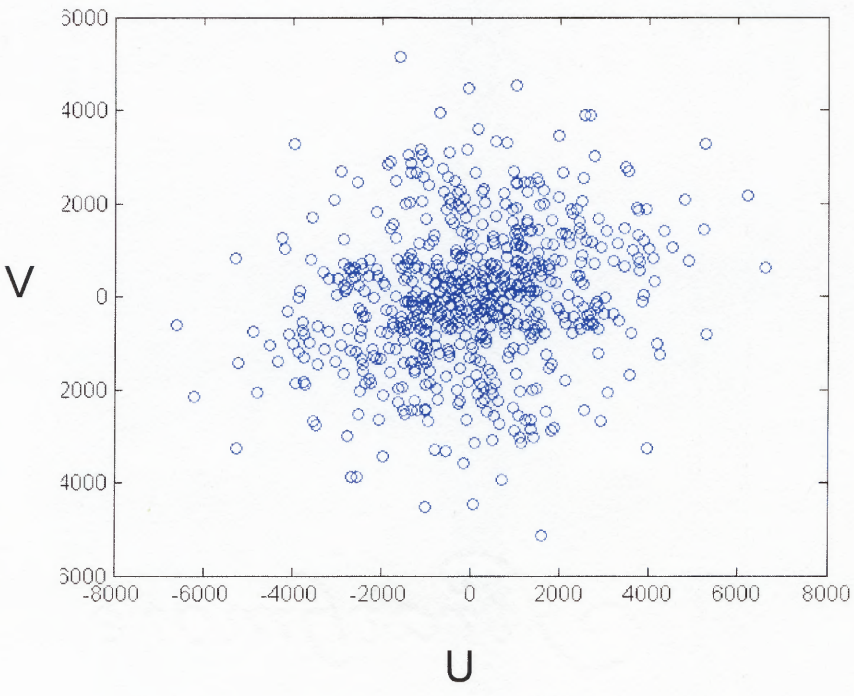

(b)

Figure 5.12 (a) Geometric arrangement of u-v 25 sensor nodes, (b) Nodes generated in space by 25 sensors. Maximum number of unique nodes in upper or lower u-v plane is 300.

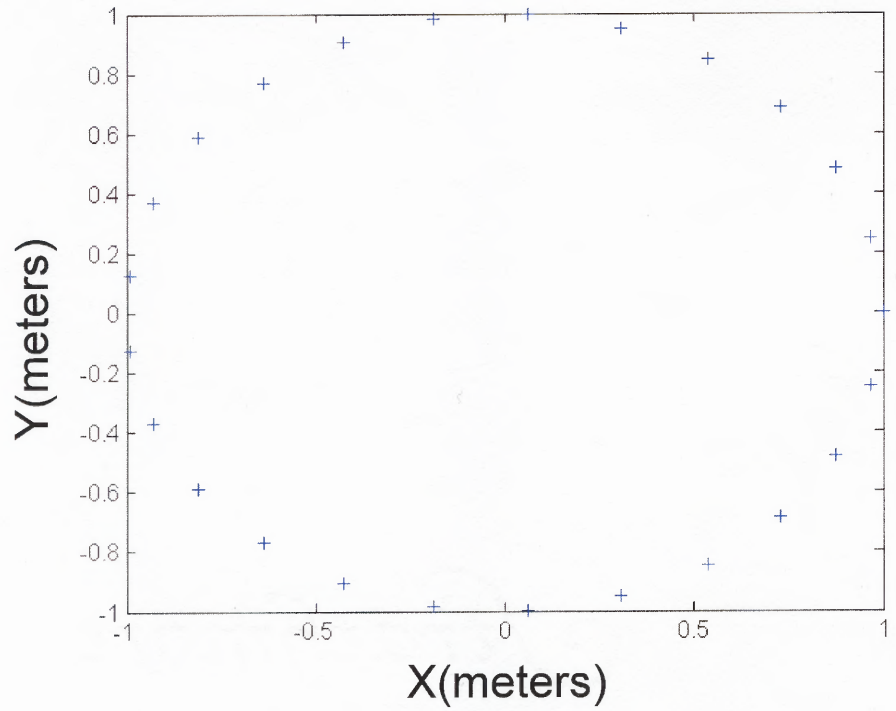

(a)

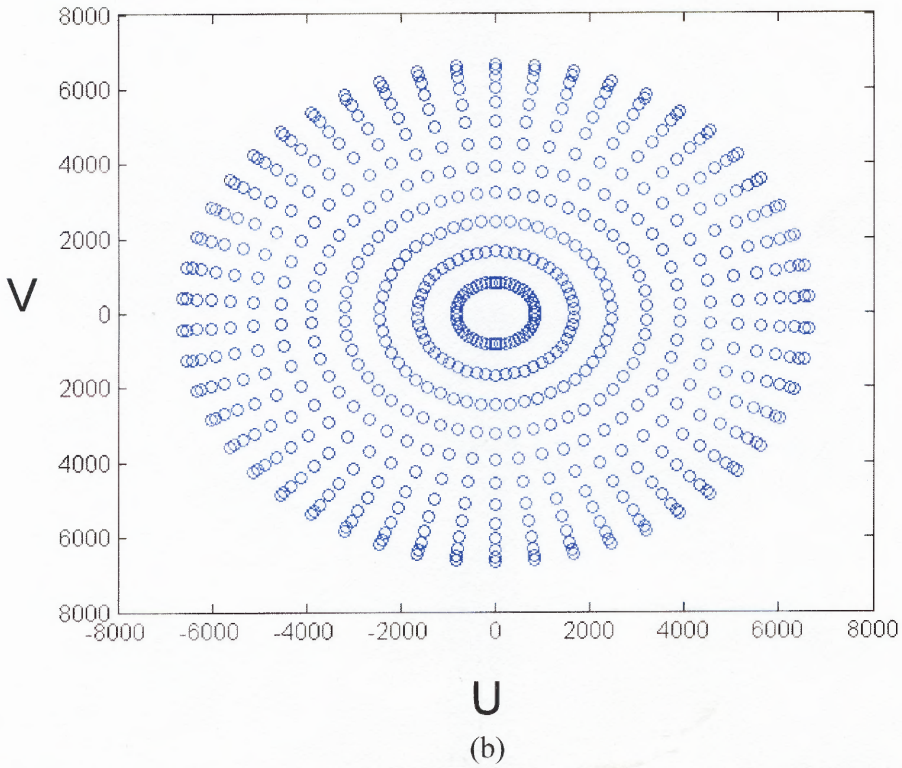

(b)

Figure 5.13 (a) Circular geometric arrangement of 25 sensor nodes, (b) Nodes generated in space by 25 circular sensors. Maximum number of unique node in upper or lower u-v plane is 300.

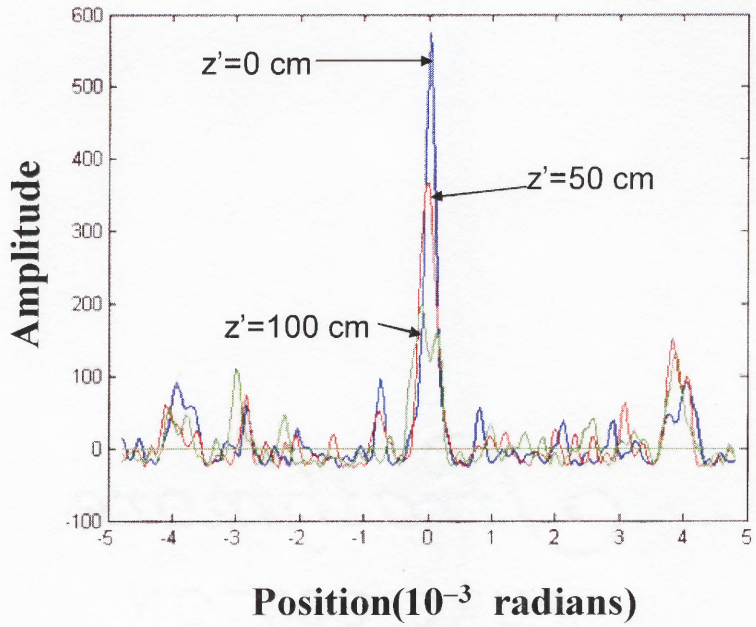

(a) Spherical array with z′ displaced.

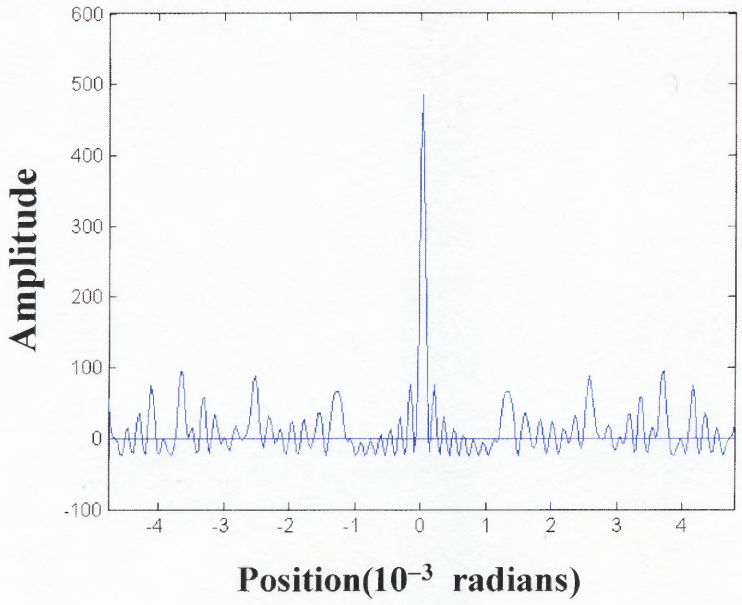

(b) Circular array with z′ displaced.

Figure 5.14 (a) Synthetic imaging of a source point with a spherical array, (b) Synthetic imaging of a source point with a circular array. Distance of the sensor nodes from the z axis range from 1 centimeter to 1 meter, radiation frequency is 10^{12} Hertz, x' = y'= 0 cm, and R_0 = 50 m.

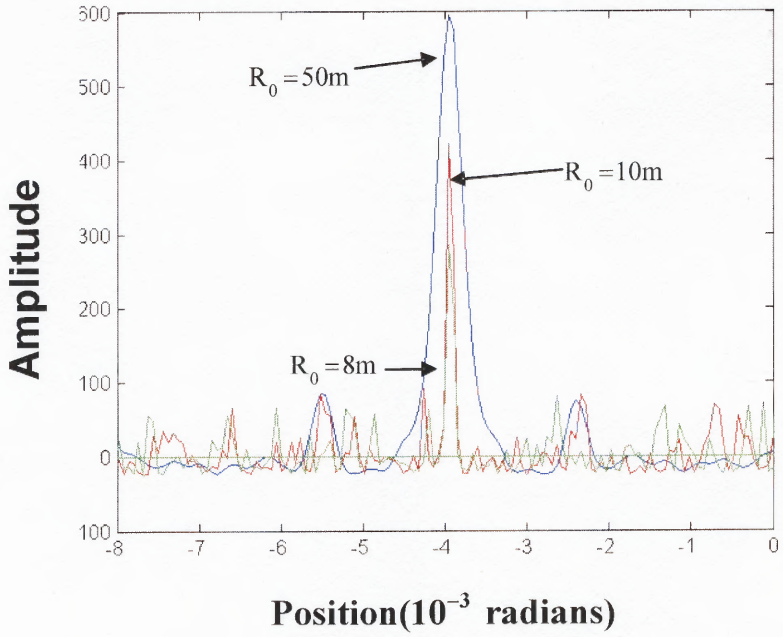

(a) Spherical array with x′and y′ displaced.

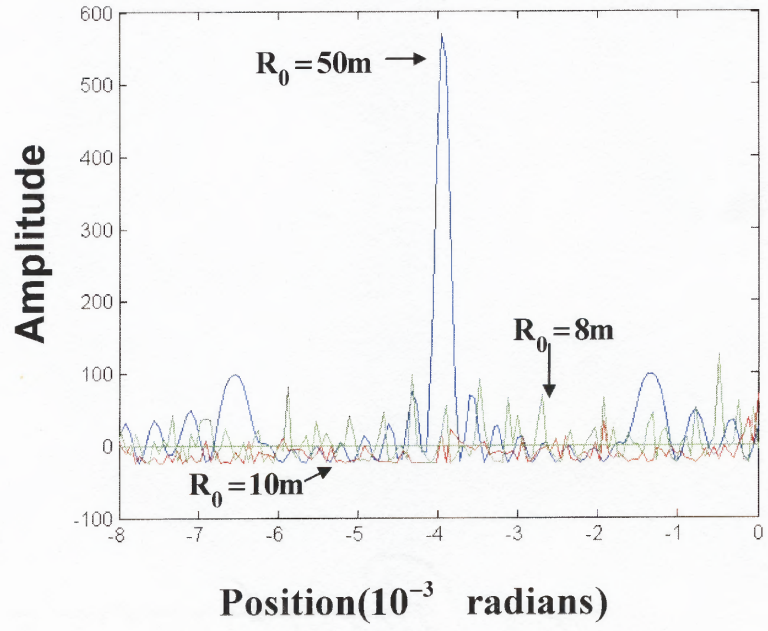

(b) Circular array with x′and y′ displaced.

Figure 5.15 (a) Synthetic imaging of a source point with a spherical array, (b) Synthetic imaging of a source point with a circular array. Distance of the sensor nodes from the z axis range from 1 centimeter to 1 meter, r'=(−10,10,0)cm, and the radiation frequency is 10^{12} Hertz. Point source and focal point lie on the same plane.

5.5 Synthetic Imaging and the Detection of Superconductivity

Small angle approximations are an absolute requirement in the synthetic imaging of a nano superlattice with a spherical array. However, the spatial resolution is in the order of 1-100 Angstroms and is given by $R\lambda/b$. The baseline b is about 1/10 the radius of curvature R of the spherical array. Letting R = 1.0 meter and b = 10 centimeters, resolutions of 1 and 100 Angstroms would require the radiation frequency of the source to be of the order of 10^{19} and 10^{17} Hertz respectively. Such high frequencies would destroy the matrix of a semiconductor. If infrared radiation is used, the minimum resolution would be 10^{7} Angstroms or 1.0 millimeter. Imaging of a nano structure with a spherical array would thus have restrictions (Table 5.1). However, a relatively large nano object, such as a superlattice, could be imaged as a whole against a macro size substrate. In addition, macro size semiconductors could also be imaged.

The technique for detecting superconductivity in small samples of high temperature superconductor can also be done without contacts but with the sample localized in the same region as the measuring devices. There is also the additional problem of the depth of focus z. The magnitude of the phase δ can be calculated knowing the radius of curvature and the sensor pair baselines. Using $\delta = kz(\varphi_{MAX} - \varphi_{MIN})$, where φ_{MAX} and φ_{MIN} are the maximum and minimum azimuthal angles for sensor nodes on the surface of the spherical array, then $\varphi_{MAX} - \varphi_{MIN} = 1.59 \times 10^{-6}$ radians for a spherical array with a radius of curvature of 50 meters and a maximum baseline of one meter. Designing a spherical array with such dimensions is virtually physically impossible. The only solution is to use a circular array where all of the azimuthal angles are equal which forces δ to zero. In Figure 5.1

the dimensions of the sample and window are 30 and 15 mm, respectively. According to Table 5.1, the frequency of the radiation source can be at least $3.0x10^{12}$ Hertz and with no problems with either resolution of depth of focus.

Table 5.1 Wavelength, Frequency and SR (R_0 = 1.0 meter, b = 10 cm, SR, λ are in $\mathring{A}$)

λ	ν	$SR=10\lambda$
1	$\mathbf{3.0x10^{18}}$	**10**
10	$\mathbf{3.0x10^{17}}$	**100**
$\mathbf{10^4}$	$\mathbf{3.0x10^{14}}$	$\mathbf{10^5}$
$\mathbf{10^6}$	$\mathbf{3.0x10^{12}}$	$\mathbf{10^7}$

The sample could be placed within the inductor of a Colpitts oscillator. The precise quantity of feedback is finely adjusted to maintain oscillation at set amplitude. The presence of superconductivity is detected through a small but sudden change in frequency and an increase in the gain required to maintain oscillations. Upon cooling through the transition temperature of T_C, a cuprate superconducting sample in an induction coil will experience a sharp reduction in Q (gain) corresponding to a loss of energy to the sample. This loss will reach a maximum just below T_C. Since no electrical contacts are necessary, the technique is suitable for samples in either bulk or powder form. However, the technique is not remote so the presence of cryogenic temperatures may affect the measuring apparatus.

To detect superconductivity remotely using a spherical array, a plausible method would be to follow a scheme based reflectivity profiles and parameters in terms of R (Figure 5.17). The source of radiation could beam at the material in a normal incidence and a spherical array could be used to determine the existence of energy

absorption in a normal state semiconductor (Figure 5.18). R can be determined knowing the reconstructed intensity of radiation incident upon the surface of the semiconductor. R can also be determined theoretically from the electromagnetic boundary conditions on the surface of the conducting semiconductor. Ambient background interference may cause a problem in reconstructing the intensity profiles of the semiconductor.

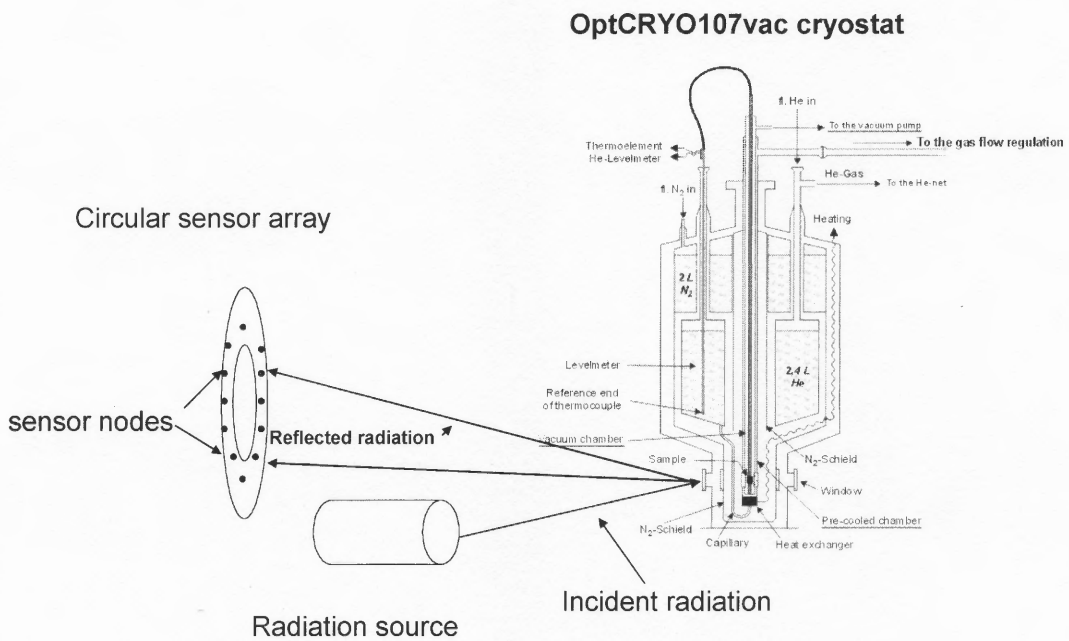

Figure 5.16 Circular array imaging sample in a cryostat. Window-to-window distance for transmission geometry: 120 mm, windows diameter 15 mm, sample space: 30 mm.

However, an intensity vs. frequency profile could still be used to determine the onset of superconductivity. The "distorted" profiles resulting from interference are repeated with the same range of frequency scans and any noticeable disruption in the profile can be used to deduce the presence of superconductivity as the temperature of the superconductor is lowered towards T_C.

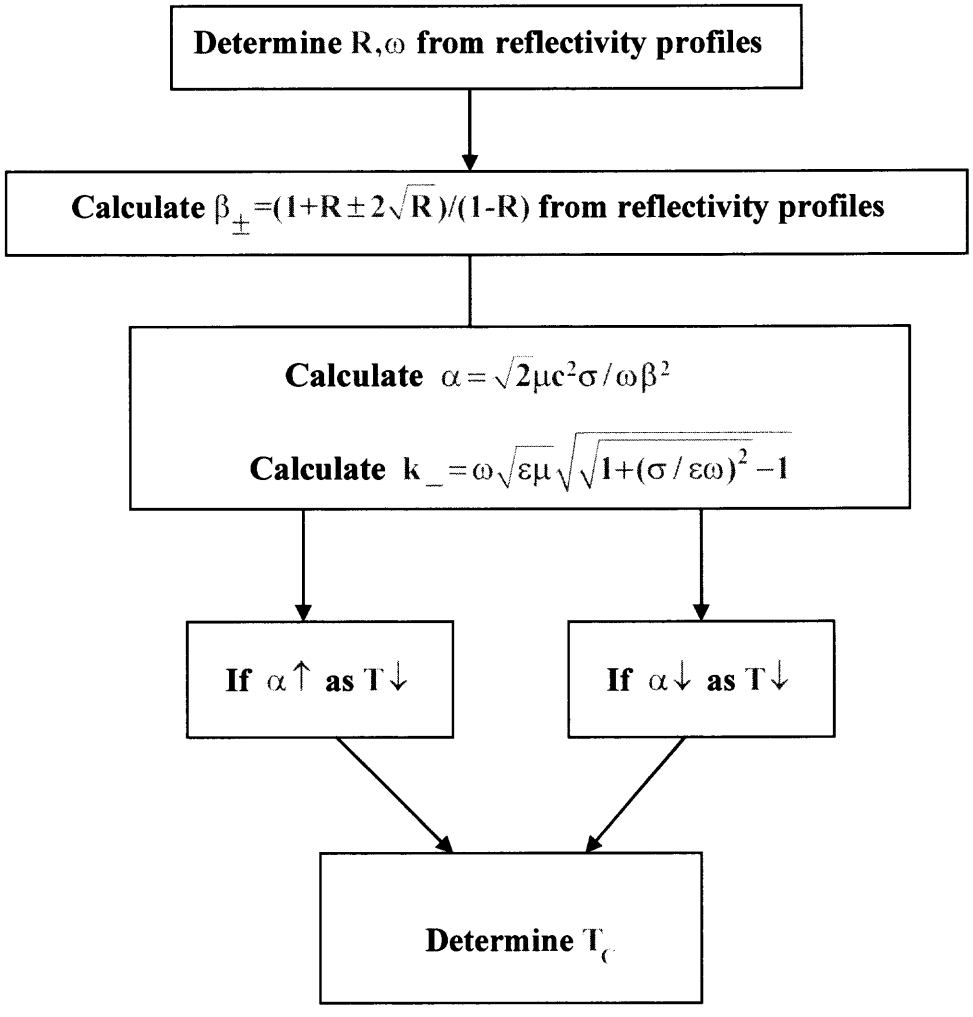

Figure 5.17 Scheme for determining superconductivity in a superlattice using a circular array.

In a more analytically way, one can determine the onset of SC my defining certain variables and conditions (see Appendix D and Figure 5.17). If the imaginary part of a k vector ($k\_$) of an EM wave in a material is negligible, if $1 >> \sqrt{2}\sigma\mu_0 c^2/(\omega\beta^2)$, then there is no energy absorption in the semiconductor; else if $1 << \sqrt{2}\sigma\mu_0 c^2/(\omega\beta^2)$, then energy is being absorbed.

An EM wave entering a semiconductor in a SC state, the B field drops off

exponentially [47] and magnetic fields are confined to an area within the London penetration depth λ_L. The wave must travel a distance λ_L before the fields drop off by a factor of e^{-1}. The magnetic fields are confined to a region not far from the surface of the material whose spatial extent is λ_L (Figure 5.18). For an EM wave entering a semiconductor in a normal state, the imaginary k vector may be such that the electric and magnetic fields of a wave dissipates by a factor of e^{-1} at a distance into a conductive medium that may be less than or greater than to λ_L. If $k_- < \lambda_L^{-1}$, then the wave must travel a distance greater than λ_L before the field drops off by a factor of e^{-1}. As the medium becomes SC, k_- and $\sqrt{2}\sigma\mu_0 c^2/(\omega\beta^2)$ must both increase so that $k_-\lambda_L = 1$ when the material is SC. If $k_- > \lambda_L^{-1}$, then the wave must travel a distance less than λ_L before the field drops off by a factor of e^{-1}. As the medium becomes SC, k_- and $\sqrt{2}\sigma\mu_0 c^2/(\omega\beta^2)$ must both decrease so that $k_-\lambda_L = 1$ when the material is SC.

Reflectivity profiles of semiconductors can be used to estimate Cooper pair binding energies. Researchers have made a high temperature superconductor of bismuth, strontium, calcium, copper and oxygen. The superconductor has a T_C of 88 K. By analyzing the light reflected from the material above and below 88 K, researchers can tell which frequencies of light it absorbed. The energies of these photons are related to the binding energy of the electron pairs in the superconductor [40].

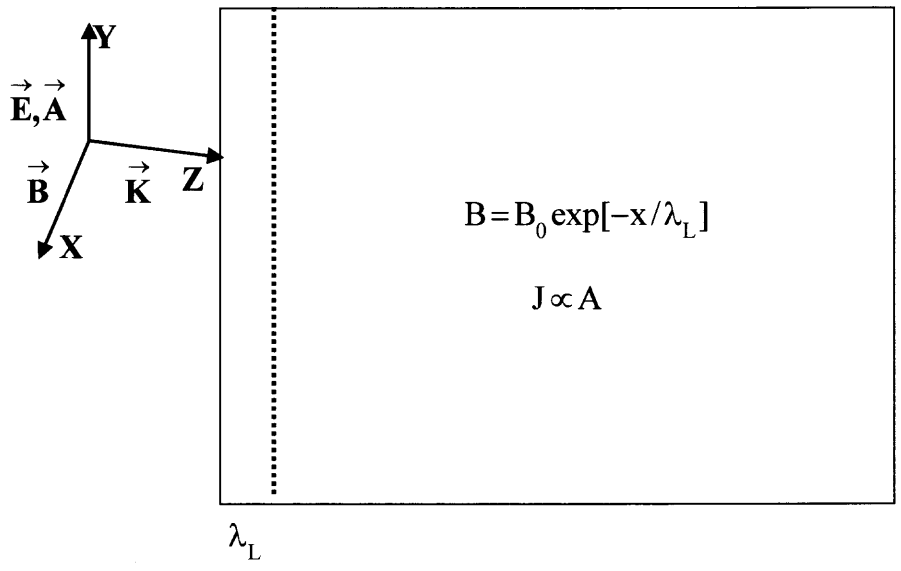

Figure 5.18 EM wave entering a semiconductor in superconducting state.

For a superconductor, if the incident frequency is below $\Delta/\hbar$, where Δ is the energu gap, the conductivity will be zero and the reflectivity will be unity. The theoretical reflectivity profiles for LSCO ($La_{2-x}Sr_xCuO_4$) are shown in Figures 5.19 **[48]**. The reflectivity is plotted against ω/Δ, where γ is the level broadening. The level broadening is a measure of the degree of electronic scattering. At T=0 K, there is a cutoff frequency at $\omega/\Delta=0.7$, below which the reflectivity is unity. The material below that point has zero conductivity. When $\gamma=0$, there will no electron scattering, creating a pure Bloch electron state. As T increases, the reflectivity profiles show marked differences. Other materials will show differences in the reflectivity profiles as T is varied from below T_C to above T_C. In general, as a semiconductor is cooled towards the critical temperature, the reflectivity profile changes. The reflectivity profiles, generated by sensor arrays, can thus easily be used to determine the onset of SC at T is lowered towards the critical temperature.

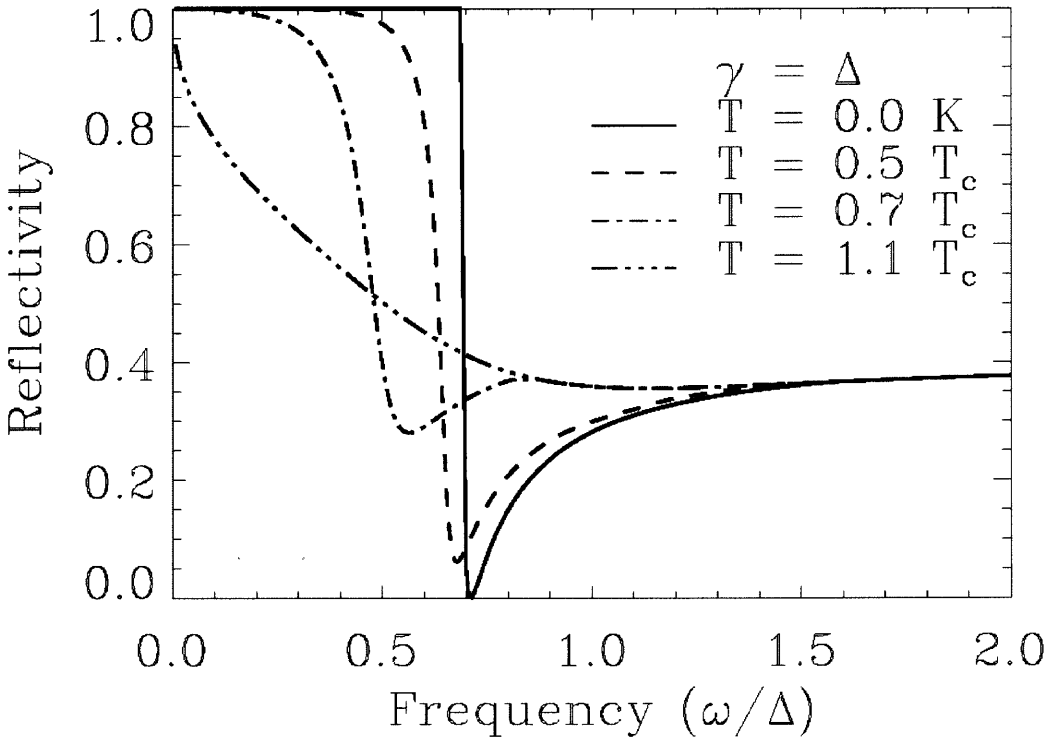

Figure 5.19 Reflectivity of LSCO as a function of the frequency for fixed impurity scattering rate with different temperatures (from Figure 1c of Reference 48).

CHAPTER 6

CONCLUSIONS

This thesis has evaluated conditions for semiconductor superlattice structures for which high $-T_C$ superconductivity is feasible via both theoretical arguments and results of computer simulations. Analysis of computer simulations, with numerous superlattice designs and doping concentrations, seem to support the theoretical argument that Fermi energies and interplanar Coulomb interaction are factors that determine the formation of the quantum wells with electron and hole carrier layers. The Coulomb interactions between layers in a superlattice are a strong factor affecting the feasibility of designing a HTS superlattice that satisfies all the criteria of the Harshman formulation. None of the computer simulations in this study indicated that a superlattice structure that satisfies all the criteria of the Harshman model was possible.

The computer simulations emulated the electronic structure of high $-T_C$ superconductor superlattices with $\beta = 1$. Results are based on a maximum built-in electrostatic field of 500 kV cm^{-1} and a sheet resistance of 10^4 Ohms, which dictates a minimum superlattice period of d = 80 nm and a corresponding sheet carrier density of electrons and holes is $N = 1.56 \times 10^{10}$ cm^{-2}. Based on a strong-coupling electronic model of superconductivity, a superconductor with a transition temperature of 2 K will result from such an electron-hole superlattice.

Synthetic imaging of macro objects in the near field is only possible with circular arrays if small angle approximations exist. Circular arrays can be used to detect the existence of superconductivity in semiconductor material.

APPENDIX A

DERIVATION OF LOGARITHMIC DERIVATIVE OF THE CRITICAL TEMPERATURE

This section will derive the expression:

$$d\log[k_B T_C]/d\log[\hbar\omega_D] = 1-(\mu^* \log[k_B T_C/\hbar\omega_D])^2$$

$$k_B T_C = \hbar\omega_D \exp[-1/(\lambda_{HE}-\mu^*)] \quad \text{(A.1)}$$

$$\mu^* = \mu/(1+\mu\log[E_F/(\hbar\omega_D)]) = \mu/(1+\mu\log[N_S\pi\hbar/(m^*\omega_D])) \quad \text{(A.2)}$$

$$\log[k_B T_C] = \log[\hbar\omega_D] - 1/(\lambda_{HE}-\mu^*) \quad \text{(A.3)}$$

Differentiating the above with respect to $\log[\hbar\omega_D]$ yields:

$$d\log[k_B T_C]/d\log[\hbar\omega_D] = 1-(d\mu^*/\log[\hbar\omega_D])/(\lambda_{HE}-\mu^*)^2 \quad \text{(A.4)}$$

Differentiating μ^* with respect to $\log[\hbar\omega_D]$ yields:

$$d\mu^*/\log[\hbar\omega_D] = \mu^2/(1+\mu\log[N_S\pi\hbar^2/m^*\omega_D])^2 \quad \text{(A.5)}$$

Substitute A.5 into A.4:

$$d\log[k_B T_C]/d\log[\hbar\omega_D] = 1-\mu^2/(1+\mu\log[N_S\hbar^2\pi/m^*\omega_D])^2(\lambda_{HE}-\mu^*)^2 \quad \text{(A.6)}$$

Using and A.1 and A.2 the above becomes:

$$d\log[k_B T_C]/d\log[\hbar\omega_D] = 1-(\mu^* \log[k_B T_C/\hbar\omega_D])^2 \quad \text{(A.7)}$$

APPENDIX B

VALIDITY OF THE 3D HOLE/ELECTRON DENSITY FUNCTIONS AT THE T=0 K LIMIT

It will be shown that the hole and electron densities reduce to zero in the limit as T approaches zero.

The hole density at low T is given by:

$$p = 2\sqrt[3]{2\pi m_H^* k_B T / h^2}\,\exp[-((\Delta E_C + (\hbar^2 k^2/2)(1/m_{AlGaAS} - 1/m_{GaAs}) - 1/2(E_D + k_B T \ln[N_C/N_D]))/k_B T] \quad \text{(B.1)}$$

As $T \rightarrow 0$, $N_C \rightarrow N_D$, and $m_{AlGaAS} \rightarrow m_{GaAs}$, so the second and fourth terms above go to 0.

If $E_D > 2\Delta E_C$, as $T \rightarrow 0$, then $p \rightarrow 0$.

The electron density at low T is given by:

$$n = 2\sqrt[3]{2\pi m_E^* k_B T / h^2}\,\exp[-1/2(E_D + k_B T \ln[N_C/N_D])/k_B T] \quad \text{(B.2)}$$

As $T \rightarrow 0$, the second factor in B.2 approaches a constant and the first factor goes to zero.

APPENDIX C

THE 2-D INVERSE FOURIER TRANSFORM (IFT) OF THE PRODUCT OF TWO DISPLACEMENT VECTORS AND THE CORRELATION FUNCTION

To prove the theorem that the 2-D Inverse Fourier Transform (IFT) of the product of $2r_ir_j$ and the correlation c(i,j) between 2 sensor points located at r_i, r_j yields the intensity distribution on the surface of an illuminated object.

Let r_i, r_j be the distances from a source point 1 to sensors i, j respectively and E(x,y) is the amplitude of the wave field at the source point and k is the wave number. K_1 and k_2 are dummy variables that will be used in integrations. The sensors are in a plane that is parallel to the plane containing the source point as shown in Figure C.1 since one can assume small angle approximations. Since E(x,y) is real, $|E(x,y)|^2$ can be expressed as $E(x,y)^2$.

The wave fields from the source at points i, j are respectively:

$$\varphi_i = (E(x,y)/r_i)(e^{i(kr_i - \omega t)}) \tag{C.1}$$

$$\varphi_j = (E(x,y)/r_j)(e^{i(kr_j - \omega t)}) \tag{C.2}$$

The correlation function c(i,j) for the 2 points is:

$$c(i,j) = Re(\varphi_i \varphi_j^*) = E(x,y)^2 \cos[k(r_i - r_j)]/(r_i r_j) \tag{C.3}$$

The 2-D IFT of $r_ir_jc(1,2)$ is (using $\cos[\alpha] = 1/2(e^{i\alpha} + e^{-i\alpha})$):

$$\int_{-\infty}^{\infty}\int_{-\infty}^{\infty} |E|^2 (1/2)(e^{i(kr_i - kr_j)} + e^{-i(kr_i - kr_j)} e^{-ik_1 r_i} e^{-ik_2 r_j} dk_1 dk_2 =$$

$$\int_{-\infty}^{\infty}\int_{-\infty}^{\infty}|E|^2(1/2)(e^{i(kr_i-k_1r_i-kr_j-k_2r_j)}+e^{-i(kr_i-k_1r_i-kr_j-k_2r_j)}dk_1dk_2 \qquad \text{(C.4)}$$

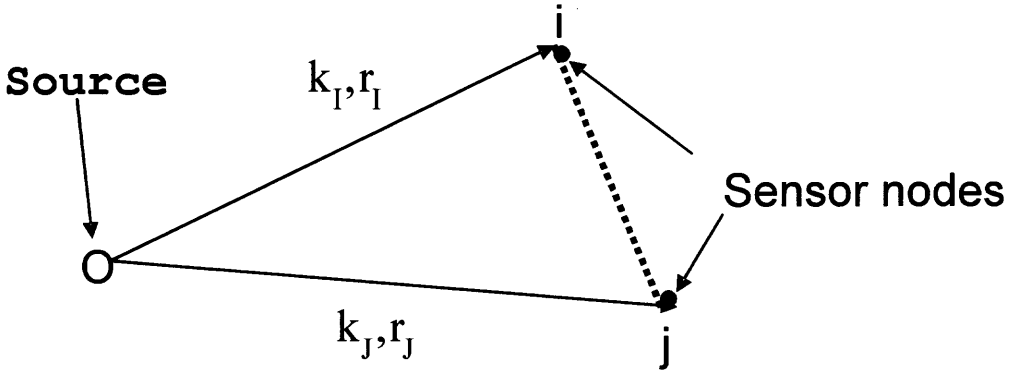

Figure C.1 Geometry of source point and sensor nodes.

To evaluate the above consider, consider the first two terms in the first parenthesis of the above integration:

$$\int_{-\infty}^{+\infty}(e^{i(kr_i-k_1r_i)}dk_1=(1/(ir_i))e^{i(r_i(k-k_1))}\Big|_{k-k_1=-\infty}^{k-k_1=\infty} \qquad \text{(C.5)}$$

One can put the right side of D.5 into a different form, which does not change the evaluation:

$$e^{i(r_i(k-k_1))}\Big|_{k-k=-\infty}^{k-k_1=\infty}=e^{i(r_i(k-k_1))}\Big|_{r_i=-\infty}^{r_i=\infty} \qquad \text{(C.6)}$$

The function in the equation does not approach a limit as $r_i \to \pm\infty$. A limit can be defined as an averaged limit of a large interval. The limit of D.5 can be expressed as:

$$\lim_{\Delta\to\infty} 1/\Delta\int_0^{\infty} e^{i(r_i(k-k_1)} \, dr = 0 \; k \neq k_1$$

$$\lim_{\Delta\to\infty} 1/\Delta\int_0^{\infty} e^{i(r_i(k-k_1)} \, dr = 1 \; k = k_1$$

and $\int_0^{\infty} e^{i(r_i(kr_i-k_1r)} \, dk_1 = 1 \; k = k_1$, 0 otherwise.

Likewise, $\int_{-\infty}^{\infty} e^{i(-kr_j - k_2 r_j)} dk_2 = 1/(-ir_j)$ if $k = -k_2$, 0 otherwise. Applying the same process to the remaining terms in the second parenthesis of D.4, the IFT of $r_i r_j c(1,2)$ now becomes:

$$\int_{-\infty}^{+\infty}\int_{-\infty}^{+\infty} E(x,y)^2 (1/2)(e^{i(kr_i - kr_j)} + e^{-i(kr_i - kr_j)} e^{-ik_1 r_i} e^{-ik_2 r_j} dk_1 dk_2$$

$$= |E(x,y)|^2 / r_i r_j \qquad \text{(C.7)}$$

For small angle approximation, an assumption for near field synthetic imaging, $r_i \cong r_j$ and both can be absorbed into E(x,y). Thus the IFT[$r_i r_j c(1,2)$] = E[x,y]. This, however, is only a partial reconstruction of the intensity distribution. To fully reconstruct the image of an object, a large number of pairs of sensor nodes would be needed.

APPENDIX D

DERIVATION OF THE CONDITION FOR NON-DISSIPATION OF AN EM WAVE THROUGH A CONDUCTIVE MEDIUM

The conditions for non-dissipation of an EM wave, traveling through a conductive Medium, expressed in terms of β and ω will de determined.

Consider an EM wave propagating through a conducting medium and assume $\mu_1 = \mu_2$. Letting $\beta = c\sqrt{\varepsilon\mu_0\sqrt{1+(\sigma/\varepsilon\omega)^2}}$, the reflectivity can be expressed as:

$$R = (1-\beta/1+\beta)^2 \tag{D.1}$$

$$\beta_{\pm} = (1+R\pm 2\sqrt{R})/(1-R) \tag{D.2}$$

For a non-dissipative EM wave in a normal semiconductor:

$$\mu_0\sigma c^2/n^2\omega << 1 \tag{D.3}$$

where $n^2 = \varepsilon\mu_0 c^2$. B can be expressed in terns of the index of refraction n:

$$\beta = \sqrt[4]{n^4+(\mu_0\sigma c^2/\omega)^2} \tag{D.4}$$

$$n^2 = \sqrt{\beta^4-(\mu_0\sigma c^2/\omega)^2} \tag{D.5}$$

Substituting D.5 into D.3, one finds the condition for a non-dissipative EM wave:

$$1 >> \sqrt{2}\sigma\mu_0 c^2/\omega\beta^2 \tag{D.6}$$

REFERENCES

1. Harshman, D. & Mills, A. (1992). Concerning the nature of high-T_C superconductivity: Survey of experimental properties and implications for interlayer coupling. Physical Review, Volume B45, No. 18, 10701.

2. Tan, H., Snider G., Chang, G. D., & Hu, E. (1990). A self-consistent solution of Schrödinger-Poisson equations using a nonuniform mesh. Journal of Applied Physics, Volume 68, Number 8, 4071.

3. Homes, C., Dordevic, S. V., Strongin, M., Bonn, D. A., Liang, R., Hardy, W. N., Komiya, S., Ando, Y., Yu, G., Kaneko, N., Zhao, X., Greven, M., Basovand, D. N., & Timusk, T. (2004). A universal scaling relation in high-temperature superconductors. Nature 430, 539.

4. Hirsch, J. E. (1997). Correlations between normal-state properties and superconductivity. Physical Review, Volume B55, Number 14, 9007-9024.

5. Flukiger, R. (1992). A snapshot view of high temperature superconductivity 2002. Concise Encyclopedia of Magnetic and Superconducting Material, Pergamon Press, Inc., 1.

6. Fisher, O. & Maple, M. B. (1982). Superconductivity in Ternary Compounds. Springer-Verlag, Berlin, 1.

7. Etourneau, J. (1992). Solid State Chemistry: Compounds. Clarendon Press, Oxford, 60.

8. Vonsovsky, S. V., Izyunov, Y. A., & Kurmaev, E. Z. (2002). A snapshot view of high temperature superconductivity 2002. Springer Series in Solid State Sciences, Springer-Verlag, Berlin, 259.

9. Bud'ko, S. L., Lapertot, G., Petrovic, C., Cunningham, C. E., Anderson, N., & Canfield, P. (2001). Upper critical field and irreversibility line in superconducting MgB_2. Solid State Communication, Volume 118, Number 497, 1.

10. Mohanty, P., Wei, J. Y. T., Ananth, V., Morales, P., & Skocpol, W. (2004). Nanoscale high-temperature superconductivity. Physica C 408–410, 666-669.

11. D. R. Harshman, unpublished paper.

12. D. R. Harshman, private communication.

13. Shore, H. B., Zaremba, E., & Sander, L. (1978). Density-functional theory of Wigner crystallization. Physical Review, Volume B18, Number 12, 6506-6509

14. Valenzuela, B., Fratini, S., & Baeriswyl, D. (2003). Charge and spin order in one-dimensional electron systems with long-range Coulomb interactions. Physical Review, Volume B68, Number 045112, 1-11

15. Keimer, B. (2005). Superconductors: the mystery goes on. Physics World, April Issue, 48.

16. Snider, G. (2005). 1D Poisson/Schrödinger User's Manual. http://www.nd.edu/~gsnider, University of Notre Dame, Notre Dame, Indiana.

17. Ram-Mohan, L. (2002). Finite Element and Boundary Element Applications in Quantum Mechanics. Oxford University Press, 241-256.

18. Bardeen, J., Cooper, L. N., & Schrieffer, J. R. (1957). Theory of Superconductivity. Physical Review, Volume 108, Number 5, 1175.

19. Bednorz, J. G. & Mueller, K. A. (1986). Possible high-T_C superconductivity in the Ba-La-Cu-O system. Z Physics B, Condensed Matter, Volume 64, 189-193.

20. Long, M. W. (1990). Low spin correlations between copper spins in oxygen hole superconductors. Journal of Physics: Condensed. Matter, Volume 2, Number 16, 3823-3839.

21. Hirsch, J. (2002). Why holes are not like electrons. Physical Review, Volume B65, Number 18, 4502.

22. D. R. Harshman, private communication.

23. Hirsch, J. (1989). Hole conductors and superconductors. Materials Research Society Symposium Proceedings, Volume 156, 349.

24. Kittel, C. (2004). Introduction to solid state physics. Eight Edition, John Wiley & Sons, Inc., 662.

25. Lynn, J. W. (1990). High temperature superconductivity. Springer-Verlag, New York, 16.

26. Lanzara, A., Bogdanov, P. V., Zhou, X. J., Kellar, S. A., Feng, D. L., Lu, E. D.,Yoshida, T., Eisaki, H., Fujimori, A., Kishio, K., Shimoyama, J., Noda, T., Uchida, S., Hussain, Z., & Shen, Z.X. (2001). Evidence for ubiquitous strong electron-phonon coupling in high temperature superconductors. Nature 41, 510-514.

27. Carlson, E. W., Emery, V. J., Kivelson, S. A., & Orgad, D. (2002). Concepts in High Temperature Superconductivity. Retrieved June 6 2006 from the World Wide Web: http://arxiv.org/PS_cache/cond-mat/pdf/0206/0206217.pdf, 10.

28. Balandin, A. (2002). Thermal Properties of Semiconductor Low-Dimensional Structures. Physics of Low-Dimensional Structures, Volume 1/2, Number 1, 1-43.

29. Tien, C. L & Chen, G. (1994). Challenges in Microscale Conductive and Radiative Heat Transfer. ASME Journal of Heat Transfer, Volume 116, 799.

30. Xiao, Y., Thorpe, M. F., & Parkinson, J. B. (1999). Two-dimensional discrete Coulomb alloy. Physical Review, Volume B59, Number 1, 277-285.

31. Wetzel, C., Efros, A., Moll, A., & Meyer, B. (1992). Dependence on quantum confinement of the in-plane effective mass in $Ga_{0.47}In_{0.53}As$/InPquantum wells. Physical Review, Volume B45, Number 24, 45.

32. Majumda, A., Rokhinson, L. P., Tsui, D. C., Pfeiffer, L. N., & West, K. W. (2002). Effective mass enhancement of two-dimensional electrons in a one-dimensional superlattice potential. Applied Physics Letters Volume 76, Number 24, 3600.

33. Ebihara, T., Bauer, E. D., Cornelius, A.L., Lawrence, J. M., Harrison, N., Thompson, J. D., Sarrao, J. L., Hundley, M. F., & Uji, S. (2003). Dependence of the Effective Masses in $YbAl_3$ on Magnetic Field and Disorder. Physical Review Letters, Volume 90, Number 16, 6404.

34. Davies, J. H. (1998). The Physics of Low-Dimensional Semiconductors. Cambridge University Press, 145.

35. Yariv, A. (1982). An Introduction to Theory and Applications of Quantum Mechanics. John Wiley & Sons, 247-249.

36. Cole, B. E., Chamberlain, J. M., Henini, M., Cheng, T., Batty, W., & Wittlin, A. (1997). Cyclotron Resonance in Ultra-low Hole Density, Narrow, p-type GaAs/(Al,Ga)As QuantumWells. Physical Review, Volume B55, 2503-2511.

37. Walsh, K.P., Fiory, A. T., Ravindra, N. M., Harshman, D. R. & Dow, J. D. (2006). Electron-Hole superlattices in $GaAs/Al_xGa_{1-x}As$ multiple quantum wells. Philosophical Magazine, Volume 86, Number 23, 3593.

38. Huxley, A., Sheikin, I., Ressouche, E., Kernavanois, N., Braithwaite, D., Calemczuk, R., & Flouquet, J. (2001). UGe2: A ferromagnetic spin-triple superconductor. Physical Review, Volume B63, Number 144519, 1.

39 Millis, A. J. (2000). Advances in the Physics of High-Temperature Superconductivity. Science, Volume 288, Number 5465, 468.

40. Pennicott, K. (2002). Superconductivity clue comes out of the blue. Retrieved 6 June 2006 from the World Wide Web: http://physicsweb.org/articles/news/6/3/17.

41. Eck, E. J. (2005). Confirmation: Planar Weight Disparity Improves T_C. Retrieved 6 June 2006 from the World Wide Web: http://www.superconductors.org/32121212.htm.

42. Timusk, T. (2005). High-temperature uncertainty. Physics World, Volume 18, Number 7, 35.

43. Naidu, P. S. (2000). Sensor Array Signal Processing. CRC Press, prologue.

44. Walsh, K.P., Schulkin, B., Gary, D., Federici, J. F., Barat, R. & Zimdars, D. (2004). Terahertz near field interferometric and synthetic aperture imaging. Proceedings SPIE, Volume 5411, 1-9.

45. Griffiths, D. J. (1999). Introduction to Electrodynamics. Prentice Hall, 309.

46. Christy, R. W., Milford, F. J., & Reitz, J. R. (1992). Foundations of Electromagnetic Theory. Addison-Wesley, 405.

47. Ashcroft, N. W. & Mermin, N. D (1976). Solid State Physics. Saunder College, 739.

48. Sarma, S. D. & Hwang, E. H. (2002). On the c-axis optical reflectivity of layered cuprate. Physical Review Letters, Volume 80, Number 21, 4753-4756.